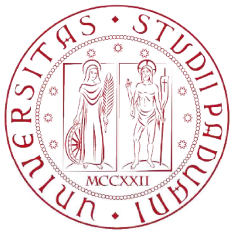

Università degli Studi di Padova
Dipartimento di Fisica e Astronomia
Scuola di Dottorato di Ricerca in Astronomia
Ciclo XXIX

Optical solutions for extreme instrumentation: from ground to space

Direttore della Scuola: Ch.mo Prof. Giampaolo Piotto
Supervisori: Ch.mo Prof. Roberto Ragazzoni
Dott. Demetrio Magrin

Valutatori: Prof. Tom Herbst
Dott. Kjetil Dohlen

Dottorando: Davide Greggio

Padova, Gennaio 2017

Abstract

New generation astronomical instruments have the purpose to enable more and more precise observations of celestial objects. To fulfill the ever increasing requirements posed by new science goals, it is mandatory that the instrument design is developed taking into account the various constraint coming from observing conditions, environment, performance and integration with other instruments and, at the same time, exploiting in the best possible way new technologies and observing techniques.
This Thesis describes the optical design activity conducted for the development of three new instruments: JANUS, SHARK and PLATO. All the three instruments are mainly dedicated to planetary science observations, but they are very different in the techniques they will exploit and the environment in which they will operate.
JANUS is a visible camera that will be part of the ESA space mission JUICE dedicated to the study of Jupiter and its moons. The camera will operate in space, far from the Earth and in a strong radiation environment caused by charged particles trapped by the magnetic field of Jupiter. SHARK is a coronagraphic high-contrast imager for the Large Binocular Telescope (LBT) dedicated to the direct imaging of exo-planets and proto-planetary disks around nearby stars. PLATO is a space satellite dedicated to the indirect detection of earth-sized exo-planets with the transit method.
A brief introduction is given for each instrument, describing their principal characteristics and science objectives, followed by a more detailed description of the optical design and analyses conducted to characterize the performance and fulfillment of the science objectives.

Riassunto

La sfida posta agli strumenti astronomici di nuova generazione è quella di saper produrre dati scientifici sempre più accurati, integrando in maniera intelligente i requisiti scientifici, osservativi o ambientali e, allo stesso tempo, che sappiano mettere a frutto tecnologie o tecniche osservative innovative.
Questa Tesi descrive le attività di progettazione ottica condotte per lo sviluppo di tre nuovi strumenti: JANUS, SHARK e PLATO. Tutti e tre gli strumenti sono dedicati a osservazioni nel campo delle scienze planetarie, ma presentano caratteristiche estremamente diverse sia nelle tecniche osservative utilizzate che nelle condizioni ambientali in cui opereranno.
JANUS è la camera che farà parte della strumentazione di bordo del satellite JUICE, sviluppato da ESA, e che osserverà il sistema di Giove. La camera condurrà osservazioni dettagliate delle atmosfere e delle superfici dei corpi del sistema gioviano in banda visibile estesa e opererà lontano dalla Terra, in un ambiente caratterizzato da forti radiazioni causate dalle particelle cariche intrappolate dal campo magnetico di Giove. SHARK è una camera coronografica per

il Large Binocular Telescope, dedicata all'osservazione diretta di eso-pianeti e dischi proto-planetari attorno a stelle vicine al Sole. PLATO è una missione spaziale dell'ESA dedicata all'osservazione indiretta di eso-pianeti attraverso il metodo dei transiti e sarà in grado di osservare pianeti di tipo terrestre orbitanti nella zona abitabile di stelle di tipo solare.
Nella Tesi è fornita una descrizione generale delle caratteristiche e degli obiettivi scientifici di ogni strumento, seguita da una descrizione più dettagliata dello sviluppo del disegno ottico di tali strumenti e delle analisi condotte per verificare la capcità di soddisfare i requisiti scientifici.

Contents

Introduction

New advances or discoveries in observational astronomy are usually made either by looking at new observables or by enhancing the precision and performance of already available instrumentation. Other times, especially in space missions, new discoveries come from looking at something that has never been observed before because it was inaccessible, even if the technology to perform such observation was already existing and the idea was already in the mind of scientists for several years. Independently from which is the actual situation, these new discoveries are usually made possible by the availability of new instrumentation which is pushing the modern technology to the limit and which allows to achieve extreme performance or to work in very harsh environments. One relatively recent example is the enormous advancement in planetary sciences driven by the discovery of thousands of exo-planetary systems in nearby stars. The detection was made possible by the availability of a new generation of very stable photometric and spectroscopic instruments able to observe the indirect effects of the presence of planets around their host stars. More recently, even more challenging observations have been made to directly detect exo-planets or proto-planetary disks by masking the light of the central star. Despite the huge amount of data retrieved by these new instruments, still a lot of improvements are necessary for the detection and characterization of exo-planets. These data are supposed to be very useful for the understanding of the formation of planets and the origin of life. Not only data from exo-planetary system will be useful to answer these questions, but also a better knowledge of our Solar System can provide detailed information on the chemical and physical processes happening in the planetary systems. This knowledge will put constraints on the evolutionary paths that bring from a proto-planetary disk to a planetary system.
During my PhD I had the opportunity to work on the optical design and characterization of three new instruments dedicated to planetary observations: JANUS (Jupiter Amorum Ac Natorum Undique Scrutator), SHARK (System for coronagraphy with High order Adaptive optics from R to K band) and PLATO (PLAnetary Transit and Oscillations). These three instruments, dedicated to different targets, will operate in very different environments and will require their own observation strategies. Although any of these instruments has its own specific requirements, all of them present many challenges in the design and require the exploitation of extreme technological solutions for the fulfillment of their scientific task. JANUS is a visible camera that will be part of the space mission JUICE operated by ESA and dedicated to the study of Jupiter and its moons. The camera will operate in space, far from the Earth and in a strong radiation environment caused by charged particles trapped by the magnetic field of Jupiter. SHARK is a coronagraphic high-contrast imager to be installed at the Large Binocular Telescope (LBT) dedicated to the direct imaging of exo-planets and proto-planetary disks around nearby stars via extreme AO. PLATO, the medium class mission of ESA, is a space satellite operating at the Lagrange point L2, dedicated to the indirect

detection of exo-planets with the transit method. It will achieve extremely stable photometry over a wide field of view and with high dinamic rang,e thanks to a multi-telescope approach. In this Thesis, I will present in detail the optical design of JANUS, SHARK and PLATO, along with the design trade-offs, expected performance and some preliminary analysis that I have been conducting during the last three years. Chapter 1 is dedicated to a general introduction of some concepts of optical design. The purpose of this presentation is to describe some topics or quantities used throughout the Thesis and some constraints usually encountered in optical design. Then, a chapter is dedicated to each of the instruments (Chapters 2, 3 and 4). They include an overview of the instrument and a brief description of the science goals and the requirements, followed by a more detailed description of the design and analyses conducted to assess their performance.
The main work consisted in the optical design and characterization of JANUS and SHARK throughout the different project phases, from the preliminary design until the "almost" final design. I first focused on the definition of the optical configuration and its optimization, and then I conducted several analyses to characterize the system tolerances, the thermal evolution, the stray-light, etc. Many of these studies are based on ray-tracing with the software Zemax. Others are based on analytic or semi-analytic models. More recently, I have also been involved in the PLATO project. My activity consisted in the design adaptation and procurement of optics to build a prototype of one of the PLATO telescopes.The prototype will allow us to test the foreseen AIV procedure and to verify the thermal behavior of the telescope in the transition from the assembly temperature to the working temperature. This will be extremely important in view of the mass production required for the building and assembly of all the 28 telescopes.

Chapter 1

Optical design concepts

1.1 Introduction

The optical design process has evolved rapidly in the last decades. In the first half of the last century, optical design relied mainly on hand calculations of linear equations for paraxial rays through an optical system, or third order estimation of the aberration coefficients. For complex optical systems, the calculations could be very long and prone to errors and an analytic solution was not guaranteed when aberrations were taken into account. The situation started to change between the 1960s and 1970s when the first practical computer software for optical design started to appear (see [1]). Later, between 1980 and today, many commercial programs have been produced and developed, and the improvement of this software is still continuing. An optical design software usually allows to: (1) define the optical prescription i.e. the shape, position, materials of an optical system, (2) evaluate the system performance (3) optimize the optical system by mean of a user-defined error or "merit" function. Generally the calculations are made by propagating rays from an object plane through the system until they reach the image plane. The big advantage is that not only paraxial rays can be calculated, but also exact rays produced by reflection or refraction from a surface in the optical system. In the following I will call these rays *"real"* to distinguish them from the paraxial ones. Some of the big advantages of optical design software are the speed-up of the optimization process, the possibility to design, simulate and optimize complex optical systems and a great versatility that allows the designer to deal with very different problems. Moreover, a huge effort has been made in the last years to develop user-friendly graphic interfaces that make the interaction process between program and designer easier and allows also non-expert users to test simple designs and perform basic analysis of optical systems. On the other hand, the use of optical software without a proper knowledge of the optical principles can lead to errors, unexpected results or a lot of time spent trying to optimize an optical system without getting any progress on it. For this reason, it is necessary to have a good knowledge of the optical principles, together with some experience in the field and knowledge of the manufacturability of optical components. Finally, one has to remember that the optical models that can be realized with optical design software never provide a complete description of the real behavior of the system. Sometimes one can produce different models that provide complementary information about the system, but most of the time other analysis needs to be performed in order to understand if the designed instrument is really able to meet the scientific requirements it was conceived for. The next sections will be dedicated

to the definition of some general concepts of optical design that are necessary for the correct statement of optical problems. Then, I'll present some rules and procedures that I have found useful during the design and analysis of JANUS, SHARK and PLATO. The topics covered by this chapter are not complete and not all of them arise from specific physical laws, but are rather the product of the experience gained during the last few years that I spent working on optical design of astronomical instrumentation.

1.2 Paraxial design

1.2.1 paraxial ray propagation

When starting the design of a new optical system, considering the paraxial approximation for ray propagation is a good starting point before further refinements of the design. Moreover, most of the basic properties of an optical system like focal length, entrance pupil diameter, plate scale, magnification or field of view, which are usually set by the scientific requirements, can be determined from paraxial calculations. From the paraxial point of view, a lens or a mirror in an optical system is defined only by its *focal length*, f (or by its *optical power*, $\phi = 1/f$). For mirrors, the focal length is equal to half the radius of curvature with positive sign if the center of curvature lies on the same side of the incoming ray and negative if the center of curvature is on the opposite side of the incoming ray. The focal length of a lens is slightly more complicated and depends on the index of refraction n of the glass, on the central thickness d and on the curvature of the two surfaces. It is given by:

$$\frac{1}{f_{lens}} = (n-1)\left(\frac{1}{R_1} - \frac{1}{R_2} + \frac{(n-1)d}{nR_1R_2}\right) \tag{1.1}$$

The same sign convention as for mirrors holds for the curvature of the two surfaces of a lens. The propagation of a ray through an optical system is determined by two simple linear equations. Considering the 2D case (see figure 1.1) and calling z the direction of propagation of the ray, y the ray height and u the ray angle (expressed in radians) with respect to the z axis, the two equations can be expressed as:

$$y' = y + u'z' \tag{1.2}$$

$$u' = u - y\phi \tag{1.3}$$

Eq. 1.2 gives the propagation of the ray in free space and is usually called the *transfer equation*, while eq. 1.3 determines the bending of the ray at a surface with optical power and is called the *refraction equation*.

1.2.2 Conservation of étendue

Different rays that pass through a lens do not behave independently. This is because there are some invariant quantities in the propagation of rays ([2]). One very important quantity relates the height and angles of a couple of rays. Consider two paraxial rays that pass through a lens. At a given plane, where the medium has an index n, one ray has height y_1 and angle u_1, and the other has height y_2 and angle u_2. The quantity

$$L = n\left(y_1u_2 - y_2u_1\right) \tag{1.4}$$

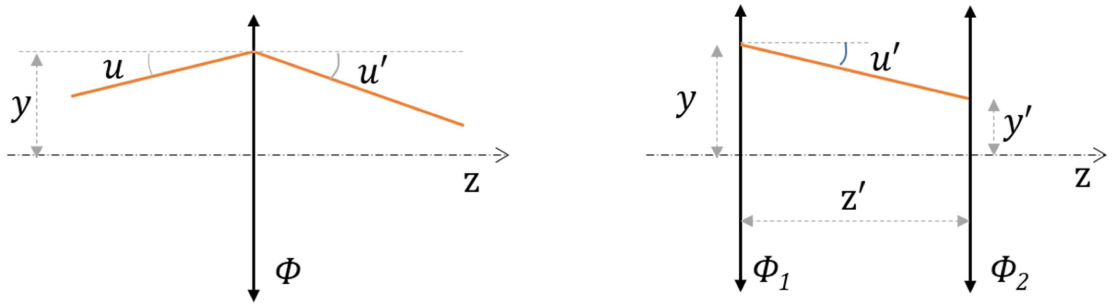

Figure 1.1: Paraxial ray propagation. Left: refraction from an optical element. Right: straight propagation between two optical elements.

is unchanged as the rays propagate through the system. Applying equations 1.2 and 1.3 to the above relation shows that the quantity is not changed by propagation between surfaces or by refraction from a surface with optical power. Of course this relation is true only for normal propagation based on reflection or refraction and does not consider other possible phenomena like scattering. Moreover, equation 1.4 refers to the one-dimensional case and is true only for rotationally symmetrical systems. This relation arises from basic physical principles and is the paraxial version of the more general *Lagrange invariant* which is also referred to as *"conservation of étendue"* or *"conservation of throughput"*. This invariance shows that there are fundamental limits on what optical systems can do. For example, given the paraxial heights and angles of two input rays, only three of the four output heights and angles can be chosen arbitrarily.
In astronomy, that is generally characterized by big telescope apertures, the conservation of étendue usually manifests itself when trying to reduce the size of the pupil inside instruments in order to have smaller optical elements. If we have a telescope with an 8 m aperture and we want to re-image the telescope aperture inside an instrument with a size of 8 mm, the height of the rays are squeezed by a factor of 1000, thus resulting in the ray angles (field angles) to increase by the same factor. Bigger angles means bigger optics far from the pupil plane and, generally, also greater aberrations.

1.2.3 Image formation

The paraxial ray tracing equations can be used to determine the location of the image of a particular object just by tracing two rays emanating from the same point of an object and calculating their intersection point after the propagation through the optical system. For a single lens system it can be verified that a very simple relation holds between the object-lens distance p, the lens-image distance q and the lens optical power. This relation is known as *Gauss thin lens formula* and is given by:

$$\frac{1}{p} + \frac{1}{q} = \frac{1}{f} \tag{1.5}$$

The ratio between the height of the image and the height of the object is called *lateral magnification* and is equal to $m = q/p$. In image 1.2 h_1 and h_2 have opposite signs and the magnification is negative. For multi-lens systems equation 1.5 can be used to calculate the

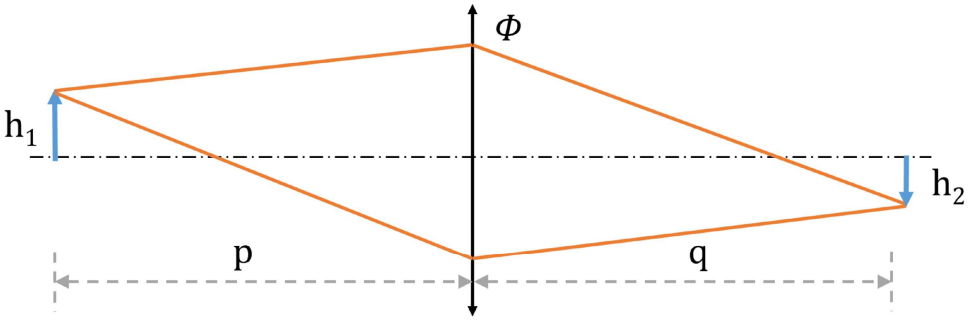

Figure 1.2: Schematic drawing of paraxial image formation

final image in multiple steps. First find the position of the image of the object made by the first lens, then use the first image as the object for the second lens and find the second image position. Proceed in this way until the last element is reached and the final image is formed. When dealing with complex optical systems made up of multiple elements, it is sometimes useful to consider the whole assembly as a single lens system. In the paraxial approximation, the properties of the whole system can be expressed just by two numbers: the system focal length and the effective lens position. The formulae relating the power and position of single elements to the system focal length can be quite complex. In the case of a two lens system, the equivalent focal length is given by:

$$f_{eq} = \frac{f_1 f_2}{f_1 f_2 - d} \tag{1.6}$$

where d is the distance between the two lenses. In a telescope, the effective focal length is directly related to the *plate scale* which gives the relation between the on-sky field angle and position in the image plane [1]:

$$plate\ scale = \frac{1}{f_{eq}} \tag{1.7}$$

where the units are $radians/mm$. In astronomy, the plate scale is more often expressed in $arcsec/mm$ or $arcsec/px$ by making the proper unit transformation.

1.2.4 Aperture, pupil and field

The first step from paraxial, infinite lenses toward a more realistic system comes from considering the finite size of optical elements. Defining the size of the aperture of an instrument means defining its light gathering capabilities and, from a wave-optics point of view also its resolving power. Light rays are emitted from an object point in all directions and only a fraction of them is captured by the optical system and reach the image plane. For axial object points, the delimiting structure is called the *aperture* or the *stop*. The aperture can be a lens, a mirror or another external structure like an adjustable iris. The size and position of the aperture do not affect the paraxial properties like magnification, conjugate object-image points or focal length. They do affect the image irradiance and aberrations, however.

[1] "Classical" telescopes are afocal systems and are designed to be coupled to the eye of the observer. In this case the plate scale is determined by the assembly telescope-eye. In the text we refer to telescopes used in "imaging" mode.

Two rays are particularly useful to track the size of the light beam through an optical system. The first ray is the one originating from the axial object point that passes through the edge of the aperture and it is called *marginal ray*. The other is the ray originating from the edge of the object field that passes through the center of the aperture and is called *chief ray*. The marginal ray tracks the maximum aperture size, while the chief ray tracks the maximum field size.
Other very useful characteristics of an optical system are its *entrance pupil* and *exit pupil*. The entrance pupil is the image of the stop as seen from the object plane. Its size and position are determined by calculating the image of the stop made by all the optics between the object plane and the aperture plane. The exit pupil is the image of the stop as seen from the image plane. Its size and position can be calculated by tracing the image of the stop made by the optics between the aperture plane and the image plane. To combine two optical sub-systems without losing light one should match the exit pupil of the first system to the entrance pupil of the second system and the same can be done for following subsystems. This effect is usually demonstrated by looking through binoculars. More generally, the term "pupil" is used to identify any intermediate image of the aperture stop (either real or virtual) or the stop itself.
The *field of view* of a system is usually expressed as an angle in object space or as an object

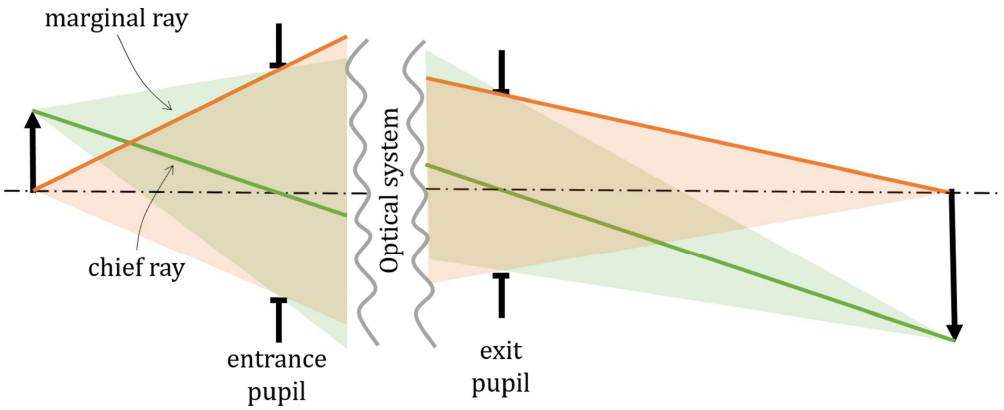

Figure 1.3: Schematic definition of chief ray and marginal ray.

height. In astronomy, the first definition is more common since the objects are approximately at infinite distance. Since rays enter an optical system through its entrance pupil, which is placed in object space, the field angle is equivalent to the angle of the rays at the entrance pupil. It is interesting to notice that, in the paraxial approximation, rays from different field points overlap at the entrance pupil and at subsequent pupil planes while they are perfectly separated at image planes. This is because object and image plane are conjugated and there is a one-to-one correspondence between points on the two planes. The opposite happens for rays from the same field point that pass through different positions of the pupil. These rays are well separated at the pupil plane while they overlap at the image plane. The concept can be summarized with the following statement: "on pupil planes there is information on the entrance position while on image planes there is information on the entrance angle". This is true for an object at infinity, for which the rays coming from a given object point enter the system all with the same angle.

1.2.5 Radiometry and image irradiance

Radiometry measures the amount of light emitted by objects and transmitted through an optical system. The definition of radiometric quantities can be different from one author to another and particular care should be used when using quantities from other works. Here, I will use the notations and definitions given in [3]. The amount of power emitted by the differential projected area $dA \cdot cos(\theta)$ of a source, into the differential solid angle $d\omega$ is called *radiance*:

$$L = \frac{d^2\Phi}{dAcos(\theta)d\omega} \tag{1.8}$$

the units are $photons/s/m^2/sr$ or $W/m^2/sr$. If transmission losses are neglected, radiance is conserved through an optical system. The radiance of the image is the same as the radiance of the exit pupil or the radiance of the object. This is a consequence of the conservation of étendue (or conservation of *throughput*). The *throughput* of an optical system is defined as:

$$G = \int_{A_s}\int_{A_c} \frac{dA_s cos(\theta_s) dA_c cos(\theta_c)}{d^2} = \int_{A_s}\int_{A_c} dA_s cos(\theta_s) d\Omega_c = \int_{A_s}\int_{A_c} dA_c cos(\theta_c) d\Omega_s \tag{1.9}$$

Where dA_s is an infinitesimal area of the source, dA_c is an infinitesimal area of the collector, θ_s is the angle between the normal to the source and the direction of the collecting surface, θ_c is the angle between the normal to the collector and the direction of the source and d is the distance between source and collector (see figure 1.4). An approximation of the expression

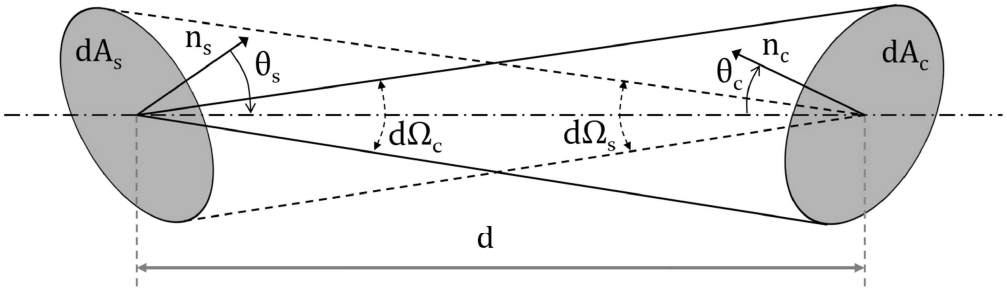

Figure 1.4: Quantities used in the definition of throughput.

above can be made when source and collector are normal to each other (i.e. $\theta_s = \theta_c = 0$) and $d^2 >> A_s, A_c$. With these conditions eq. 1.9 becomes:

$$G = \frac{A_s A_c}{d^2} = A_s\Omega_c = A_c\Omega_s \tag{1.10}$$

This is the reason why the throughput is also called $A\Omega$ product. Throughput is constant across an optical system and, in an imaging system, it is usually calculated on the focal plane using as collecting surface the area of a pixel. Accounting also for the index of refraction of the medium in which the throughput is calculated, the expression becomes:

$$n_1^2 G_1 = n_2^2 G_2 \tag{1.11}$$

The *irradiance* E incident on a surface is the ratio between the infinitesimal flux $d\Phi$ incident on the surface and the infinitesimal area dA:

$$E = \frac{d\Phi}{dA} \tag{1.12}$$

Irradiance is measured in $ph/s/m^2$ or W/m^2. The irradiance at a distance d from a surface source with radiance L and area A is given by the cosine-to-the-fourth law:

$$E = \frac{LAcos^4(\theta)}{d^2} \tag{1.13}$$

as depicted in figure 1.5 The flux on an infinitesimal surface dA due to a source with surface

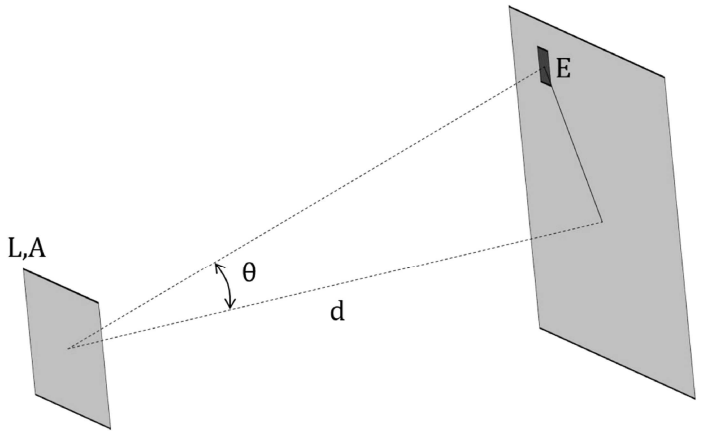

Figure 1.5: Relationship between surface source radiance and irradiance.

radiance L_s is given by:

$$\Phi = \int_{A_s}\int_{A_c} \frac{L_s dA_s cos(\theta_s) dA_c cos(\theta_c)}{d^2} \tag{1.14}$$

If the source is Lambertian, i.e. L_s is constant with θ, eq. 1.14 becomes:

$$\Phi = L_s \int_{A_s}\int_{A_c} \frac{dA_s cos(\theta_s) dA_c cos(\theta_c)}{d^2} = L_s G \tag{1.15}$$

which means that the flux from a Lambertian source is the product of the surface radiance and the throughput of the optical system. If we take the throughput relative to a pixel, we get the flux/pixel of the source.

1.3 Optical aberrations

1.3.1 introduction

The second step in the optical design process is evaluation and minimization of aberrations. Aberrations of an optical system are deviation from the perfect imaging system, i.e. a system in which each point in the object plane is imaged perfectly to one point in the image plane. Aberrations have many effects that can be described in different ways, depending on which is the measurable or the particular application. Some possible descriptions of aberrations includes geometrical wavefront, optical path length, ray angles or ray intersection points ([2]). The amount of aberration depends on the aperture size and position, the field of view, the shape of optical surfaces and also on wavelength when using refractive optical elements. Aberrations are categorized in a variety of ways based on pupil dependence, field dependence

or symmetry characteristics. In the following sections I'll present two of the most common systems for characterization of aberrations: the third order Seidel aberrations and the Zernike polynomials.
For many applications, and especially in complex optical systems, minimization of aberrations is usually accomplished through optimization routines in optical design software. However, if possible, finding an analytical solution provides a better starting point for the optimization process and allows the designer to understand if a system can be simplified, for example by decreasing the number of aspherical surfaces or the number of optical elements.
When a system is free from geometrical aberrations, image resolution is limited by diffraction which blurs the image of a point source. Diffraction is due to the wave nature of light and is a particular type of interference, originating when a wavefront reaches an obstruction. The result is that the wave, once the obstacle is crossed, starts propagating in directions which are different from the one of the incoming wavefront, accordingly to the Huygens principle. If we neglect the atmosphere, the wavefront coming from a star and reaching a telescope aperture is flat. The selection of a portion of such a wavefront, made by the telescope stop, defines an area inside which the photons have to go through, to reach the focal plane. According to Heisenberg uncertainty principle, an uncertainty is then introduced on the direction of the photons motion, which translates into a point-like source image enlargement. In the case of a circular aperture, the image of a point-like source is a ring pattern called "Airy diffraction pattern" (see figure 1.6). The radius of the first dark ring of the Airy pattern, corresponding to the theoretical resolution limit, is given by:

$$\theta_{Airy} = 1.22\frac{\lambda}{D} \tag{1.16}$$

where D is the telescope diameter and λ is the wavelength of observation.

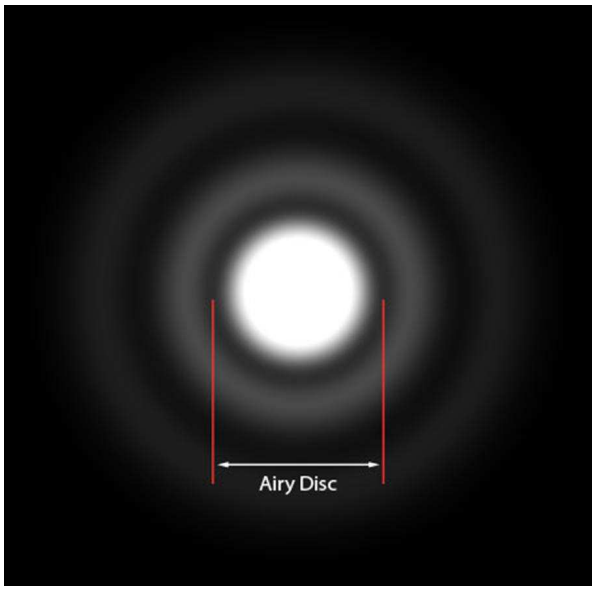

Figure 1.6: Airy diffraction pattern.

1.3.2 Wavefront and ray aberrations

In an unaberrated system, the optical path length of all rays from one object point to its image is identical and the geometrical wavefront leaving the exit pupil is spherical. Usually, rather than looking at the wavefront shape, it is preferable to consider the deviation from the perfect spherical wavefront, which is called the *reference sphere*. The reference sphere is generally centered on the paraxial image location and intersects the center of the exit pupil. The *wavefront aberration* W is defined as the optical path difference between the wavefront and the reference sphere. The wavefront aberration is calculated over the exit pupil and is different for each image point. Thus, it depends on both the pupil coordinates and image coordinates. Usually pupil coordinates are denoted with $(\xi;\eta)$ while image coordinates with $(x;y;z)$, thus $W = W(\xi;\eta;x;y;z)$. The z coordinate is generally set constant, because the image plane is fixed. If the absolute path length is not important, but only path differences between rays, the radius of the reference sphere can be chosen arbitrarily. The absolute value is significant only when combining coherent light beams that interfere one with the other. Errors in absolute optical path are called *piston errors*.
Another method of evaluating aberrations is to look at the ray intercept in the image plane. In a perfect system, all the rays from an object point intersect at a common point in the image plane that is the paraxial image location. In an aberrated system, the *transverse ray aberration* is given by the displacement $(\epsilon_x;\epsilon_y)$ between the real intersection point and the nominal one. Also in this case, the displacement is a function of the pupil coordinates $(\xi;\eta)$ and nominal image coordinates $(x;y)$.
A ray intercept diagram, or *spot diagram*, is a plot that shows the intersection points of a group of rays with the image surface. In general, the group of points originates from a single object point and sample the pupil with a uniform grid or hexagonal pattern. For rotationally symmetric systems, the spot diagram relative to an object point on the optical axis is also rotationally symmetric. If the object point is off-axis, then object points symmetric with respect to the optical axis will have symmetric spot diagrams. This property is commonly used to speed up the optimization process in optical design software.
Since rays are normal to wavefronts, transverse ray aberration is proportional to the slope of the wavefront aberration function (see figure 1.7). For systems of rotation with image space index n and marginal ray angle θ, the transverse aberrations are approximated by the following relations [4]:

$$\epsilon_x = \frac{1}{nsin(\theta)}\frac{\partial W}{\partial \xi} \quad \epsilon_y = \frac{1}{nsin(\theta)}\frac{\partial W}{\partial \eta} \tag{1.17}$$

where ϵ is the transverse ray aberration and the partial derivatives are performed in the pupil coordinates.

1.3.3 Seidel aberrations

Seidel aberrations arise when considering one more term in the Taylor expansion of $sin(\theta)$ with respect to the paraxial approximation:

$$sin(\theta) \approx \theta + \frac{\theta^3}{3!} \tag{1.18}$$

There are five third-order Seidel aberrations: spherical, coma, astigmatism, field curvature and distortion. Each can be expressed as a function of the pupil and image coordinates and

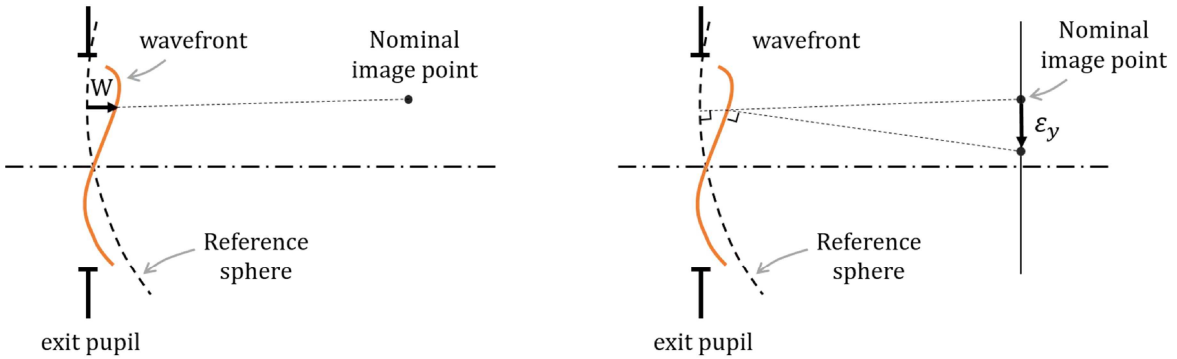

Figure 1.7: Left: definition of the geometrical wavefront aberration. Right: definition of transverse ray aberration and relation with the wavefront aberration.

can be evaluated as wavefront errors or transverse ray aberrations. Calling $\rho^2 = \xi^2 + \eta^2$ the radial pupil coordinate and $h^2 = x^2 + y^2$ the radial image coordinate, the wavefront aberrations of the Seidel aberrations are given by:

$$\begin{aligned} W_{sph} &= W_{040}\ \rho^4 && spherical \\ W_{coma} &= W_{131}\ \rho^2 \eta h && coma \\ W_{asti} &= W_{222}\ h^2 \eta^2 && astigmatism \\ W_{fcur} &= W_{220}\ h^2 \rho^2 && field\ curvature \\ W_{dist} &= W_{311}\ h^3 \eta && distortion \end{aligned} \tag{1.19}$$

where W_{LMN} are called *Seidel wavefront coefficients*. Spherical aberration is circularly symmetric in the pupil plane and depends on the fourth power of the pupil radius. In coma, the wavefront aberration increases linearly with field height. In astigmatism, the aberration is cylindrical with a quadratic dependence on the pupil coordinate. Field curvature is an axial variation of focal position with field height (ρ^2 is the defocus term). Distortion is a deviation of similarity between object and image in which the magnification increases or decreases as a function of field height. From the wavefront aberrations it is possible to calculate the transverse ray aberrations by use of the equations 1.17

1.3.4 Zernike polynomials

For a given field position, wavefront aberration over a circular pupil can also be decomposed into the *Zernike polynomials*. The Zernike polynomials are a set of basis functions orthonormal and complete on a circle. This means that each function defined in a circular domain can be decomposed as a unique linear combination of Zernike polynomials. In polar pupil coordinates $(\rho; \theta)$, the Zernike decomposition of a wavefront W is given by:

$$W(\rho;\theta) = \sum_{n,m} C_n^m Z_n^m(\rho;\theta) \tag{1.20}$$

where n, m denote the radial and azimuthal indices respectively, C_n^m are the linear coefficients of the decomposition and Z_n^m are the Zernike base functions [5]:

$$\begin{aligned} Z_n^m(\rho;\theta) &= R_n^m(\rho)cos(m\theta) \qquad for\ n-m\ even \\ Z_n^{-m}(\rho;\theta) &= R_n^m(\rho)sin(m\theta) \qquad for\ n-m\ odd \end{aligned} \tag{1.21}$$

where $R_n^m(\rho)$ is defined for n and m integers with $n > m \geq 0$ by:

$$\begin{aligned} R_n^m(\rho) &= \sum_{l=0}^{(n-m)/2} \frac{(-1)^l (n-l)!}{l!\left[\frac{1}{2}(n+m)-l\right]!\left[\frac{1}{2}(n-m)-l\right]!}\rho^{n-2l} \qquad for\ n-m\ even \\ R_n^m(\rho) &= 0 \qquad for\ n-m\ odd \end{aligned} \tag{1.22}$$

The Zernike polynomials up to the fourth radial order are summarized in figure 1.8. As can be seen from the names of the polynomials, the first terms are related to the primary Seidel aberrations, although there isn't a perfect match between the wavefront shapes. In general, a wavefront is decomposed in terms of Zernike polynomials up to a certain radial order and a fitting error is provided representing the deviation between the starting wavefront and the decomposed one. The maximum radial order is related to the maximum spatial frequency of the aberrations in the pupil plane.

1.3.5 Chromatic aberrations

Chromatic aberrations or chromatism occurs due to the wavelength dependence of the index of refraction in optical materials. This causes rays of different wavelengths to follow different optical paths thus causing an elongation of the image. Chromatic aberration is generally introduced by lenses in optical systems but also the atmosphere can contribute to chromatic aberrations. It is common to ditinguish between *longitudinal* chromatic aberration and *lateral* chromatic aberration. The longitudinal aberration gives the variation of the best focus positions for different wavelengths for axial objects. The lateral chromatic aberration gives the transverse displacement between images of the same object point at different wavelengths and can be due to a wavelength dependence of the system magnification or distortion.

Longitudinal chromatic aberration is commonly reduced by splitting the lens in a couple of lenses made of glasses with different dispersion (which is related to the *Abbe number*). In order to correct for chromatism, one of the lenses should have positive optical power, while the other one should have negative optical power. Moreover, the focal length of the two-lens system should be the same as the focal length of the starting lens. Considering a system working in the wavelength range $[\lambda_a, \lambda_b]$, and calling $\lambda_m = (\lambda_a + \lambda_b)/2$ the mean wavelength, the dispersion is given by:

$$V = \frac{n_m - 1}{n_a - n_b} \tag{1.23}$$

where n is the refractive index of the glass at the different wavelengths. The condition for chromatic correction is then given by:

$$f_1 V_1 + f_2 V_2 = 0 \tag{1.24}$$

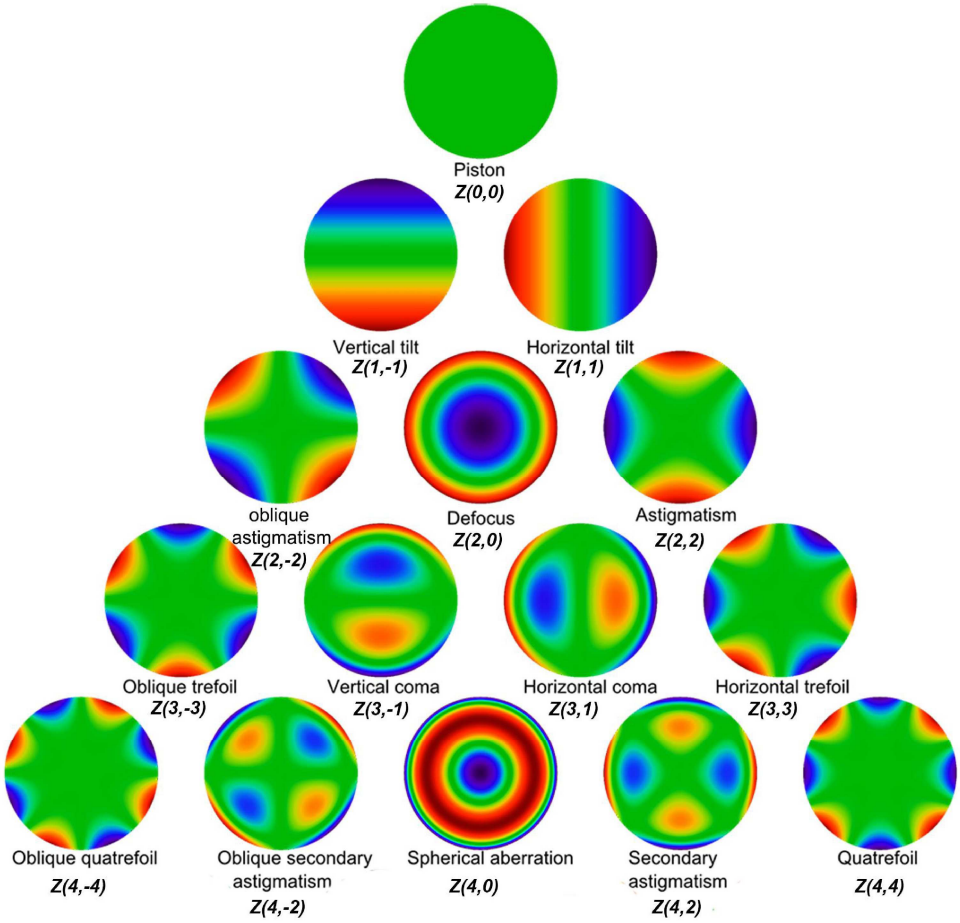

Figure 1.8: Wavefront shape of the Zernike polynomials up to the fourth radial order.

with f_1 and f_2 denoting the focal length of the two lenses. In the thin lens approximation, the total focal length of a system composed of two lenses in contact is:

$$\frac{1}{f} = \frac{1}{f_1} + \frac{1}{f_2} \tag{1.25}$$

Solving equations 1.24 and 1.25 gives the focal length of the two lenses for the chosen pair of glasses that minimizes the chromatic focal shift in the waveband of interest.

In the case of atmospheric color aberration, the biggest contribution is given by *atmospheric differential refraction*. In fact, when observing a celestial object away from the zenith direction, the earth atmosphere acts as a lens, bending the rays from their original direction. Since the refractive index of air is wavelength dependent, the deviation is also wavelength dependent and lateral color is introduced in a way similar to what happens when producing low resolution spectra with prisms. Atmospheric differential refraction is a function of zenith angle and wavelength, being stronger for large zenith angles and for shorter wavelengths. It also depends on other parameters like air pressure, height of the observing site, temperature and humidity. In astronomy, atmospheric refraction is usually not considered a big issue when

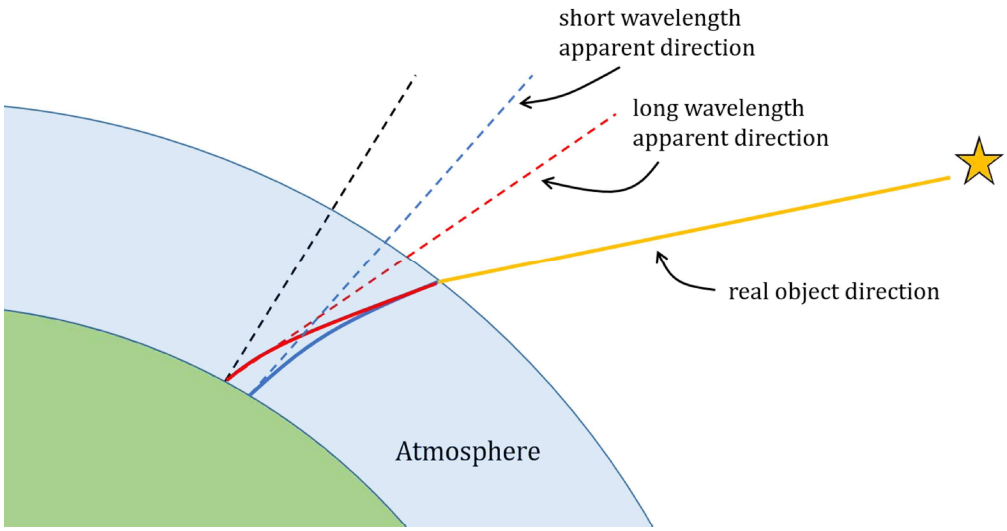

Figure 1.9: Schematic representation of the atmospheric chromatic dispersion.

observing in the near-infrared (NIR) or at longer wavelengths. Nevertheless, when working close to the diffraction limit of an 8m class telescope, atmospheric differential refraction needs to be corrected also in the NIR. This is generally achieved by means of a dispersive element that introduces a variable dispersion, opposite to the atmospheric one. The dispersion needs to be variable because the object's zenith angle changes during the night. Thus, the correction needs to be adapted to the altitude of the object.

1.4 Image quality estimation

1.4.1 Introduction

The quality of an optical system can be estimated in many ways depending on the characteristic of the instrument and the kind of observations it will conduct. A first distinction can be made between *focal* and *afocal* systems. A focal system is a system whose purpose is to make an image of an object. Its quality is usually estimated by looking at the properties of the image (contrast, sharpness, etc...). In an afocal system, the purpose is not to form an image but, for instance, to expand or compress a beam, or to produce an angular magnification in a collimated beam as with binoculars. In the following, I will consider only focal systems since they are the topic of this thesis.
A second distinction can be made between "*nominal*" and "*real*" systems. Nominal is used to define a system as it is by design, i.e. without accounting for imperfections in the manufacturing of the optical components or in the alignment of the system. A real system, on the other hand, is characterized by imperfections that translate to poorer performance. These imperfections can usually be simulated by optical design software and the procedure of analyzing and quantifying the effects of imperfections is referred to as *tolerance analysis*. Finally, the image quality can be estimated with a ray approach or a wavefront approach, depending on the characteristic of the instrument. The ray approximation is generally not accurate when working close to the diffraction limit, since it does not account for diffraction effects.

1.4.2 Spot diagram

The spot diagram is a diagram showing the intersection positions of the rays from an object point in the focal plane. For a stigmatic (i.e. free of aberrations) imaging system, all the rays focus at a common point and the spot diagram is a single point with infinitesimal size: the system has no geometrical aberrations and is diffraction-limited. If the system is aberrated, the rays intersect the image plane at different locations and the collection of all the rays forms a spot whose shape is related to the type of aberration affecting the system. The "Root mean square" (RMS) of the spot is defined as:

$$RMS = \sqrt{\frac{1}{N}\sum_{i=1}^{N}[(x_i - x_c)^2 + (y_i - y_c)^2]} \tag{1.26}$$

where x_i and y_i are the coordinates of the $i-th$ ray, x_c and y_c are the coordinates of a central reference point (most commonly the centroid or chief ray position) and the sum is performed over the whole set of N rays. If the RMS is much greater than the Airy disk then the aberrations dominate over diffraction effects and the spot diagram is a good estimation of the image size and shape. If the RMS is smaller than the Airy disk, then diffraction effects should also be considered to get accurate results.

1.4.3 Point spread function and strehl ratio

The point spread function (PSF) describes the response of an imaging system to a point source. Two algorithms are commonly used to calculate the PSF of an optical system: the Fourier transform and the Huygens wavelets method. The fast Fourier transform (FFT) PSF algorithm exploits the fact that the diffraction PSF is related to the modulus of the Fourier transform of the complex amplitude of the wavefront in the exit pupil of the optical system. The amplitude and phase in the exit pupil are computed for a grid of rays, an FFT is performed, and the diffraction image intensity is computed.
The Huygens wavelets method is based on the principle that each point on a wavefront can be considered as a perfect point source with an amplitude and phase. Each of these point sources radiates a spherical "wavelet", sometimes called a "Huygens wavelet" after Huygens, who first proposed the model. The diffraction of the wavefront as it propagates through space is given by the interference, or complex sum, of all the spherical wavelets radiated. To compute the Huygens PSF, a grid of rays is launched through the optical system, and each ray represents a particular amplitude and phase wavelet. The diffraction intensity at any point on the image surface is the complex sum of all these wavelets, squared. The Huygens algorithm is more accurate than the FFT, but it is also slower, since the computation time is proportional to the pupil grid size squared times the image grid size squared.
The *Strehl ratio* (SR) is defined as the ratio between the peak of the PSF of the system and the peak of the diffraction limited PSF. By definition, the SR is a number between 0 and 1, with $SR = 1$ corresponding to a perfect system and $SR \approx 0$ corresponding to a very aberrated system. The SR is related to the RMS of the wavefront in the exit pupil of an optical system by the Maréchal relation [6]:

$$SR = \frac{1}{\exp{(2\pi\sigma)^2}} \tag{1.27}$$

where σ is the wavefront RMS expressed in units of wavelength. The Maréchal relation is an approximation and it is accurate to a couple of percent for RMS errors of 1/10 wave, with the difference diminishing for smaller errors (see [7] for more details).

1.4.4 Encircled energy

The encircled energy of a point source is the percentage of energy enclosed in a circle centered on the image and with a certain radius. By definition it is a number between 0% and 100%. It is common to plot the encircled energy as a function of the radius of the circle as in figure 1.10. In optical design software, the encircled energy can be determined in different ways. For example, the center of the image can be the centroid or the chief ray position and the calculation of the energy distribution on the focal plane can be based on the ray approximation (geometric encircled energy) or the wave approximation (diffraction encircled energy).
Also, the geometry of the aperture can be of different shapes depending on the application, the most common geometries being circles, squares or slits. Usually, image quality is estimated by giving the radius of the circle which contains 80% or 90% of the energy or, complementarily, giving the percentage of energy enclosed within a certain region (for example 2x2 pixels or a slit).

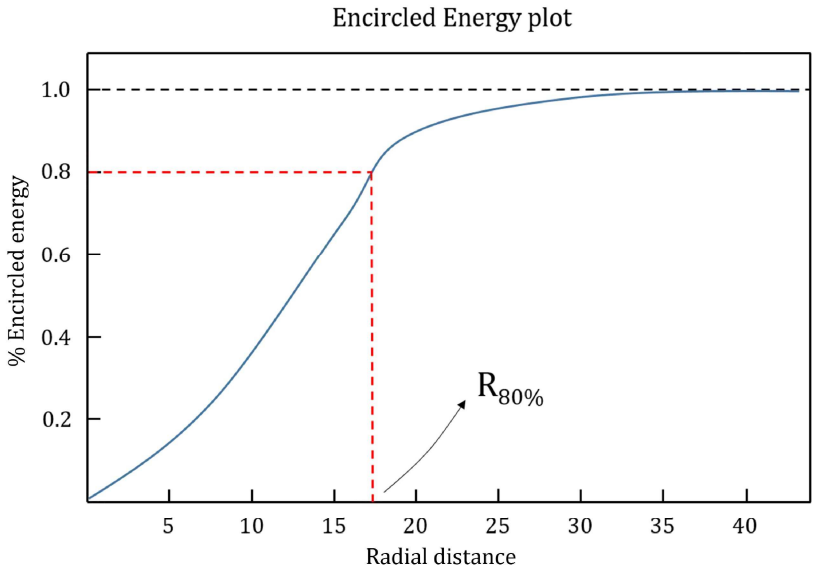

Figure 1.10: Typical encircled energy plot.

1.4.5 Modulation Transfer Function

Modulation Transfer Function (MTF) is a very common parameter used to describe the image quality delivered by an optical system. MTF specifies the response of an optical system to a periodic sine-wave pattern, as a function of its spatial frequency or period (see figure 1.11) [8]. In general, diffraction or optical aberrations decrease the contrast of an image and, as a result, high spatial frequency structures cannot be resolved. This is quantified by the modulation

depth:

$$M = \frac{I_{max} - I_{min}}{I_{max} + I_{min}} \tag{1.28}$$

When M=0, means that, although there is still a non-zero image irradiance level, there is no spatial variation of that irradiance, and the sine pattern is no more visible. Low levels of modulation depth are harder to discern against the unavoidable levels of noise inherent in any practical system. An MTF plot gives the modulation depth delivered by an optical system,

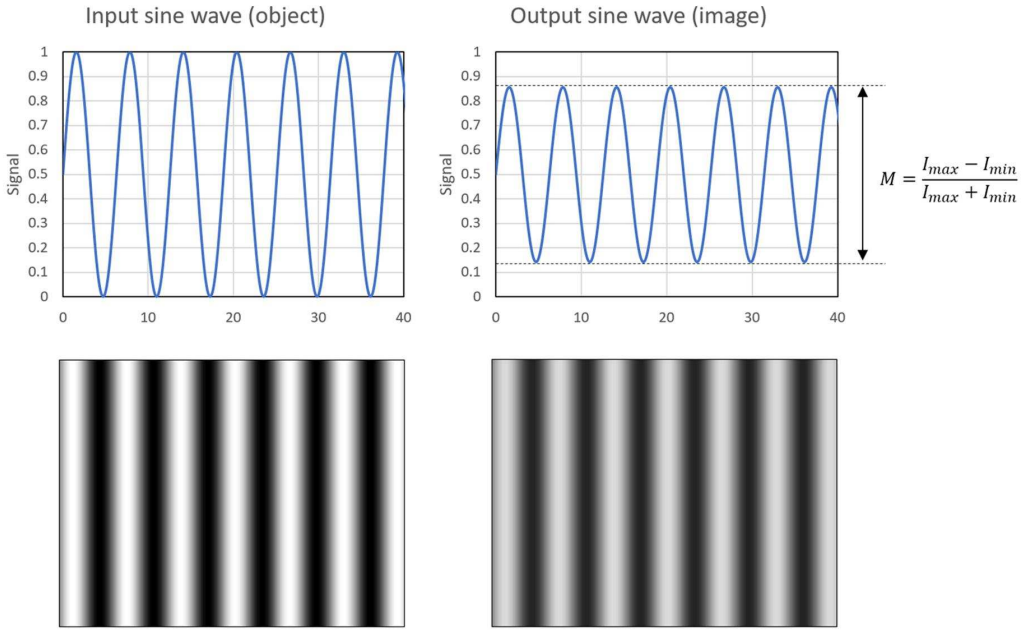

Figure 1.11: Input (left) and output (right) sine wave target with definition of the modulation depth.

as a function of the spatial frequency of the input sine wave pattern. Figure 1.12 shows an example of MTF plot for a three-lens objective. The modulation depth is close to $M = 1$ for very low spatial frequencies and falls below $M = 10\%$ for spatial frequencies higher than 150 cycles/mm.
As for the encircled energy, also the MTF can be calculated with geometrical approximation (geometric MTF) or with the Fourier Transform formalism (FFT diffraction MTF). The latter takes into account diffraction effects and is more accurate for diffraction limited optical systems.

1.4.6 Signal to noise ratio

The *Signal to Noise Ratio* (SNR) is another parameter used to quantify the quality of an image. The source radiation is considered the signal, while the noise is a radiation flux which is only partially dependent on the source, mixed with the signal reducing the image quality of the system. The noise is composed of several contributions. First of all, the *photon noise*, which is related to the statistics of the photons from the source. The photons follow Poisson statistics and the related noise is equal to the square root of the signal.

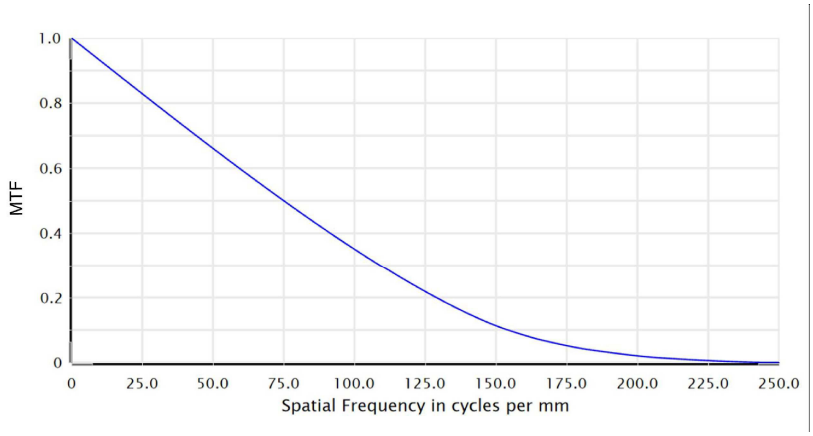

Figure 1.12: Example of an MTF plot for a three-lens system.

Then there is the *sky background* noise, which is the noise due to the diffuse light coming from the night sky. When you observe a FoV on the sky, part of the photons observed by the detector are coming from sources which are different from the target. It could be due to Sun light reflected by the moon, if visible, or the emission coming from extragalactic unresolved sources, in addition to the integrated Milky Way starlight. Moreover, interplanetary dust scatters and emits a fraction of the Visible Sun light, producing the zodiacal light. Such a component has a distribution which is a function of the FoV coordinates with respect to the ecliptic. The maximum of such emission can be found on the ecliptic plane, in the solar direction and in the opposite one. The zodiacal light generates almost 70% of the total visible light sky background on a moonless night.
Another source of noise is the emission from the Earth's atmosphere (*airglow*), which is due to the transitions between the electronic, rotational and vibrational energy levels of the molecules constituting the medium, together with the electronic recombination and the diffusing effect of such molecules on the sun light.
Then, there is the *thermal noise* which is particularly relevant at IR wavelengths and is due to thermal emission from optical components or the surrounding environment and the sky.
Stray-light noise is generated by photons scattered by optical components or from the structure of the telescope. Scattering is produced by small scale structures on the surfaces of optical components like residual micro-roughness from polishing or dust particles deposited on the surface. Sometimes, the term "stray-light" is used more generally to categorize all the un-wanted light generated by the instrument and the environment, and includes also the thermal background.
Concerning noise sources intrinsic to the detector, there is *Read Out Noise* (RON), which is introduced by the readout amplifier when trying to measure a very small packet of charge, and the *dark current*, due to electric charges released because of thermal agitation of the electrons inside the CCD itself.

1.4.7 Contrast and detection curves

Contrast quantifies the ratio between the brightness of two sources that can be simultaneously detected and distinguished by the system and fall within the same FoV. It is commonly used in direct imaging of exo-planets to quantify the ratio between the brightness of a planet and

that of the host star. A contrast of 10^{-6}, for example, means that the system is able to detect the light of a planet that is one-million times less luminous than the host star. In our Solar System, the contrast between the Earth and the Sun, as viewed from a distant star, is of the order of 10^{-10} at visible wavelengths, while the contrast between the Sun and Jupiter is of the order of 10^{-9} [9].

The maximum contrast detection achievable by an instrument depends on the angular separation between the two objects, being easier for objects with a wide separation. The detection curve of an instrument is a curve representing the achievable contrast as a function of the angular distance from the central star for a given SNR threshold. Usually a detection can be confirmed with high confidence when $SNR > 5$. A typical contrast curve appears in figure 1.13.

Coronagraphic instruments, i.e. instruments specialized in obtaining extremely high contrasts near a bright source, are generally optimized in a limited angular region around the star delimited by an "inner working angle" (or IWA) and an "outer working angle" (or OWA).

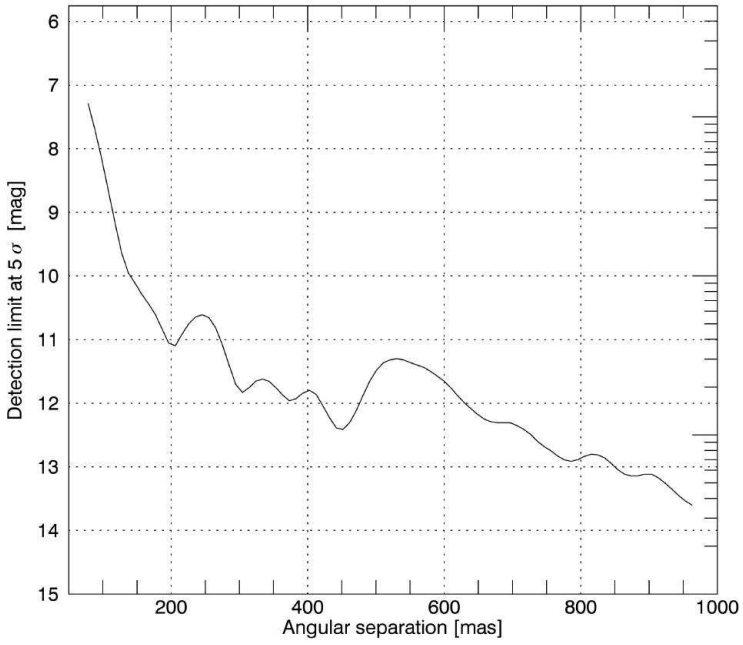

Figure 1.13: Typical detection limit curve as a function of angular separation.

Chapter 2

JANUS

2.1 Introduction

JANUS (Jovis Amorum ac Natorum Undique Scrutator) is an optical camera on the JUICE (JUpiter ICy moons Explorer) satellite, the large L class mission under development by ESA. JUICE is devoted to the detailed study of Jupiter and its moons, particularly Europa and Ganymede.The JUICE space mission is planned for launch in 2022 and arrival at Jupiter in 2030, and it will operate for at least three years, making detailed observations of the Jovian system. The JANUS science objectives are:

- Characterize Ganymede, Callisto, and Europa as planetary bodies, including their potential habitability, with special focus on Ganymede;
- Characterize and study the physical properties of other satellites of the Jupiter system, including Io, the irregular and inner satellites;
- Perform a physical characterization of the ring system;
- Study the external layers (down to the troposphere) of Jupiter's atmosphere;
- Study the magnetosphere in which Jupiter and its satellites are embedded, and the complex interactions taking place in the Jovian system.

A satisfactory answer to all these questions requires also measurements taken by an imaging system with optimum performance. Such a system will have a major role in the mission, not only with its camera-specific scientific results, but also in providing the necessary context for most of the other instruments on-board JUICE, as for instance the Digital Terrain Model (DTM) of a few regions of Ganymede required by RIME (Radar for Icy Moons Explorations) for its topographic correction.

2.2 Scientific goals

2.2.1 Geology of Ganymede, Callisto and Europa

The detailed investigation of the Galilean satellites (Ganymede, Europa, and Callisto), which are believed to harbour subsurface water oceans, is central to elucidating the conditions for habitability of icy worlds in planetary systems in general. The study of the Jupiter system

also offers the best opportunity for understanding the origins and formation of the gas giants and their satellite systems. The JUICE camera system JANUS will determine the formation and characteristics of magmatic, tectonic, and impact features on the satellites, relate them to surface forming processes, constrain global and regional surface ages, and investigate the processes of erosion and deposition.
The investigation of structural elements is necessary for a detailed study of surface processes, their evolution and the interaction between subsurface, surface and atmosphere. The performance of JANUS is ideal to address many key science questions related to the structural evolution of Ganymede's icy shell, such as the types of deformation features, the sources of the deformation forces, the thickness of Ganymede's lithosphere, etc. The global coverage of Ganymede with $\leq 400m/px$ will enable complete mapping of the basic geologic surface units (i.e. light terrain, dark terrain, impacts). After the first analysis from global mapping and kinematic studies, a close-up inspection of selected features with resolution $\approx 100m/px$, will allow more detailed observations required to determine the true mechanical nature of surface features and to develop models of their origin and evolution. Finally, very high-resolution images ($< 100m/px$) are needed to analyze the small-scale architecture of folds and faults and study their key properties.
Monochromatic high resolution images with $< 50m/px$ down to $< 10m/px$ or color images with resolution $< 500m/px$ will also allow scientists to study the cryovolcanic structures on Ganymede and Europa to decipher their origin. In addition, spectral information derived from JANUS colour filters will provide insight into the compositional differences of possible cryovolcanic features.
The study of impact craters is an extremely important indicator for many properties of planetary bodies, such as:

- rheological properties (related to plastic deformation) of a planetary surface and regional differences
- subsurface structure
- the nature of impactors (asteroids or comets)
- time-dependent morphologic expressions of specific properties
- thermal history of a planet or satellite

Moreover, craters are subject to resurfacing processes such as erosion, tectonism, volcanism or superposition of new impact craters. Thus, craters play an important role in tracing the history of a planet and of its environment. JANUS will be able to provide a global coverage of craters morphologies at resolutions $< 400m/px$ for Ganymede and an almost global coverage at resolutions $< 1km/px$ for Callisto.
JANUS will also help in studying the internal structure and dynamics of the Galilean icy satellites by determining the mean spin pole direction (obliquity), the forced nutation of the spin pole at the orbital period (the expected value of Ganymede obliquity ranges between $0.015°$ and $2°$, depending on the presence or absence of a subsurface ocean), and the amplitude of the forced libration at the orbital period.
Finally, with multi-spectral imaging, it will be possible to study the albedo changes of water ice as well as non-ice materials. Multispectral imaging will allow us to spectrally characterize the dark non-ice contaminants, to distinguish between different possible dark materials, and to derive their varying abundance across Ganymede's surface.

2.2.2 Observations of Io and Jupiter

Io's volcanic activity significantly affects the Jovian system, including causing aurorae on Jupiter and transporting sulfur to Jupiter and Europa. JANUS will help to investigate Io's tidal heating by monitoring its volcanic activity, constraining magma composition and eruption styles, detecting previously unknown active volcanic centers and surface changes from plumes and other activity. In particular, surface changes can be detected by repeated observations at similar phase angles and at different wavelengths.
The observations of Jupiter will be mainly devoted to the study of its atmosphere. The three uppermost layers of the atmosphere can be investigated by imaging observations. In particular JANUS will:

- Study the troposphere, imaging the active dynamical processes, cloud systems, waves, vortices and other instabilities and detecting lightning;
- Observe stratospheric variations due to water meteorology and disturbances from large vortices, such as the Great Red Spot;
- Investigate the upper atmosphere by imaging auroral activity and polar hazes.

In addition to the study of Jupiter's atmosphere, it will be possible also to study the ring system of Jupiter which is of great importance to understand how faint rings can form from the meteoric bombardment of satellites and then evolve under a variety of forces and external events. High-accuracy astrometric positions of all the moons can be obtained during the tour of the Jovian system. Based on Cassini data, an accuracy of $< 10km$ may be expected for the Galilean moons, which will greatly improve the determination of tidal dissipation in both Io and Jupiter.

2.3 Mission architecture

The mission architecture is described in detail in the Consolidated Report on Mission Analysis (CReMA) [10]. The mission is based on a launch from Kourou with Ariane 5 ECA with direct escape. The baseline launch is in 2022. The interplanetary transfer sequence is case dependent and relies on gravity assist with Venus, the Earth and Mars.
All interplanetary transfers are based on an initial Earth to Earth arc, which is justified by the strong dependence of the launcher performance on the escape declination. It is also necessary to benefit from a Lunar-Earth gravity assist.
After a variable time of flight (7.4 to 8.9 year for the launch in 2022), the spacecraft is injected around Jupiter via a capture maneuver. An initial Ganymede swing-by is performed before the capture maneuver in order to reduce the magnitude of the latter.
Following a series of Ganymede swing-bys that reduce the orbit energy, the inclination and the infinite velocity, the spacecraft is transferred to Callisto with the conditions necessary to initiate the Europa science phase.
Later on, the spacecraft initiates the Europa science phase, which is composed of two fly-bys with closest approach at 400 km altitude and low infinite velocity. Because of the low distance between Europa and Jupiter, special care was attached to the radiation dose minimisation. The duration of this phase is about 35 days.
The Jupiter high latitudes phase follows the Europa science phase: it is based on a series of 1:1

resonant transfers with Callisto, which raise the inclination with respect to Jupiter's equator to a maximum value of 22 deg. When the maximum inclination is reached, the spacecraft is injected into a 4:3 resonant transfer. The duration of this phase is around 6 months.
The spacecraft is then transferred from Callisto to Ganymede in two steps: the first step uses Callisto to reduce the infinite velocity with respect to Ganymede. Further infinite velocity leveraging is obtained in a second step via a low energy endgame with Ganymede: a series of 5 close encounters with Ganymede is followed by a gravitational capture with the moon.
The science phase around Ganymede is decomposed into an elliptic sub-phase with a period close to 12 hours and a low altitude circular sub-phase. The elliptic sub-phase lasts 120 days during which the eccentricity quickly decreases, remains close to zero, before finally building up again under the influence of Jupiter. The circular sub-phase is performed at an altitude of 500 km for 160 days.
At the end of this phase the eccentricity will naturally build up until the spacecraft impacts the surface in an uncontrolled manner. The total duration of the Jupiter tour is 3.5 year.

2.4 Spatial resolution and approach distances

Table 2.1 summarizes the results of the preliminary JUICE mission analysis with closest flyby distances to the surfaces of Jovian satellites and resulting ground sampling distances of JANUS before Ganymede orbit insertion [11]. Figure 2.1 gives a graphical presentation of the ground sampling distance and resulting image swaths in comparison with the mission analysis results. JANUS will have a spatial resolution $<$ 10m/pixel during the Ganimede Circular Orbit at 500km of altitude (GCO-500). From the 10 irregular satellites analyzed so far, only two can be spatially resolved by JANUS; all others will represent point sources. Observation conditions for the remaining about 50 Jovian satellites shall be analyzed in the future.

2.5 Instrument requirements

The top level requirements to fulfill the JANUS scientific objectives are translated in a set of instrument low level requirements which are contained in a dedicated document called "JANUS-Instrument Requirements Specifications" [12]. The main scientific aspects that the optical design has to fulfill are related to the image quality, spatial and spectral coverage and resolution capabilities during the different observation phases and operation conditions. Some of the primary requirements that have to be satisfied are:

1. light collection through an optical system allowing enough overall throughput
2. maintain optical and mechanical stability in all operational phases, under all expected thermal conditions
3. provide active or passive thermal control
4. provide optics and detector protection from contamination and sunlight
5. possibility to acquire images in the spectral range $350 - 1050nm$ with some sensitivity at $1064nm$ to allow co-alignment with the laser altimeter;

Target	Distance to surface [km]	Ground sampling [km/px]
Jupiter	593587	8.9
Io	423574	6.35
Europa	403	0.006
Ganymede	301*	0.0045
Callisto	199	0.003
Metis	537221	8.1
Adrastea	536815	8.1
Amalthea	484211	7.3
Thebe	519141	7.8
Themisto	3969653	59.5
Leda	5157103	77.4
Himalia	7437512	111.6
Lysithea	6511680	97.7
Elara	3435558	51.5
Ananke	15950989	239.3
Carme	16084058	241.3
Pasiphae	10738013	161.1
Sinope	3507883	52.6
Callirrhoe	7328898	109.9

Table 2.1: JUICE distance to surface (not center), JANUS ground sampling distance and date during closest approach based on current JUICE orbit prediction (* distance to Ganymede before Ganymede orbit insertion).

6. optics entrance pupil should be at least $100mm$ equivalent diameter;
7. the field of view subtended by one pixel shall be $IFOV = 15\mu rad$ ($\approx 3arcsec$);
8. the field of view shall be $> 30mrad$ ($1.7deg$) on cross-track direction and $> 22.5mrad$ ($1.3deg$) on along-track direction;
9. the global quantum efficiency shall be $> 60\%$ EOL (at End Of Life) at the central wavelength;
10. global Modulation Transfer Function (MTF) at Nyquist frequency shall be $> 15\%$ (goal of 20%);
11. the contribution of straylight and ghosts to the signal shall remain negligible (i.e. their contribution shall be within the noise) in the different observation conditions;

Some of the requirements come directly from the ESA baseline requirements, while others are created at instrument-level with the purpose to detail the more general requirements in a way to be applicable to the different JANUS subsystems. In particular, the parameters have been fine-tuned to allow JANUS to perform low, medium and high-resolution imaging on different targets in the Jupiter system, taking advantage of the complex mission design. In this way, instrument operations will be flexible enough to optimize the acquisition parameters with respect to the many different observation requirements and conditions that JANUS will

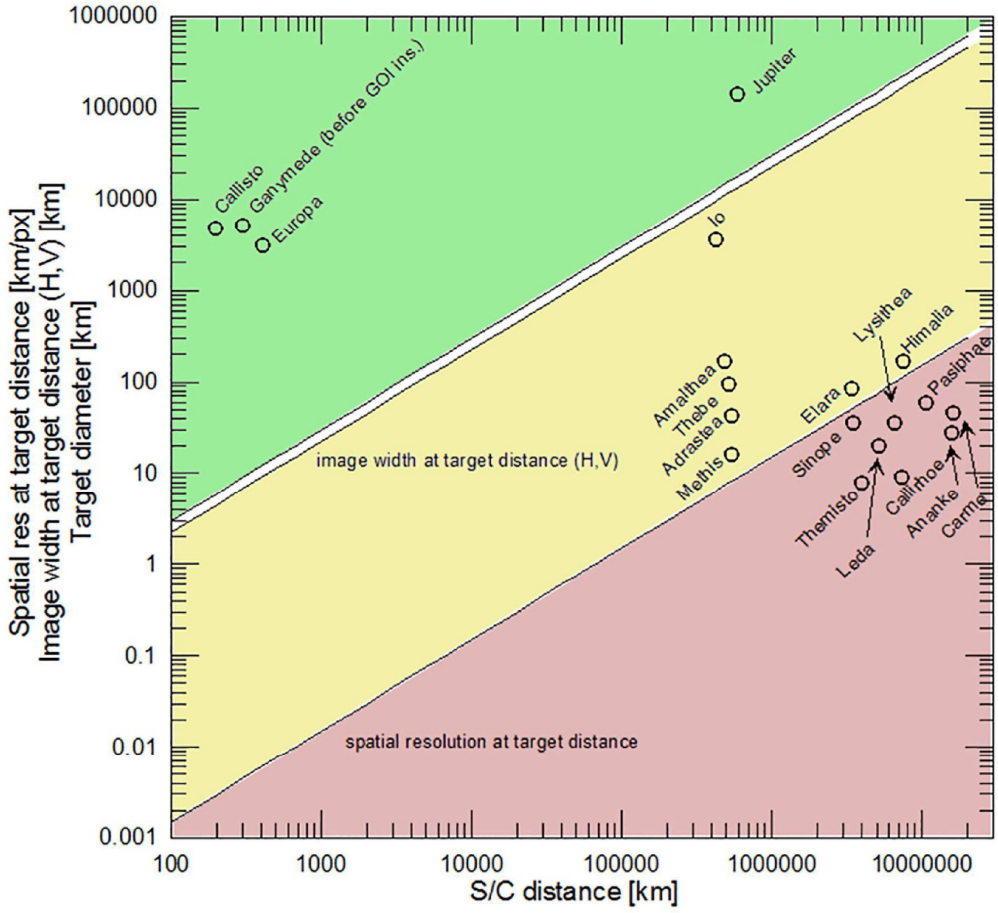

Figure 2.1: JANUS spatial resolution and image swaths (2000 x 1504 pixel) compared to closest Space-Craft (S/C) distance and diameter of Jovian satellites. The red region is for non-resolvable objects, the yellow region for resolvable objects fitting within the FoV, and the green region for resolvable objects bigger than the FoV.

face. The instrument design should allow adjustment of the resolution through binning, the field of view through windowing, the signal levels and SNR through integration time, and the instrument calibration parameters through in-flight calibration and data pre-processing;

2.6 Optical design

2.6.1 First order optical design

Requirements 4 to 7 of the previous section, along with the detector specifications, are useful to trace the first order properties required for JANUS. The selected detector is a $2000 \times 1504\ px$ back-side illuminated CMOS sensor from E2V with square pixels of $7\mu m$ pitch. The pixel size, along with the IFOV requirement, sets an effective focal length of $f_{eq} = 467mm$. The entrance pupil diameter of $100mm$ translates to a quite fast focal ratio of $f/4.67$. All the specifications of the optical design are summarized in table 2.2. Different optical solutions have been

Parameter	Value
Entrance pupil diameter	100 mm
Effective focal length	467 mm
F/#	4.67
Plate scale	15 $\mu rad/px$
Field of view	1.72×1.29 $degrees^2$
Detector format	2000×1504 px^2
Pixel size	7 μm
Spectral range	350 –1050 nm

Table 2.2: JANUS optical specifications

investigated to achieve the requirements for JANUS. At a first stage a catadioptric design was studied, but it was rejected because it was not effective in providing a sufficient image quality over the whole spectral range. Then, an all-reflective "*Three Mirror Anastigmat*" (TMA) design which avoids chromatic aberrations was proposed. Finally, the configuration has been changed to a modified Ritchey-Chrétien telescope to reduce mass. The latter two configurations are described in the following sections

2.6.2 Third order analytical solutions

The second step in the design of the telescope was to find analytical solutions that minimize the primary Seidel aberrations, in order to have a good starting point for further optimizations with ray tracing software. Allowing for the use of aspheric surfaces, there are ten degrees of freedom for a TMA, enough to correct for the major sources of aberration. Many choices can be made for the parameters that describe the optical system. For instance, a very natural choice from a sequential ray-trace point of view are the following mutually independent parameters: the entrance pupil position t_1, the object position s_1, the three mirrors surface curvatures c_i and conic constants k_i, the distance between primary and secondary mirror d_1 and the distance between secondary and tertiary mirror d_2. Some of them are fixed by the optical prescriptions for JANUS (such as the effective focal length and the object position), while the others can be used to eliminate third-order aberrations and to put geometrical constraints on the system. The constraints used for the TMA design of JANUS are the following:

1. object at infinity
2. entrance pupil on the secondary mirror
3. system focal length $f = 467mm$
4. Spherical aberration = 0
5. Coma = 0
6. Astigmatism = 0
7. Field curvature = 0

8. $d_1 = -d_2$

As mentioned above, there are ten degrees of freedom in total but we use only eight conditions, meaning that there are two free parameters to play with. The approach followed is similar to that presented in Dohlen et al. (1996) [13] i.e. building equi-conic contour maps of the mirrors as a function of two carefully chosen free parameters. The two free parameters can be chosen according to our needs, but it is necessary to remember that the choice can't be arbitrary. In fact the two free parameters should be independent from the other eight, in order to fully characterize the optical configuration. In our specific situation, we are interested in the back focal clearance (to allocate a filter wheel) and the overall size of the system. The latter can be characterized by the back focal length (BFL) i.e. the distance between M3 and the focal plane, while the former is given by the difference between the BFL and the distance between M2 and M3. Both these parameters are independent from the other constraints, and fixing a value for them gives a unique solution for the equations that characterize the optical system. The equations to compute third-order aberrations of a three-mirror system can be found in Korsch (1991) [14]. Here, I will use his notation:

- s_1 is the initial object distance, $v_1 = 1/s_1$ is the reciprocal
- s'_3 is the final image distance, $v'_3 = 1/s'_3$ is the reciprocal
- t_1 is the initial entrance-pupil distance from the primary mirror
- $d_1,\ d_2$ are the mirror separations
- $\Omega_1,\ \Omega_2$ are the paraxial ray height ratios defined as: $\Omega_i = h_{i+1}/h_i$ (see figure 2.2)
- $c_1,\ c_2,\ c_3$ are the mirror curvatures
- $k_1,\ k_2,\ k_3$ are the mirror conic constants

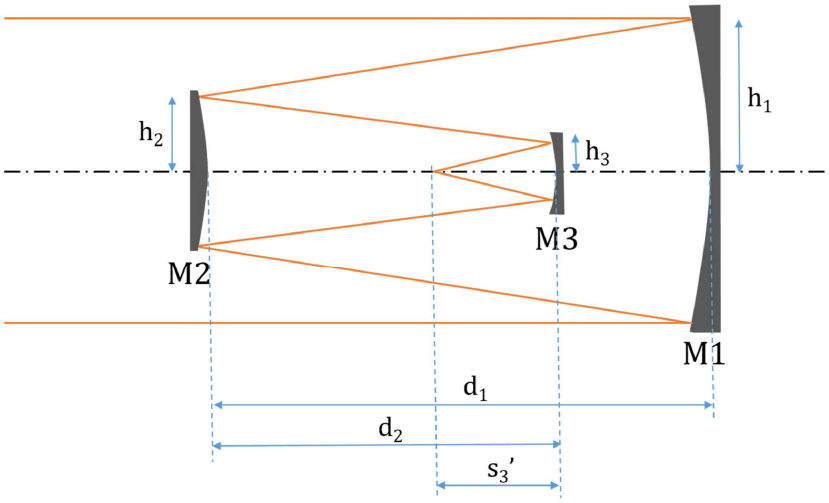

Figure 2.2: definitions of the parameters for a three-mirror system.

With the above definitions, the aberration coefficients for spherical aberration (A), coma (B), astigmatism (C) and field curvature (c_p) are respectively [14]:

$$A = \tau_1^{-4}\left(c_1^3\Delta\delta_1 - \Omega_1^4 c_2^3\Delta\delta_2 + \Omega_1^4\Omega_2^4 c_3^3\Delta\delta_3\right)$$

$$B = \tau_1 t_1 A + \tau_1^{-2}\left[\frac{1}{4}\left(v_1^2 - \Omega_1^2\Omega_2^2 v_3'^2\right) - \Omega_1^3 d_1 c_2^3\Delta\delta_2 + \Omega_1^2\Omega_2^3\left(\Omega_1\Omega_2 d_1 - d_2\right)c_3^3\Delta\delta_3\right]$$

$$\begin{aligned} C = & -2\tau_1^2 t_1\left(t_1 + \tau_1\frac{d_1}{\Omega_1}\right)A + 2\tau_1\left(2t_1 + \tau_1\frac{d_1}{\Omega_1}\right)B - \\ & - \frac{1}{2\Omega_1}\left[\Omega_1\Omega_2 v_3'^2\left(\Omega_1\Omega_2 d_1 - 2d_2\right) + v_1^2 d_1\right] + \\ & + v_1 + v_3' - 2\Omega_2^2 d_2\left(\Omega_1\Omega_2 d_1 - d_2\right)c_3^3\Delta\delta_3 \end{aligned} \tag{2.1}$$

$$c_p = \frac{\left(1-\Omega_1\right)^2}{\Omega_1 d_1} - \frac{\left(1-\Omega_2\right)^2}{\Omega_2 d_2} - v_1 - v_3'$$

where $\tau_1 = 1 - v_1 t_1$ is the image scale coefficient and the $\Delta\delta_i$ are the Cartesian deviations which are related to the conic constants by:

$$\begin{aligned} k_1 = & \Delta\delta_1 - \left(\frac{1-\Omega_1 - v_1 d_1}{1-\Omega_1 + v_1 d_1}\right)^2 \\ k_2 = & \Delta\delta_2 - \left[\frac{\Omega_1 d_1\left(1-\Omega_2\right) - d_2\left(1-\Omega_1\right)}{\Omega_1 d_1\left(1-\Omega_2\right) + d_2\left(1-\Omega_1\right)}\right]^2 \\ k_3 = & \Delta\delta_3 - \left(\frac{\Omega_2 v_3' d_2 - 1 + \Omega_2}{\Omega_2 v_3' d_2 + 1 - \Omega_2}\right)^2 \end{aligned} \tag{2.2}$$

The surface curvatures are related to the other system parameters by the following equations:

$$\begin{aligned} c_1 = & \frac{1-\Omega_1}{2d} \\ c_2 = & \frac{1}{2}\left(\frac{1-\Omega_1}{\Omega_1 d} - \frac{1-\Omega_2}{d}\right) \\ c_3 = & \frac{1}{2}\left(\frac{\Omega_2 - 1}{\Omega_2 d} + v_3'\right) \end{aligned} \tag{2.3}$$

From the definitions above, the constraints for the optical design are determined by the following conditions:

1. focal length: $f_{eq} = 1/(\Omega_1\Omega_2 v_3') = 467mm$
2. object position: $v_1 = 0$ and $\tau_1 = 1$
3. entrance pupil on the secondary mirror: $t_1 = -d_1/\Omega_1$
4. spherical aberration: $A = 0$
5. coma: $B = 0$
6. astigmatism: $C = 0$
7. field curvature: $c_p = 0$
8. mirror separation: $d_1 = -d_2 = d$

To find the equi-conic contour maps, it is necessary to calculate the values of k_1, k_2 and k_3 from each pair of input free parameters (the back focal extraction $v_3' - d$ and the back focal length v_3'). The procedure adopted is to find the paraxial ray height ratios Ω_1 and Ω_2 from conditions 1,7,8 and then to solve conditions 4,5,6 for the Cartesian deviations $\Delta\delta_i$. Conditions 2 and 3 are simply substituted inside the equations. To find Ω_1 and Ω_2, it is necessary to solve a system of second order equations. Thus, there are two possible solutions for the paraxial ray height ratios. Calling for simplicity of notation $k_f = f_{eq}/d$ and $k_v = 1/(v_3' d)$, the paraxial ray height ratios are given by:

$$\begin{aligned} \Omega_2 =& \frac{k_f\left(4k_v+1\right) \pm \sqrt{k_f^2\left(4k_v+1\right)^2 - 4k_f k_v\left(k_f+k_v\right)^2}}{2k_f\left(k_f+k_v\right)} \\ \Omega_1 =& \frac{k_v}{k_f\Omega_2} \end{aligned} \tag{2.4}$$

The solution of conditions 4,5,6 together with constraints number 2 and 3, gives the following equations:

$$\begin{aligned} \Delta\delta_3 =& \frac{2v_3' - \Omega_2 v_3'^2\left(\Omega_1\Omega_2 d + 2d\right)}{-4\Omega_2^2 d\left(\Omega_1\Omega_2 d + d\right)c_3^3} \\ \Delta\delta_2 =& \frac{-\Omega_1^2\Omega_2^2 v_3'^3 + 4\Omega_1^2\Omega_2^3\left(\Omega_1\Omega_2 d + d\right)c_3^3\Delta\delta_3}{4\Omega_1^3 d c_2^3} \\ \Delta\delta_1 =& \frac{\Omega_1^4}{c_1^3}\left(c_2^3\Delta\delta_2 - \Omega_2^4 c_3^3\Delta\delta_3\right) \end{aligned} \tag{2.5}$$

Finally, equations 2.2 can be used to find the conic constants from the Cartesian deviations. In the case of JANUS, one pair of solutions for Ω_1 and Ω_2 gives very high and unreasonable values for the conic constants and they are not considered as feasible solutions. The other pair of solutions, on the other hand, gives a set of very interesting systems to use as a starting

point for the ray-trace optimization.
The equi-conic contour maps for the three mirrors of JANUS are shown in figure 2.3 for a reasonable range of back focal length and back focal extraction. It appears that, for the range

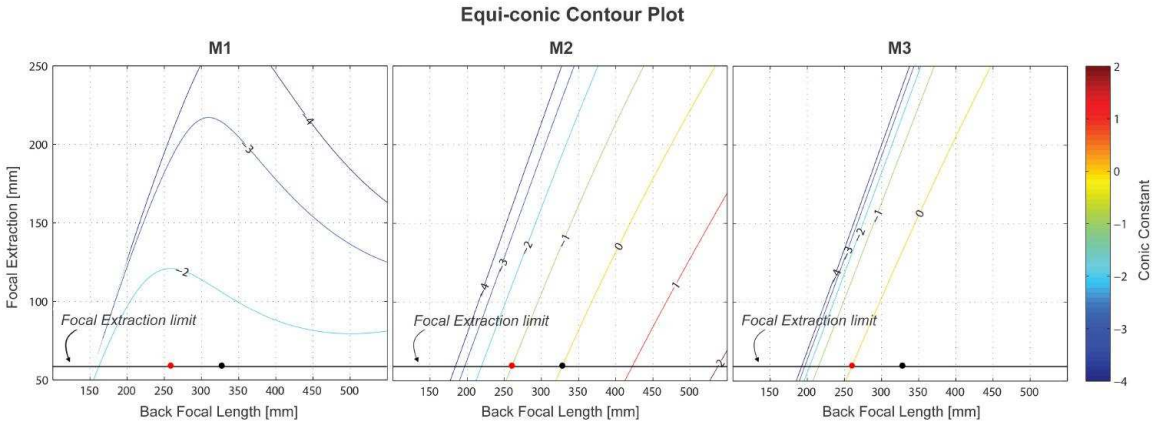

Figure 2.3: Equi-conic contour plots for M1, M2 and M3 as a function of BFL and focal extraction.

of back focal lengths and back focal clearances under examination, there is no solution that gives a spherical ($k_1 = 0$) primary mirror while both the secondary and the tertiary can be spherical in some configurations. It would be interesting to find some solutions in which both M2 and M3 are spherical, which means that the equi-conic contours relative to $k_2 = 0$ and $k_3 = 0$ intersect at some point, but unfortunately this is not the case. Among all the systems with a spherical mirror, we chose the most compact systems allowed by the requirements. In particular, in order to have enough room for the filter wheel, a minimum back focal extraction of $60mm$ is necessary. At this point, we are left with two possible systems which are denoted by the black (spherical secondary) and red (spherical tertiary) points in figure 2.3. Since the secondary coincides with the system stop, which is more sensitive to aberrations, and since the manufacturing of spherical surfaces is easier, and better quality can be achieved with respect to aspheric surfaces, we decided to use the spherical-secondary solution. Moreover aspheric convex mirrors are more difficult to test with respect to concave ones. The mirror parameters of the spherical-secondary solution are summarized in table 2.3

Parameter	**Radius of curvature [mm]**	**conic constant**
M1	-994.69	-1.680
M2	-315.30	0.000
M3	-461.62	0.195
d	268.58 mm	

Table 2.3: Parameters for the spherical secondary mirror solution

2.6.3 Ray-tracing optimization

For the ray-tracing optimization and analysis we used a sequential model with the software Zemax. With respect to the third-order design described in the previous section, which provides an on-axis solution, we considered an off-axis variant (with off-axis field of view and on-axis pupil) to take full advantage of the contrast capabilities of an un-obstructed design [15]. The same configuration was also adopted for the Narrow Angle Camera [13] of the Rosetta satellite, which has proven to be capable of taking extraordinary images. The final configuration includes the filters and a window just in front of the detector for radiation shielding. The merit function used for the optimization process of the TMA consists of the following conditions:

- the distance between the primary and the secondary is equal to the distance between the secondary and the tertiary
- the focal extraction is forced to be greater than 60 mm
- all the mirrors share the same optical axis
- the vertical displacement of M1 and M3 is forced to satisfy the following condition for first order stray light rejection: the ray passing through points A and B (in figure 2.4) should fall out of M3 and the ray passing through points C and B (in figure 2.4) should fall out of M1. This means that, by proper internal baffling, M3 cannot be illuminated directly by sources out of the field of view and that light scattered by M1 cannot directly reach the filters and the detector.
- The field of view is forced to be off-axis in order to not obstruct the incoming beam with the secondary mirror.
- M2 is fixed to be spherical to reduce manufacturing and alignment complexity.

In addition to these constraints, the optical quality of the system over the whole field of view has been maximized in terms of polychromatic MTF.

The system resulting from the optimization is very similar to the starting third-order solution. It has an on-axis, virtual entrance pupil placed to the right of M1 and M3 (in figure 2.4), at a distance of about $850mm$ from the vertex of M2. The field is about 7.7 degrees off-axis in order to have an un-obstructed pupil. Table 2.4 summarizes the characteristics of each surface. The first mirror is an off-axis section of a hyperboloid with a diameter of about $132mm$. The secondary mirror is spherical with a diameter of $50mm$ and defines the optical stop of the system. The tertiary mirror is an off-axis section of an oblate ellipsoid with diameter of about $96mm$. The focal plane is located $335mm$ from the tertiary mirror with a focal extraction of approximately $60mm$ with respect to M2, allowing enough space for the filter wheel.

The JANUS camera will have 13 optical filters with different bandwidth and central wavelength. The filter's substrate is assumed to be fused silica, characterized by an extremely low coefficient of thermal expansion ($CTE = 0.55 \cdot 10^{-6}[1/K]$) and high transmittance over the whole spectral range. Moreover, fused silica has been demonstrated to maintain unvaried optical properties also when exposed to high energy radiation fluxes ($\approx$ 10 MRad [16]). Their thickness is about 3 mm, varied slightly from filter to filter in order to minimize the chromatic focal shift at the different wavelengths. All the filters have been tilted by about 5

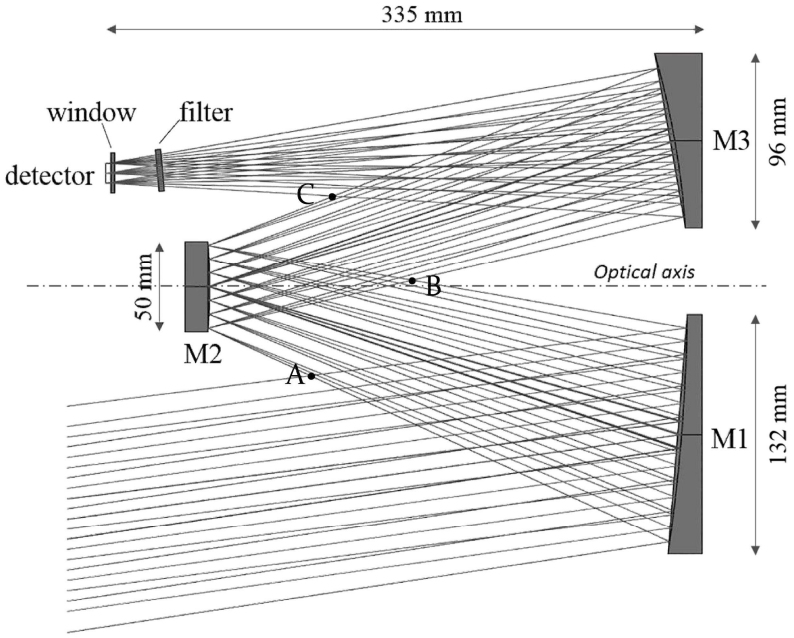

Figure 2.4: JANUS 2D optical layout

Surface	**Radius of curvature* [mm]**	**conic constant**	**Diameter[mm]**	**Aperture decenter [mm]**
M1	−991.623 (cc)	-1.6307	132	81.56
M2	−313.986 (cv)	0.0000	50	0.00
M3	−459.744 (cc)	0.2021	96	80.80

Table 2.4: Parameters of the optical surfaces. *"(cc)" stands for concave, "(cv)" for convex.

degrees with respect to the optical axis to maintain perpendicularity with the chief ray and maximize optical quality. The flat window in front of the detector is 2 mm thick with a gap of 1 mm with respect to the detector. The window substrate has been assumed to be sapphire due to its resistance and good transmittance over the full wavelength range. The detector format is rectangular with 2000x1504 pixels^2 and the short side of the detector is parallel to the scanning direction (along track) of the camera, while the long side is perpendicular to it (cross track), in order to maximize the imaging coverage during the planet/satellite surface scan.

2.7 Nominal image quality

The nominal image quality has been estimated using both the spot diagram and the diffraction MTF. Figure 2.5 shows the spot diagram for nine different positions in the field of view. The rays fall within the Airy disk, showing that the all-reflective design and the use of three mirrors gives enough degrees of freedom to obtain a diffraction limited optical quality over the whole field of view. The result is also confirmed by the diffraction polychromatic MTF

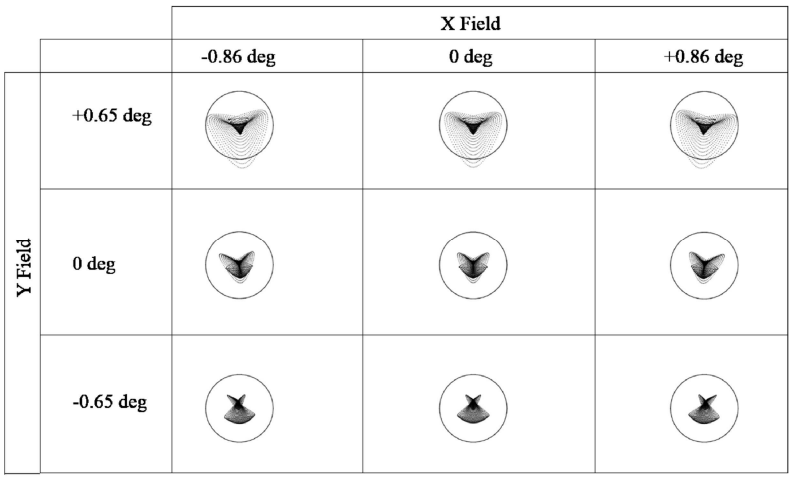

Figure 2.5: Spot diagram for nine field positions. The circle represents the size of the Airy disk at $\lambda = 0.7\mu m$.

(figure 2.6). The maximum spatial frequency considered is the Nyquist frequency equal to:

$$f_{Nyq} = \frac{1}{2\ pixel\ pitch} = 71.4\ cycles/mm \tag{2.6}$$

The MTF at the Nyquist frequency is greater than 63% over the whole field of view and very close to the diffraction limited value of $MTF \approx 70\%$.

2.8 Effects of misalignment

The effect of non-perfect instrument alignment on the MTF has been evaluated with a Monte Carlo simulation. The parameters considered for this tolerance analysis are decenter, defocus and tilt of the optical elements. A preliminary sensitivity analysis, conducted before the Monte Carlo simulation, showed that the secondary mirror is more tolerant to tilt with respect to the primary and tertiary mirrors, and that the filter and the window are very tolerant both for decenter, defocus and tilt. Based on the sensitivity analysis, an error budget for every optical element has been estimated and fed into the simulation. The positioning errors used for the simulation are listed in table 2.5. The empty cells refer to misalignments that do not produce any effect because of the symmetries of the surface shape. The Monte Carlo simulation consists of 1000 different realizations of misalignment. For each one, we calculated the smallest value of the Nyquist frequency MTF over the FoV, and we used it as a figure of merit to classify the image quality deterioration. The MTF of the worst system simulated is represented in figure 2.7. Compared to the nominal system, the performance is less uniform across the FoV with a loss of the order of $25 - 30\%$ MTF for the worst field point and a loss of $\approx 13\%$ on average.

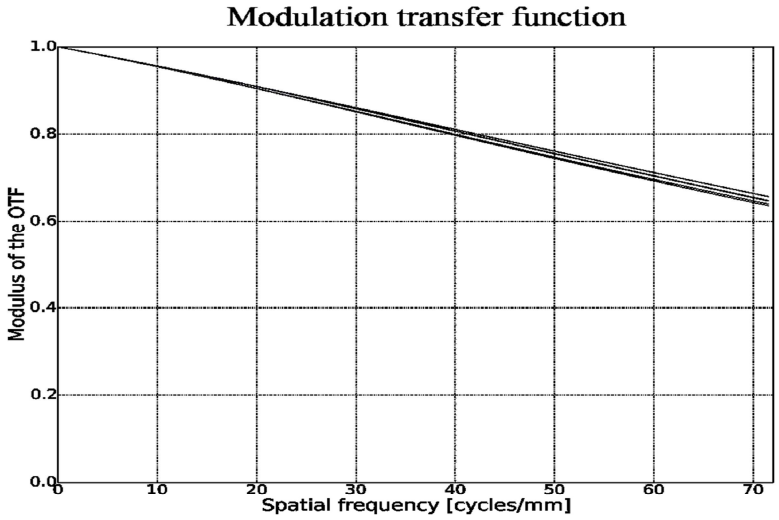

Figure 2.6: Polychromatic diffraction MTF over the whole spectral range for different field positions.

Element	defocus	decenter x	decenter y	tilt x	tilt y	tilt z
M1	±10	±40	±40	±0.5	±0.5	±0.5
M2	±10	±40	±40	±1.0	±1.0	-
M3	±10	±40	±40	±0.5	±0.5	±0.5
filter	±1000	±1000	±1000	±30	±30	-
window	±1000	±1000	±1000	±30	±30	-
detector	±10	±20	±20	±2	±2	-

Table 2.5: Input tolerance errors for the Monte Carlo simulation. Lengths are in μm, angles are in $arcmin$.

2.9 Sensitivity to temperature variations

To test the effects of temperature variations on the image quality, a preliminary thermal analysis has been performed. The analysis is based on a simplified model that takes into account the movements generated by thermal expansion (or contraction) of the supporting structure. The simulation has been done with the ray-tracing software Zemax. To simulate the effect of thermal expansion/contraction we made the following simplifications and assumptions:

- Temperature of the optical bench is homogeneous
- M1 and M3 move along the optical axis with respect to M2 due to thermal variations in the distance between the secondary and the other two mirrors (figure 2.8)
- M1 and M3 are supposed to be fixed to a plate which dilates or contracts due to thermal variations, changing the vertical distance between M1 and M3 (figure 2.8)

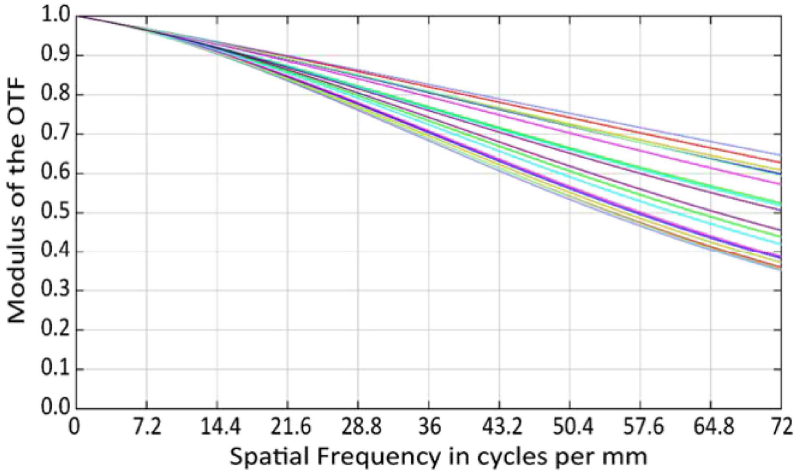

Figure 2.7: Polychromatic MTF of the "worst case" Monte Carlo system for different field positions.

- The detector moves along the optical axis for temperature variations of the material between the M2 supporting pad and the detector (figure 2.8)
- The mirror material is Zerodur (CTE 0.02 ppm/K). Thus, the variation in the shape of the mirrors is negligible.
- The only variable optical properties are the refractive index and Abbe number of the filters and of the window
- We considered two different materials for the mechanical structure: silicon carbide and carbon fiber (used CTEs are reported in table 2.6). Carbon fiber is used for the tube connecting M2 to the mounting pad of M1 and M3 while silicon carbide is used for all the rest of the structure.

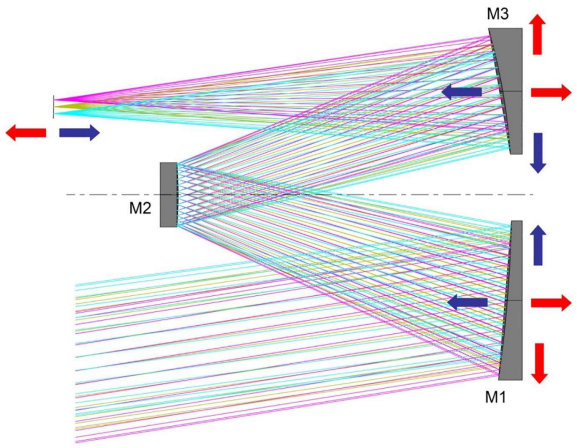

Figure 2.8: Movement scheme of the optical elements used for the thermal sensitivity analysis.

Material	**CTE** $[(1/°\mathrm{C}) \times 10^{-6}]$
Silicon carbide	2
Carbon fiber	0.5

Table 2.6: CTE values used in the model

The optical design is optimized for $T = -40°\mathrm{C}$ and temperature variations of $\Delta T = \pm 20°\mathrm{C}$ are considered. This temperature range has been adopted to evaluate the optical performance of the system in a wide (and pessimistic) range. The optical quality is evaluated in terms of polychromatic MTF at the Nyquist frequency over the whole FoV. The nominal MTF at $T = -40°\mathrm{C}$ is $> 62\%$, at $T = -20°\mathrm{C}$ the $MTF > 57\%$ and at $T = -60°\mathrm{C}$ the $MTF > 55\%$. Thus, the MTF deterioration is of the order of few %, indicating a good thermal stability of the system.

2.10 Stray-light analysis

In order to estimate and minimize the stray-light impact on performance, we have conducted a series of preliminary computer simulations based on ray-tracing. The goals of the simulations were: (1) to determine the mean stray-light irradiance on the detector expected during the mapping of Ganymede's surface (2) to evaluate the contribution of different physical parameters (mirror micro-roughness, particulate contamination (PAC) and scattering from mechanical components) (3) to identify critical light paths and optimize the baffle design.

2.10.1 Baffle design

During the optimization process, a trade-off between the camera dimensions, performance and capability to reject first-order stray-light has been carried out. In particular, via an internal baffling system, the chosen optical configuration can be made robust for stray light rejection. The solid angle through which the external baffle will see M3 has been minimized and it is possible to completely shield the filters and the detector from light scattered by M1. The baseline baffling configuration adopted for JANUS is visible in figure 2.9: it is composed of an external cylindrical baffle, with vanes and three internal baffles (one for each mirror) with conical shape. The baffles length and shape are such as not to vignette the beam, and the depth and position of the vanes in the external baffle have been optimized in order to block first order scattering from the baffle to the primary mirror (figure 2.10). Also light scattered by the edge thickness of the vanes can contribute to SL. For this reason, the number of vanes has been reduced as much as possible during the optimization. The maximum angle at which M1 can be directly illuminated by an external source is $\theta \approx 15°$. The detector is enclosed in a dedicated housing and the whole telescope is protected by an external cover.

2.10.2 Simulation approach

Since the stray light signal depends obviously on the observing conditions (i.e. position and power of light sources), a commonly adopted method for the characterization of the stray light performance of an instrument is to calculate its Point Source Transmittance (PST). PST is defined as the amount of stray light incident on the focal plane divided by the amount of light

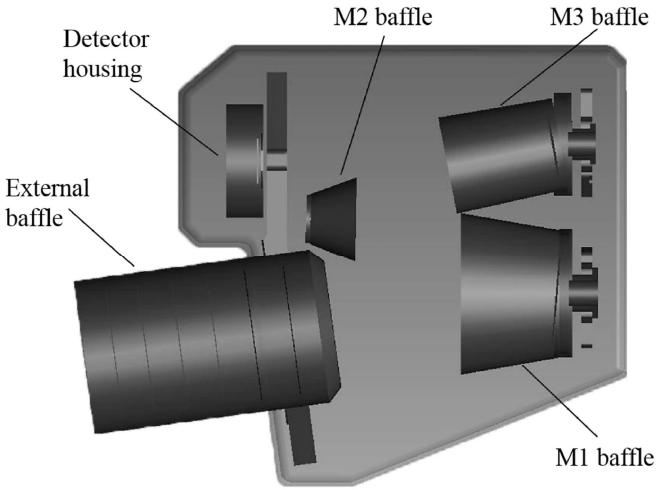

Figure 2.9: Scheme of the baffling system of JANUS

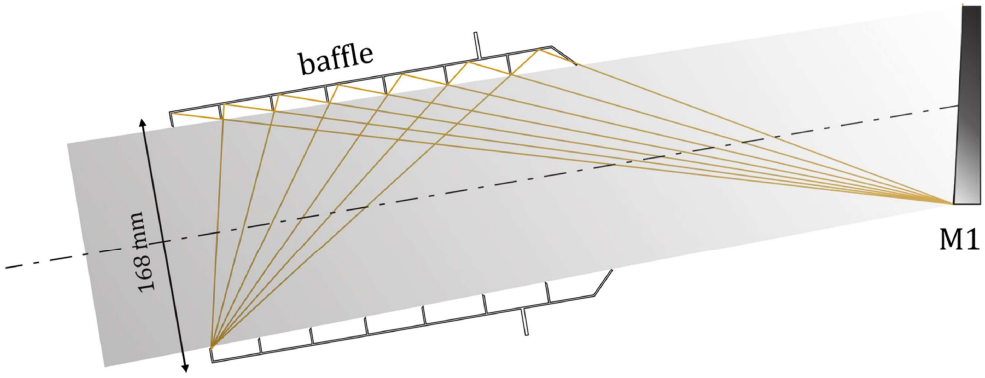

Figure 2.10: Optimization of the vane depth and position to block first-order scattering from the external baffle to the primary mirror.

incident on the entrance aperture of the system [3]:

$$PST = \frac{E_{SL}}{E_{inc}} \tag{2.7}$$

where E_{SL} is the irradiance on the focal plane due to stray light, and E_{inc} is the irradiance from a point source at infinity incident on a plane normal to the incident beam and placed at the entrance aperture of the instrument. The PST can be used to calculate the irradiance on the focal plane due to any distribution of sources just by summing up the contribution of stray light of each point source or integrating the PST over the projected solid angle of any extended source. The method adopted in our simulations is to calculate the PST for a set of entrance angles via ray-tracing techniques and to then use this information to calculate - by numerical integration - the stray light irradiance on the detector expected when observing the surface of Ganymede from 500 km of altitude. The simulated observational scenario is the one depicted in figure 2.11: the Sun is behind JANUS and completely illuminates Ganymede; JANUS is performing a nadir pointing on the surface from an altitude of 500 km (closest

approach), and receives light from the whole visible portion of Ganymede up to an angle θ_{lim} from the pointing direction. The choice of the observational scenario is driven by the

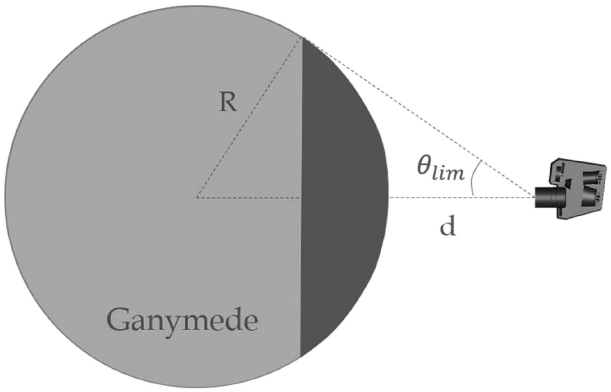

Figure 2.11: Scheme of the observing configuration between JANUS and Ganymede. R is the radius of the satellite, d is the distance between the telescope and the surface and θ_{lim} is the maximum angle from which light coming from Ganymede enters the telescope.

following: (1) the mapping of Ganymede is one of the primary targets of the mission, (2) the proximity to the surface and the correspondingly high solid angle subtended by Ganymede make it a "worst case" scenario for stray-light, (3) the geometry is easy to model.

2.10.3 Theoretical model and assumptions

To calculate the stray-light irradiance generated by an extended source like the surface of Ganymede, let's consider the radiative transfer between an infinitesimal surface area dA_{Gan} and an infinitesimal collecting surface dA_c:

$$d^2F_{s,c}(\theta,\phi) = \frac{L_s(\theta,\phi)dA_c\ cos(\theta_c)dA_s\ cos(\theta_s)}{d^2} \tag{2.8}$$

where θ_s, θ_c and d are defined as in figure 1.4. d^2F represents the infinitesimal flux coming from dA_s and impinging on dA_c. L_s is variable across the surface of the satellite because it depends on the physical characteristics and features of the surface itself. There are different laws to model scattering from the surface of a planet (some examples are provided in [17]). For our simulations, we assumed the satellite to emit like a Lambertian sphere. With this assumption, the source radiance can be expressed as:

$$L_s\,(\theta,\phi) = L \tag{2.9}$$

If we consider the following relation:

$$dA_s \cdot cos(\theta_s) = d\Omega(\theta,\phi) \cdot d^2, \tag{2.10}$$

the infinitesimal flux can be rewritten as:

$$d^2F_{s,c}(\theta,\phi) = L_s(\theta,\phi)dA_c\ cos(\theta_c)d\Omega(\theta,\phi) \tag{2.11}$$

which, integrating over the whole entrance aperture of JANUS becomes:

$$dF_{s,c}(\theta,\phi) = L_s(\theta,\phi)A_c\ cos(\theta_c)d\Omega(\theta,\phi) \tag{2.12}$$

The flux on the entrance aperture is related to the stray-light flux on the detector by the PST:

$$dF_{SL,d}(\theta,\phi) = A_d\frac{dF_{s,c}(\theta,\phi)}{A_p\ cos(\theta_c)}PST(\theta,\phi) \tag{2.13}$$

where θ is the radial angle and ϕ is the azimuthal angle (see figure 2.12). Generally, the PST is strongly dependent on θ and less dependent on ϕ. In a system rotationally symmetric around the optical axis, there would be no dependence on ϕ. Substituting equation 2.12 in equation 2.13, we obtain:

$$dF_{SL,d}(\theta,\phi) = A_d \cdot L_s \cdot PST(\theta,\phi) \cdot d\Omega(\theta,\phi). \tag{2.14}$$

Integrating this last relation over the solid angle subtended by the source gives the total stray-light flux on the detector:

$$dF_{SL} = A_d \cdot L_s \int\int PST(\theta,\phi)d\theta\ d\Omega(\theta,\phi) \tag{2.15}$$

This last equation shows that the stray-light flux on the detector is given by the product of the detector area, the source radiance and the integral of the PST over the solid angle subtended by Ganymede as seen from JANUS. We recall that the PST already includes the throughput of the optical system. The equation is further simplified if we consider the ratio between the total stray-light flux and the flux of the scientific image on the detector. The flux of the image depends on the field of view of the telescope and is given by:

$$dF_{Sci,d} = A_c \cdot L_s \cdot \tau_{eff} \cdot FoV_x \cdot FoV_y \tag{2.16}$$

where τ_{eff} is the transmission efficiency of the instrument. Since the product $A_c \cdot FoV_x \cdot FoV_y$ is the throughput, which is conserved from the entrance aperture to the detector, we can express the scientific flux as a function of the detector area:

$$dF_{Sci,d} = A_d \cdot L_s \cdot \tau_{eff} \cdot \frac{\pi}{4F\#^2} \tag{2.17}$$

where $F|\#$ is the focal ratio of the telescope. Taking the ratio between equations 2.15 and 2.17 we get the following, very simple relation:

$$\frac{\Phi_{SL}}{\Phi_{Sci}} = \frac{4}{\pi}\frac{F_\#^2}{\tau_{eff}}int_0^{2\pi}\int_0^{\theta_{lim}} PST(\theta,\phi)sin(\theta)d\theta d\phi \tag{2.18}$$

The equation tell us that, when observing a sphere (Ganymede) reflecting/scattering like a lambertian surface, the ratio between the stray light flux and the image flux on the detector is given by the product of two factors:

1. a factor dependent on the throughput of the optical system (related to the $F\#$):
2. the integral of the PST over the solid angle subtended by the sphere.

Moreover, the ratio is independent of the total power emitted by the sphere.

2.10.4 PST calculation

To calculate the PST, we used ray-tracing simulations with Zemax, performed on a non-sequential model. We set up a simplified model of the telescope, including all the main opto-mechanical components. To simulate the scattering properties of each surface, we considered three different phenomena of scattering:

1. scattering from micro-roughness of the optical surfaces
2. scattering from PArticulate Contamination (PAC) of the optical surfaces
3. scattering from mechanical surfaces

The rays were generated with a collimated source of unit irradiance aimed at the entrance aperture of JANUS (as shown in figure 2.12) that simulates the light coming from a point source at infinity that enters the instrument and gets scattered, eventually reaching the detector plane. Since the source has unit irradiance, the value of the PST (in the direction of the source) is simply given by the power recorded by the detector divided by the area of the detector itself.
The simulations are made with monochromatic light at $\lambda = 400\ nm$, corresponding to the bluest part of the observing wave-band of JANUS. Since the total scattering due to micro-roughness has, approximately, a λ^{-2} dependence on the wavelength ([3]), our simulation conditions correspond to a worst-case scenario for micro-roughness. Particulate contamination and scattering from mechanical surfaces are also wavelength dependent, but the variation is not as strong as in the case of micro-roughness. The PST is calculated by running several

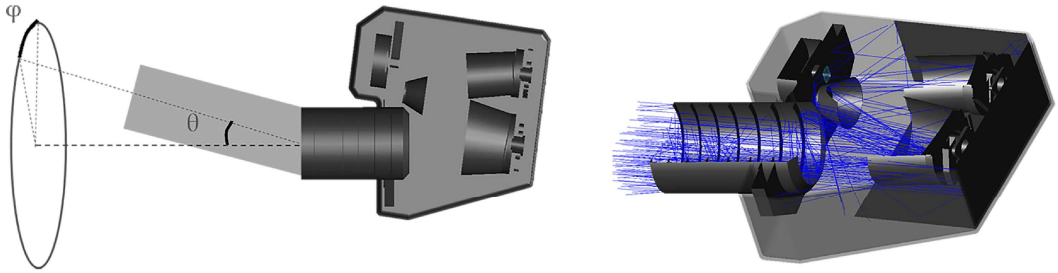

Figure 2.12: Left: collimated beam of light entering JANUS with the definition of the off-axis angle (θ) and the azimuth angle (ϕ). Right: Zemax model of the telescope with a few rays traced through the system.

simulations with different entrance angles θ and ϕ (see figure 2.12) for the source. In this way, we sample the PST at different entrance angles and we estimate the real PST interpolating between the data-points. To sample the (θ, ϕ) parameters space we chose a uniform spacing in ϕ (with a $\Delta\phi = 30\ deg$) and a non-uniform spacing in θ, with a more dense sampling inside or near the field of view. The total number of directions for which we calculated the PST is 195.

2.10.5 scattering models

Each scattering phenomena (roughness, PAC, etc...) is modelled with a specific *Bidirectional Scattering Distribution Function* (BSDF) which gives the radiance of the scattering surface, normalized by the irradiance incident on the surface:

$$BSDF(\theta_i, \phi_i, \theta_s, \phi_s) = \frac{dL(\theta_i, \phi_i, \theta_s, \phi_s)}{dE(\theta_i, \phi_i)} \tag{2.19}$$

where θ_i and ϕ_i are the elevation and azimuth angles of the incident ray, θ_s and ϕ_s are the elevation and azimuth angles of the scattered ray respectively, dL is the differential radiance of the scattering surface, and dE is the differential incident irradiance.
The BSDF generated by roughness or contamination of optical surfaces is generally well described by the 3-parameter *Harvey model* ([3]):

$$BSDF(|sin(\theta_s) - sin(\theta_i)|) = b_0 \left[1 + \left(\frac{|sin(\theta_s) - sin(\theta_i)|}{l}\right)^2\right]^{s/2} \tag{2.20}$$

Where b_0, l and s are the three free-parameters and θ_i and θ_s are respectively the incident and scattering angles with respect to the surface normal.
The *ABg model* is another common model used to describe BSDF. It is very similar to the Harvey model and it is described by the law:

$$BSDF = \frac{A}{B + |sin(\theta_s) - sin(\theta_i)|^g} \tag{2.21}$$

The three coefficients of the ABg model can be computed from the Harvey model as:

$$\begin{aligned} B =& l^{-s} \\ g =& -s \\ A =& b_0 B \end{aligned} \tag{2.22}$$

Micro-roughness

For the micro-roughness of optical surfaces, we used a value of 20 Å rms and we modelled it with an ABg profile. The resulting Total Integrated Scatter (TIS), i.e. the integral of the BSDF over the full solid angle of scattering, depends on the index of refraction and thus, on the material of the optical element:

$$TIS = \left(2\pi\Delta n \frac{\sigma_\lambda}{\lambda}\right)^2 \tag{2.23}$$

where σ_λ is the roughness rms of the surface and $\Delta n = 2$ for mirrors. The ABg parameters and the resulting TIS are summarized in table 2.7.

	ABg Model			Harvey Model			TIS (ppm)
	A	B	g	l	s	b_0	
mirrors	2.11654E-04	2.51189E-04	1.8	0.01	-1.8	0.84260	3950
filter	1.16886E-05	2.51189E-04	1.8	0.01	-1.8	0.04457	218
window	3.27313E-05	2.51189E-04	1.8	0.01	-1.8	0.12490	611

Table 2.7: scattering parameters used in the ABg model, and corresponding parameters of the Harvey model

Scattering from mechanics

For the purposes of SL analysis, we used either 100% absorbing mechanical components or partially scattering components. We considered partially scattering components to be black, coated with Aeroglaze z306 [18]. The BSDF of Aeroglaze z306 has been taken from the scattering library of the software ASAP and modelled in Zemax with a "BSDF table" listing the BSDF for different angles of incidence and angles of scatter. The values were multiplied by a factor of 1.3× as a safety margin. The total integrated scatter resulting from the tabulated data as a function of the incident angle is shown in figure 2.13 (left). For angles of incidence

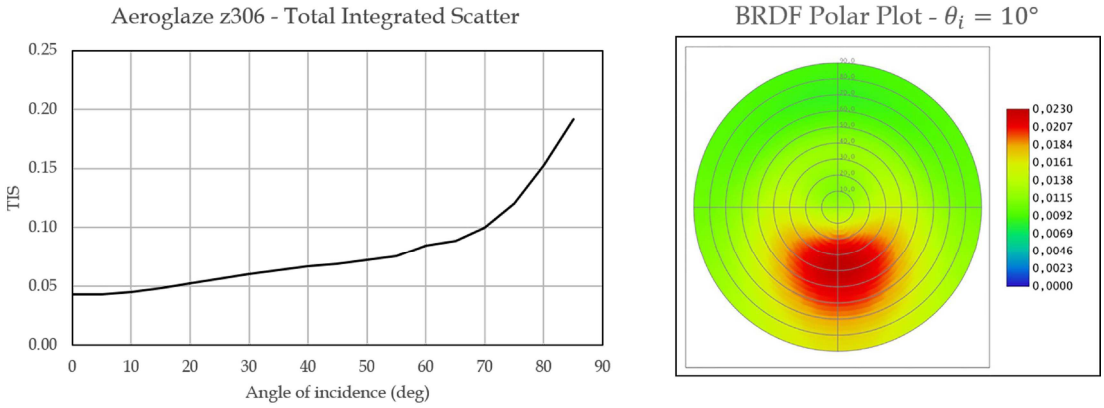

Figure 2.13: Left: Aeroglaze z306 total integrated scatter as a function of the angle of incidence. Values were taken from the ASAP scatter library and multiplied by 1.3×. Right: BSDF polar plot for an angle of incidence of 10 deg.

higher than 80 deg, the total integrated scatter is higher than 15%.

Particulate contamination

Particulate contamination intervenes on optics, changing the BSDF and the TIS of the surface itself. While it is possible to estimate this effect using Mie scattering theory, this kind of calculation is very time intensive to be done and difficult to be used in a ray-tracing simulation. Moreover, Zemax does not support it directly. For a first estimate, we have chosen to model the particulate contamination using the sum of two Harvey profiles whose total TIS=382ppm (figure 2.14). The parameters of the Harvey profiles were provided by BRO (Breault Research Organization) during the "Stray light analysis tutorial" and they are

based on a fit to a scattering model based on Mie scattering theory. The two profiles are characterized by the parameters reported in table 2.8 and refer to a PAC=500ppm (i.e. the percentage of area covered by particles is equal to 500ppm).

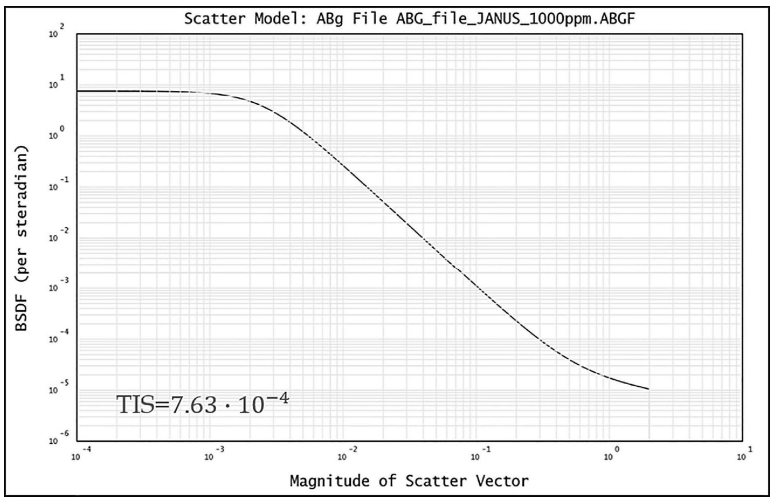

Figure 2.14: BSDF of the double Harvey profile multiplied by a factor of 2.

	ABg Model			Harvey Model			TIS (ppm)
	A	B	g	l	s	b_0	
Profile 1	2.16192E-06	5.68926E-07	2.4	2.5E-03	-2.4	3.8	357
Profile 2	9.71187E-06	4.85593E-01	0.6	0.3	-0.6	2.0E-05	25

Table 2.8: Harvey scattering parameters used in the stray-light analysis and corresponding ABg parameters. The final profile is the sum of profile 1 and profile 2.

Molecular contamination

Molecular contamination refers to the volatiles that outgas from a material and deposit on the sensor and optics. This contamination has, as a main effect, a reduction of throughput. Molecular contamination could also increase the BSDF of the optics and degrade the stray-light performance of the system [3]. However, this effect is poorly understood and we did not take it into account in the simulations.

2.10.6 Coatings

The coating of a surface determines its reflectance or transmittance properties as a function of wavelength and angle of incidence. For the purposes of our simulations, we used "ideal" coatings with reflectance independent of the angle of incidence. Moreover, we did not consider any wavelength dependence, since the simulations are performed at a single wavelength $\lambda = 400\ nm$. The coatings were applied to all the optical elements, including the detector. The values used for the reflectance and transmittance depend on the kind of simulation performed (micro-roughness, PAC or ghost analysis) and will be provided in the following sections.

2.10.7 Telescope model

The stray-light analysis has been performed using the non-sequential capabilities of Zemax. The non-sequential model of the telescope is based on the opto-mechanical design presented at the ICR instrument review [19], dedicated to the definition of the system requirements. The mechanical components, such as the filter wheel, baffles, or the detector housing, have been taken from the mechanical design and their geometry has been simplified in order to optimize the time required for the simulations. Obviously, this change in the geometry could have an impact on the final stray-light budget, but we expect the model to be accurate enough for this preliminary analysis.
The non-sequential design appears in figure 2.15 and it is characterized by the following components:

- **Cover**: the outer box which encloses the camera
- **Optical bench**: the plane where the box and the support structure for the optics are connected
- **External baffle**: the entrance baffle of JANUS. It is a cylinder with a tapered section on the M1 side and internal vanes to block first-order stray-light from the baffle to the primary mirror
- **M1 baffle**: the baffle around the primary mirror. It has the shape of a truncated cone with an aperture angle such as not to vignette the light
- **M1**: the optical surface of the primary mirror
- **M2 baffle**: the baffle around the secondary mirror. It has the shape of a truncated cone with an aperture angle to not to vignette the light
- **M2**: the optical surface of the secondary mirror
- **M3 baffle**: the baffle around the tertiary mirror. It has the shape of a truncated cone with an aperture angle to not vignette the light
- **M3**: the optical surface of the tertiary mirror
- **M1-M3 mount**: the mounting structure of the primary and tertiary mirrors
- **M2 mount**: the mounting structure of the secondary mirror
- **Main plate**: the structure supporting the mounting for M2. It has the shape of a slightly bent plate and divides the volume inside the box in two parts: one containing the mirrors and another one containing the detector. The two sections communicate only through the filter aperture.
- **Tube**: the cylindrical structure connecting the M1-M3 mount to the main plate.
- **Filter**: the glass plate used as substrate for the filter. It is made of fused silica.
- **Window**: the flat window protecting the detector from radiation and contamination. The substrate material is Suprasil.

- **Detector**: the surface of the detector. It is used to record the rays of the SL simulation. The linear size of the pixels is 10 times bigger than the real one to reduce statistical noise due to the finite number of rays traced. An AR coating as been applied to simulate ghost-reflected light.

- **Detector cover**: an absorbing box enclosing the detector in a way such that it can communicate to the external environment only through the window.

In addition to these components, some surfaces have been added to simulate scattering more efficiently. For example, some surfaces have been applied to the JANUS cover to properly point scattered rays in specific critical directions with the purpose to reduce the number of scattered rays and speed up the simulation. This technique makes use of the "scatter to" function of Zemax which allows scattered rays only in specific directions. The energy of the rays is normalized accordingly to compensate for the preferential scatter direction.

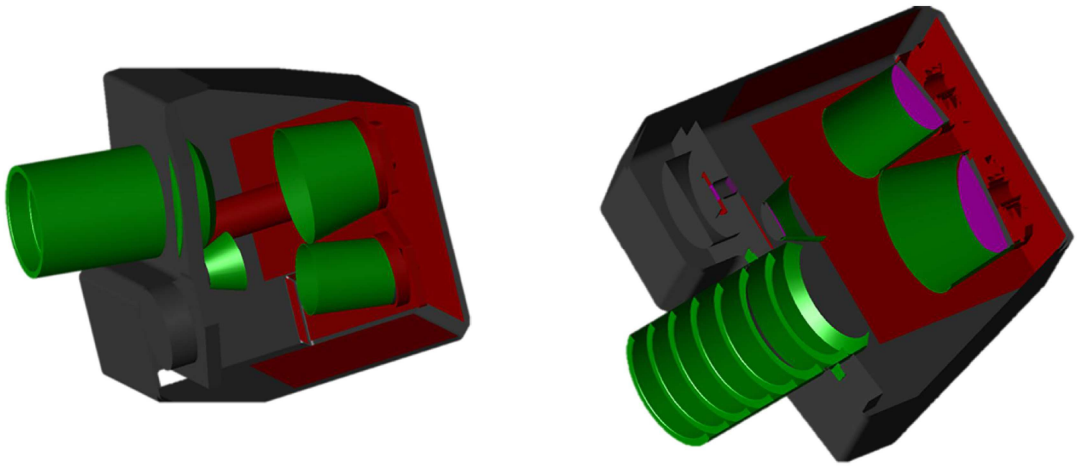

Figure 2.15: Two different views of the non-sequential model of JANUS used for the stray-light analysis.

2.10.8 Input parameters

To simulate the relative importance of the various stray-light sources, we performed three different types of analysis: the first calculates the PST from the micro-roughness of optical elements and scattering from mechanics; the second determines the PST from particulate contamination, and the third evaluates ghost reflections from filters, window and detector. The input parameters used for every simulation are reported in tables 2.9 - 2.10 - 2.11. For the scattering simulations (roughness and PAC), we assumed 100% throughput of optical elements. This corresponds to a "worst case" condition, since all the scattered stray-light is transmitted to the detector. For the ghost simulation, on the other hand, a partial reflectivity of refractive elements was necessary to produce ghost reflections. The simulation wavelength is $\lambda = 400\ nm$ for all simulations.

Micro-roughness simulation	
Parameter	**Value**
Mirror reflectance	100%
Filter & window transmittance	100%
Detector reflectance	0%
Detector QE	100%
Mirror micro-roughness	2 nm rms
Filter & window micro-roughness	2 nm rms
Mechanical el. BSDF profile	Aeroglaze z306 (1.3x)
Particulate contamination	0 ppm
Molecular contamination	not simulated

Table 2.9: parameters used in the roughness simulation

PAC simulation	
Parameter	**Value**
Mirror reflectance	100%
Filter & window transmittance	100%
Detector reflectance	0%
Detector QE	100%
Mirror micro-roughness	none
Filter & window micro-roughness	none
Mechanical el. BSDF profile	Aeroglaze z306 (1.3x)
Particulate contamination	Harvey profiles: 500-1000 ppm
Molecular contamination	not simulated

Table 2.10: parameters used in the contamination simulation

2.10.9 Results

Micro-roughness simulation

The PST was calculated at different entrance angles ($0\ deg < \theta < 80\ deg$ and $0\ deg < \phi < 360\ deg$) with a denser sampling within the FoV of JANUS and just outside it. The results are reported in figure 2.16, in which the different colors represent the PST at different azimuth angles between 0 and 360 deg. Inside the field of view ($\theta < 0.85\ deg$) the PST value is larger, and drops rapidly outside the field of view, suggesting that most of the stray light will be generated within the field. Anyway, since the solid angle inside the field of view is much smaller than the total solid angle subtended by Ganymede, also the light coming from outside the field of view can contribute significantly to the total stray light budget. To see the effective contribution as a function of the entrance angle, it is necessary to calculate the integral of equation 2.18. Figure 2.17 shows the cumulative integral of the PST assuming it to be constant at different azimuth angles. In practice, we are just integrating along θ, while the integration along ϕ yields a factor 2π. Again, the colors refer to the PST profile of different azimuth angles. The major contribution to stray light comes from angles between 0.5 and 10 deg. Indeed, for $\theta < 10$ deg the primary mirror is still directly illuminated from outside and

Ghost simulation	
Parameter	**Value**
Mirror reflectance	100%
Filter & window transmittance	99%
Detector reflectance	10%
Detector QE	90%
Mirror micro-roughness	none
Filter & window micro-roughness	none
Mechanical el. BSDF profile	none
Particulate contamination	none
Molecular contamination	not simulated

Table 2.11: parameters used in the ghost simulation

reflects/scatters light inside the telescope, dominating the contribution to the stray-light flux on the detector. A nice way to see the relative contribution of the elements to the stray-

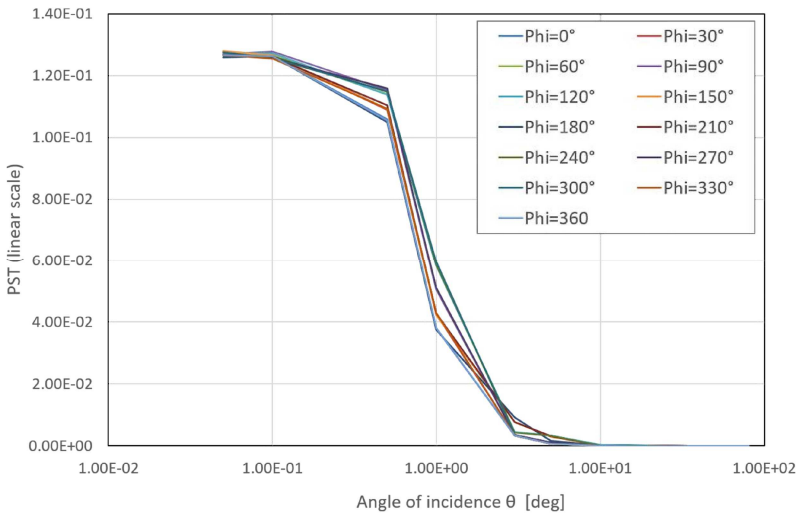

Figure 2.16: PST due to micro-roughness and scattering from mechanics as a function of the entrance angle θ for different azimuthal directions (ϕ).

light at a given entrance angle is to track the surfaces at which each ray has been scattered. Of course, a single ray can be scattered more than once, producing long combinations of scattering paths that become complicated to visualize. Anyway, since the ray loses energy at every scattering process, the multiple-scattered rays will have less energy than the single-scattered ones and their energy contribution will be smaller (although not negligible). This argument make it reasonable to consider different subgroups, each containing rays that have been scattered at least once by a given element. In this way, multiple-scattered rays will be part of many subgroups at the same time but, in general, they will have less energy because of the multiple scattering. So, for example, considering all the rays that have been scattered at least once by the primary mirror (for a given entrance angle) is a good estimation of the contribution of the primary mirror to stray-light (for that entrance angle). Doing this

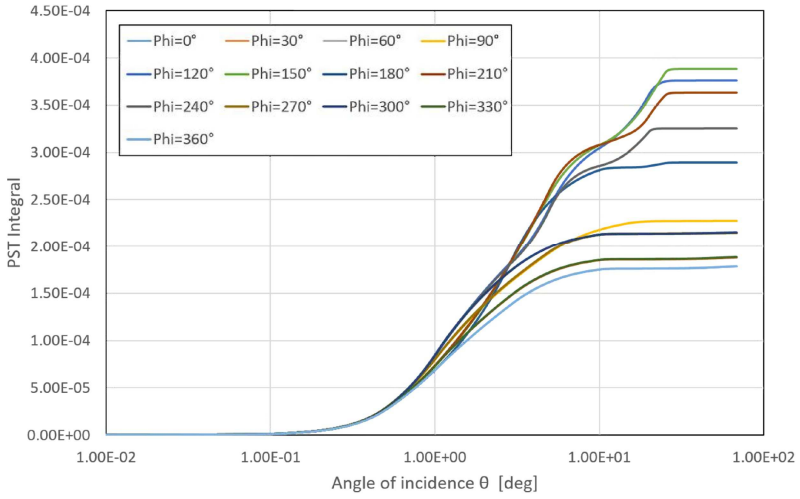

Figure 2.17: Cumulative integral of the PST due to micro-roughness and scattering from mechanics.

operation for every scattering element we get the results shown in figure 2.18. For reasons of clarity, only the main elements have been plotted in the figure. Inside the field of view the major contributors are the optical elements: the three mirrors, the filter and the window. Between 5 and 15 deg, most of the scattered light comes from the primary mirror which is directly illuminated from the outside. Finally, for angles greater than 20 deg, the major contributor is the external baffle.

Contamination simulation

The PST for the contamination simulation was calculated only along the diagonal of the detector, so the elevation angle θ is again in the range $0 - 80$ deg, but the azimuthal angle is fixed at $\phi \approx 53$ deg. To have an idea of the relative contribution of scattering from mechanics and from PAC, we performed two simulations with PAC=500ppm and PAC=1000ppm, respectively. The two levels of contamination have been simulated just by scaling the BSDF by a factor of two. The obtained PST are represented in figure 2.19. The PST relative to PAC=1000ppm is approximately a factor of two higher than that of PAC=500ppm, meaning that most of the scattered light comes from particulate contamination rather than scatter from mechanics. Also, for contamination the PST is higher within the field of view and drops rapidly outside the field. The cumulative integral of the PST, which gives the amount of stray-light when observing Ganymede, is shown in figure 2.20. It grows rapidly between 0 and 2 deg. In this range of entrance angles, the major contribution is given by the window and the filter, meaning that particular care should be taken to prevent contamination of these surfaces.

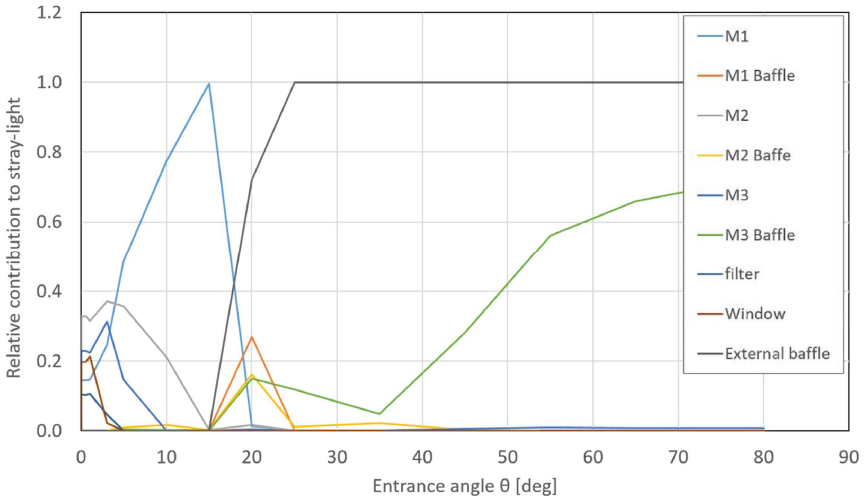

Figure 2.18: Relative contribution to stray-light of the scattering elements as a function of θ. For clarity, only some of the elements are plotted.

Ghost simulation

Generally, ghost reflections are produced only by sources within (or just outside) the FoV. For this reason, the ghost simulation was performed only for an on-axis point source and then the results have been extended to the whole field. In JANUS, ghosts are generated by reflection from the two surfaces of the filter and of the window and by the detector. The ghost pattern produced on the detector from an on-axis source is shown in figure 2.21 (left). It is a superposition of circles produced by double reflection (or an even number of reflections) from refracting surfaces. The irradiance of each circle is proportional to the reflectivity of the surfaces in which it was ghost-reflected and inversely proportional to its area. Since there are only flat refracting surfaces, the size of the circles is proportional to the distance between the ghosting surfaces. Figure 2.21 also shows a horizontal strip of light, probably generated by total internal reflection from the lateral faces of the window and filter, but its irradiance is negligible, being about eight orders of magnitude smaller than the peak irradiance. The total ghost power recorded by the detector is 0.28% of the power of the input source.

The contribution of each refractive element to the total ghost power cannot be evaluated in a unique way since ghosts, like scattering, can be produced by multiple reflections from different elements. Just to have an idea of the relative contribution of each element we report in figure 2.21 (right) the relative power coming from rays that have been ghost-reflected at least once from a given element before reaching the detector. As expected, the major contribution is due to the window, because of its small distance from the detector. Anyway, we stress the fact that the powers given in figure 2.21 are cross-correlated and, for example, increasing the reflectivity of the detector increases the power ghosted from window and filter.

2.10.10 Straylight during GCO-500

When observing Ganymede from an altitude of 500km (GCO-500), we can estimate the ratio between stray-light signal and scientific signal, once the PST of the instrument is known. Approximating Ganymede to be a uniform, Lambertian source, the ratio is given by equation

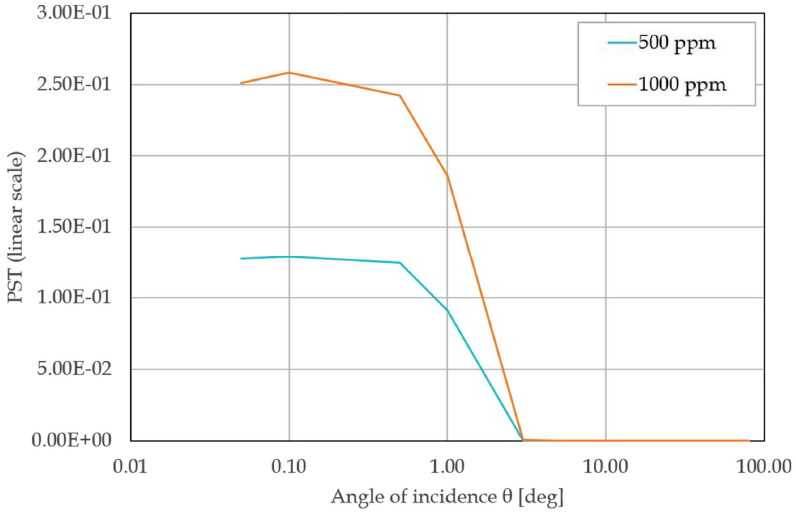

Figure 2.19: PST due to particulate contamination and scattering from mechanics as a function of the entrance angle θ for different levels of contamination.

2.18, where the integral over θ is calculated up to the limit angle $\theta_{lim} = 68$ deg. Using the PST calculated by ray-tracing simulations, the stray-light signal generated by micro-roughness is of the order of 0.5% of the scientific signal; that generated by PAC=500ppm is of the order of 0.3%. Concerning the signal generated by ghosts, when observing a uniform, extended object that fills the entire frame, we can imagine, as a first approximation, that the same ghost pattern is produced for every point within the field, generating a uniform distribution of ghost-reflected light. The ratio between the ghost signal and the scientific signal is approximately equal to that of an on-axis point source and thus, it is equal to $\approx 0.3\%$. Adding up all three contribution we get that the total stray-light signal is of the order of 1% of the scientific signal when observing Ganymede from 500km of altitude and with the Sun on the back. Of course this is one of the worst observational scenarios given the huge solid angle subtended by Ganymede and the short wavelength used for the simulations.

2.10.11 Baffling improvement

Looking at the PST integral of micro-roughness (figure 2.17), there is clearly a non-uniform behavior with respect to the azimuth angle with changes of the PST integral up to a factor of 2-3 among the different azimuthal angles. Of course, it is possible to take into account this variation just by calculating the integral in the 2-D parameter space, but we asked ourselves if it is possible to optimize the baffling design and obtain a more uniform behavior of the system with respect to stray-light.
A more detailed analysis showed that most of the difference was arising from rays striking the cover from inside and reaching the detector directly or via multiple scattering events. A possible way to partially block these rays is to split the box in two parts: one containing the detector and the tertiary mirror, and the other containing the primary mirror and the external baffle, so that rays scattered by the cover cannot reach the detector by first order scattering. A possible implementation of this solution appears in figure 2.22, where the internal baffles are replaced by a curtain (red in figure) with a central hole to let the in-field light pass

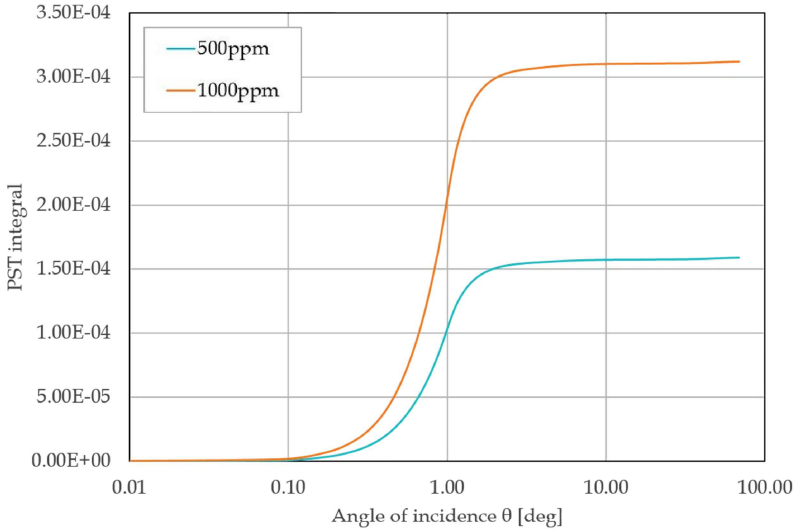

Figure 2.20: Cumulative integral of the PST due to particulate contamination and scattering from mechanics.

through without vignetting. We computed the cumulative integral of the PST also for this configuration (figure 2.22 - right) and, as expected, the dependence on the azimuth angle is greatly reduced.

2.11 Design evolution

In September 2015, a new optical configuration was proposed by Leonardo-Finmeccanica, the prime contractor selected for the production of the JANUS Telescope module and the integration of the other sub-systems (focal plane assembly, proximity electronic unit, data processing unit, etc...). The main driver for the design modification was the reduction in mass to cope with the requirements from ESA: 8.74 kg for the telescope module and 12.40 kg for the Optical Head unit, accounting for a 20% contingency.
The new optical design is based on a Ritchey-Chrétien (RC) telescope with a three-lens field corrector (figure 2.23). Leonardo-Finmeccanica already had experience with this configuration, since it is the same used for the High Resolution Imaging Channel of SIMBIO-SYS in the Bepi Colombo mission [20] and similar to the one used in CHEOPS (CHaracterising ExOPlanet Satellite) [21]. The new configuration is characterized by the same first-order properties of the TMA (focal length, field of view, waveband, etc...). It is an on-axis system with central obstruction, but the entrance pupil diameter is such that the collecting surface is equal to that of the TMA. Because of the obstruction, the nominal MTF is slightly lower than the TMA configuration, with a value $MTF > 58\%$ on the entire field. Nevertheless, the strongest limit on the MTF will be given by the detector intrinsic MTF (generated by the spatial filtering of the finite size detector pixel), which is of the order of 15%. The system is more compact than the three-mirror solution, being approximately half the size of the TMA in both length and height. The proposed baffling configuration is composed of one external baffle with vanes plus one internal conical baffle on the primary mirror obstruction that acts also as a mounting for the three-lens corrector.

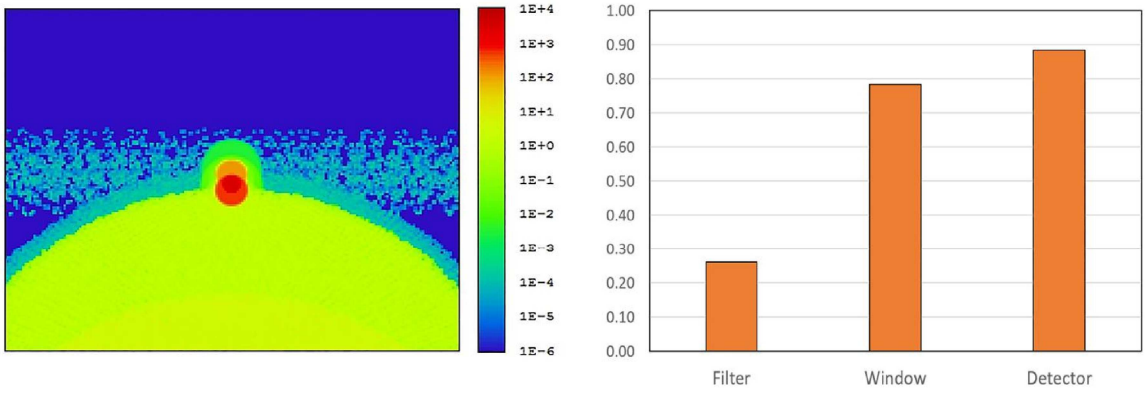

Figure 2.21: Left: ghost pattern produced by an on-axis source. Right: relative contribution to ghost power.

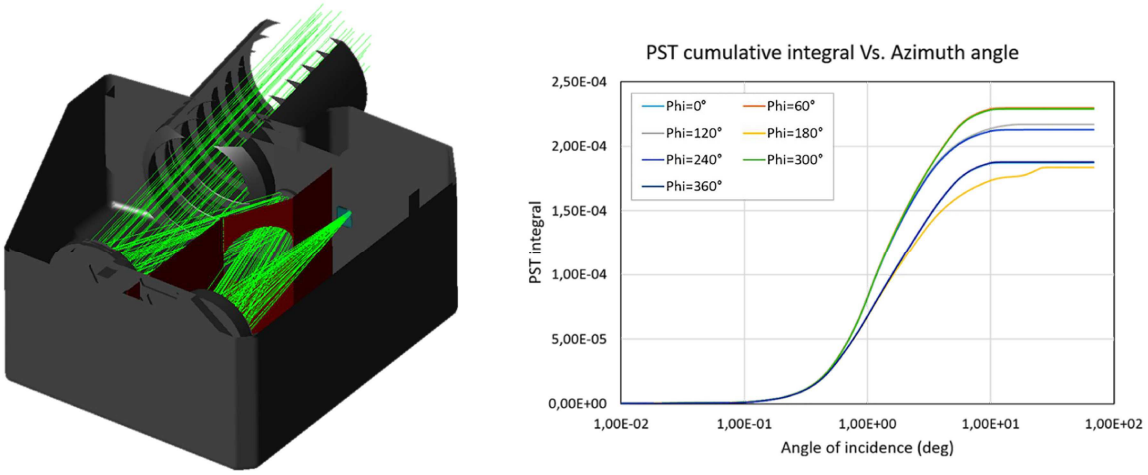

Figure 2.22: Left: layout of the optimized internal baffling configuration. Right: micro-roughness PST integral for the new baffling configuration.

The solution proposed by Leonardo has been evaluated positively, the only concern being the stray-light performance of the system. In fact, the on-axis design is more prone to stray-light and the baffling is more critical. For this reason, and given the experience gained from the stray-light analysis of the TMA design, we were asked to perform a preliminary stray-light analysis also on the RC configuration.

2.11.1 RC stray-light analysis

In order to assess the stray-light performance of the RC configuration, we performed a preliminary analysis based on the same method and assumptions used for the TMA. The purpose of this preliminary simulation is to compare the stray light performance of the Ritchey-Chrétien and the Three-Mirror design. For this reason, we used parameters as close as possible to the ones already used in the TMA simulations.

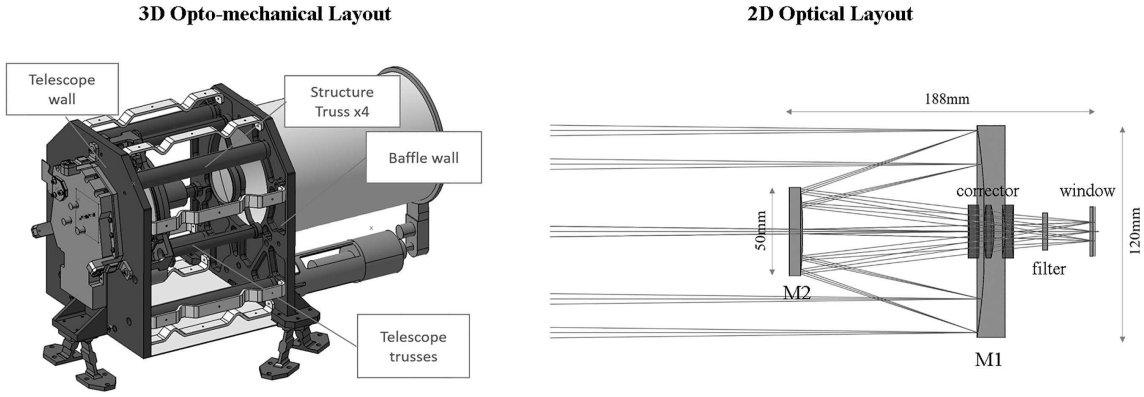

Figure 2.23: Left: Ritchey-Chrétien 3D opto-mechanical layout. Right: 2D optical layout.

We performed two different kind of simulations: one for the scattering, taking into account micro-roughness and particulate contamination, and the other for ghost reflections. In the case of the scattering simulation, the stray light performance has been evaluated by calculating, with ray-tracing, the Point Source Transmittance (PST) of the telescope for different entrance angles. In the case of the ghost simulation, the performance has been evaluated by calculating the irradiance and total power of ghost images

Non-sequential model

Based on the opto-mechanical models provided by Leonardo-Finmeccanica, we developed a non-sequential Zemax model of the telescope. The external baffle has been optimized both concerning length and vane position. The length has been adjusted to avoid direct illumination of the detector by external sources. The vane position and depth has been optimized to reject first-order stray-light from the baffle to the primary mirror and the detector (figure 2.24). Also the internal baffle on the primary mirror has been adjusted to avoid vignetting of the FoV, but still to prevent direct illumination of the detector by external sources. The final

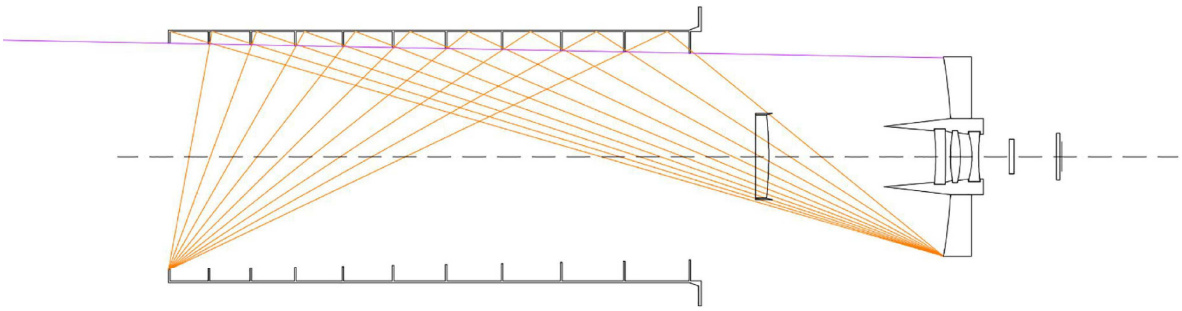

Figure 2.24: Rays traced for the optimization of the vanes position

model used for the simulations includes the following elements:

- **Cover**: the outer box enclosing the camera
- **External baffle**: cylindrical shape with vanes

- **Internal baffle**: conical shape with internal mounting structure for the three-lens corrector
- **M1**: optical surface of the primary mirror
- **M1 mount**: mounting structure of the primary mirror
- **M2**: optical surface of the secondary mirror
- **M2 mount**: mounting structure of the secondary mirror
- **M2 spiders**: three radial spiders to hold the secondary mirror
- **Baffle wall**: the structure supporting the external baffle and constituting the front part of the cover
- **Telescope wall**: the structure supporting the primary mirror and the focal plane assembly
- **Filter**: the glass plate used as substrate for the filter. It is made of fused silica
- **Window**: the flat window protecting the detector from radiation and contamination. The substrate material is fused silica
- **Corrector**: the three lenses providing field correction (fused silica)
- **Detector**: the surface of the detector. It is used to record the rays of the SL simulation.
- **Detector cover**: an absorbing box enclosing the detector in a way such that it can communicate to the external environment only through the window.

The internal baffle was split in different parts to optimize ray-aiming and reduce the simulation time.

Simulation parameters

The parameters used in the scattering and ghost simulations are reported in table 2.12 and 2.13 respectively. We used two different levels of particulate contamination for the mirrors and the three-lens corrector because the latter is less exposed to dust deposition on the optical surfaces.

Results

The PST has been calculated, by ray-tracing, at 16 different entrance angles between 0 deg and 80 deg. The direction of the incoming light follows the diagonal of the detector. Thus, the field of view is approximately equal to 1 deg (diagonal radial field). In table 2.14 and figure 2.25, we report the comparison between the RC and TMA point source transmittance. Note that the entrance angles used are different in the two simulations. The in-field PST is slightly bigger for the RC case, due to the increased number of optical surfaces. In the range 2-5 deg there is another deviation between the two curves. Here, the major contribution to scattering in the RC design is the internal part of the M1 baffle that is directly illuminated and visible from the detector. Finally, in the range 10-80 deg the PST is very small, but it is orders of

Scattering simulation	
Parameter	**Value**
Wavelength	400 nm
Mirror reflectance	100%
Filter & window transmittance	100%
Detector reflectance	0%
Detector QE	100%
Mirror micro-roughness	2 nm rms
Glass micro-roughness	1 nm rms
Mechanical el. BSDF profile	Aeroglaze z306 (1.3x)
Particulate contamination	500 ppm for M1, M2 300 ppm for glass
Molecular contamination	not simulated

Table 2.12: parameters used in the scattering simulation of the RC configuration

Ghost simulation	
Parameter	**Value**
Wavelength	400 nm
Mirror reflectance	100%
Filter & window transmittance	99%
Detector reflectance	10%
Detector QE	90%
Mirror micro-roughness	none
Glass micro-roughness	none
Mechanical el. BSDF profile	100% absorbing
Particulate contamination	none
Molecular contamination	not simulated

Table 2.13: parameters used in the ghost simulation of the RC configuration

magnitude bigger in the RC case with respect to the TMA. The major contribution is given by the thickness of the vanes of the external baffle that scatter directly to the detector. We use the PST to calculate the stray light expected when observing a lambertian sphere from 500 km. The ratio between the stray light flux and the scientific flux is given by equation 2.18. The PST is considered constant over the Azimuth angle. Thus, the integral over $d\phi$ gives a factor 2π. Figure 2.26 shows the cumulative integral of the PST as a function of the entrance angle for the RC and TMA cases. The integral is equal to 1.4E-3 for the RC configuration and 2.95E-4 for the TMA. As is visible from figure 2.26, most of the difference arise between 1 deg and 5 deg. In this range, the major contributor to stray light (in the RC case) is the internal face of the M1 baffle. This result suggests that particular attention should be taken for the design of this component. A possible solution to reduce stray-light is to add vanes to this baffle, keeping within the limits given by the design or partially vignetting the beam.

In figure 2.27, we show the ghost images on the detector produced by every refractive component. The images show the irradiance produced by light that has been ghosted at least

RC configuration		TMA configuration	
Entrance angle θ (deg)	**PST**	**Entrance angle θ (deg)**	**PST**
0.0	2.32E-01	0.05	1.86E-01
0.3	2.28E-01	0.1	1.81E-01
0.6	2.10E-01	0.5	1.74E-01
1.0	1.49E-01	1	1.07E-01
1.5	5.55E-02	3	3.37E-03
3.0	1.33E-01	5	1.02E-03
5.0	2.17E-03	10	6.06E-08
10.0	2.45E-04	15	1.19E-09
15.0	1.36E-04	20	3.43E-09
20.0	7.78E-05	25	4.26E-09
25.0	3.66E-05	35	1.84E-09
30.0	2.10E-05	45	1.28E-09
40.0	6.12E-06	55	7.84E-11
50.0	2.17E-06	65	3.58E-10
65.0	5.72E-06	80	2.57E-11
80.0	9.73E-09		

Table 2.14: Point Source Transmittance values calculated with the ray-tracing simulations

once by that element. The exceptions are the "total ghost irradiance" which accounts for all the light that has been ghosted at least once and the "scientific image irradiance" which accounts for the light that has not been ghosted at all. Below each image is given the peak irradiance and the total power recorded by the detector.

Most of the ghost irradiance is produced by double reflections: the first reflection sends the light back to M2 and the second reflection sends the light toward the detector. An exception to this is represented by L3, for which most of the ghosted power is generated by the path L3-M2-Detector with just one ghost reflection on the second surface of L3. This first-order path is due to a bad coupling between L3 and M2 and generates about half of the total ghosted power. A new deisgn of the corrector can easily solve this issue, and Leonardo-Finmeccanica has already fixed the problem.

The input source used in the ghost simulation is an on-axis source with unit irradiance (in $Watt/mm^2$) corresponding to a total input power of P=8087 Watt. The scientific power is 6586 Watt, due to the imperfect transmission and Q.E. of the detector. Of course, for a point source, the ghost power is distributed with a specific pattern but, if we observe a Lambertian extended source, the ghost irradiance tends to become more uniform. If we use the ratio between the total on-axis ghosted power and the scientific power to estimate the system performance, we get:

$$\frac{P_{gh}}{P_{sci}} = 1.23\% \tag{2.24}$$

As said before, about half of the power comes from the bad coupling between L3 and M2. For the new design, the ghost power should be of the order of 0.6%, although we have not yet checked this by simulation.

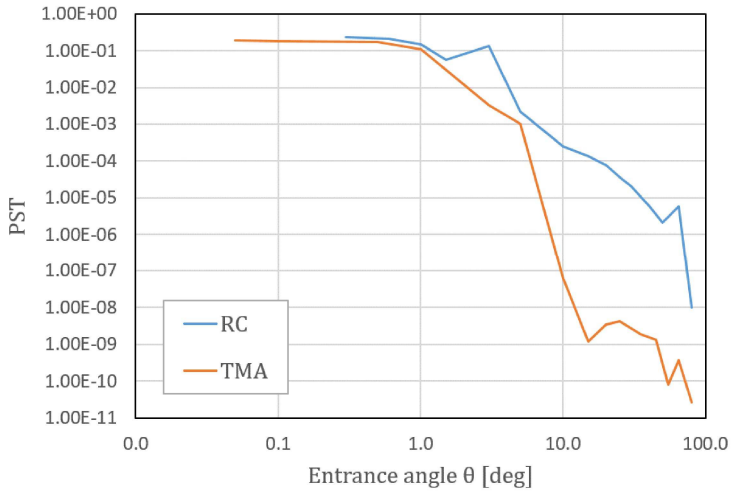

Figure 2.25: Point Source Transmittance of the RC and TMA configurations. The axes are in log scale.

Results verification: on-axis scattering

As a check of the results, we used the analytical relations given in Peterson (2004) [22], which provide the radial distribution of the scattered light on the detector generated by in-field sources. The relations are valid for optical elements with a Harvey scattering profile, which is the one we used in the simulations. The in-field stray-light irradiance as a function of the radial distance r from the image on the detector is given by:

$$E_{SL,j} = \pi T (na)^2 \frac{a_{ent}^2}{a_j^2} b_0 \left[1 + \left(\frac{(na) r}{l \; a_j} \right)^2 \right]^{s/2} E_{ent} \tag{2.25}$$

where T is the instrument transmission, $na = 0.1227$ is the numerical aperture of the system, $a_{ent} = 57.3$ is the beam diameter at the entrance, a_j is the beam diameter at the j-th element, b_0, l and s are the three parameters of the Harvey model and E_{ent} is the irradiance from the source at the entrance of the instrument. For each optical element of the RC configuration, we calculated the expected radial distribution of scattered light from equation 2.25 and we compared it with the one obtained in the ray-tracing simulation. The results are reported in figures 2.28 and 2.29. In general, the stray-light simulated by ray-tracing is in good agreement with the analytical predictions. The results for the primary mirror are very noisy, due to the bad statistics of rays on the detector that make the comparison difficult but, for the other cases, the curves are almost overlapping. For all the elements, the simulated irradiance is a bit lower than the theoretical one, meaning that part of the energy is lost. This is due to the fact that rays are terminated when their energy goes below a given threshold, in order to speed up the simulations. Finally, there is a non-perfect agreement for the light scattered by the window, particularly on the "wings" of the distribution. This is attributed to the analytical model provided by Peterson, which makes the assumption that $sin(\theta) \approx \theta$, good only for small angles. Since the window is close to the detector, the light scattered from the center of the window to the edge of the detector reaches the detector with big angles of incidence and the paraxial approximation is not valid any more.

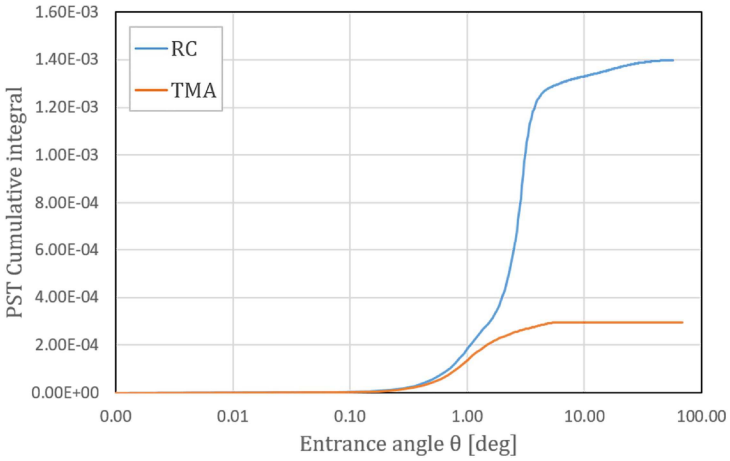

Figure 2.26: PST cumulative integral for the RC and TMA configurations. The scale on the x-axis is logarithmic.

2.12 Conclusions

We proposed two optical solutions for the JANUS camera of the JUICE space mission. The first one is an all-reflective three mirror anastigmatic telescope and the second one is a Ritchey-Chrétien telescope with a three-lens field corrector. Both designs have been studied in detail to characterize their expected image quality and stray light performance.
The two solutions show a very similar performance in terms of optical quality while, regarding stray light, the RC design is slightly underperforming with respect to the TMA by a factor of 2 – 4. Anyway, we would like to stress that the RC design is still under an optimization phase and there is room for improvement. Some modifications to the design are being studied or have been already implemented at the time of writing, with the aim to reduce stray-light on the RC configuration. For example the three-lens corrector has been redesigned to reduce ghosts and the detector mounting has been modified to reduce critical surfaces (i.e. surfaces that can be directly illuminated by external sources and are visible to the detector). From preliminary analyses a factor of 2 improvement is expected in the amount of stray-light of the RC configuration.
For this reason, the current baseline design of the JANUS camera is the Ritchey-Chrétien telescope, also considering the big advantages in terms of weight, alignment and manufacturability of the components. JANUS is currently undergoing the Preliminary Design Review phase (January 2017).

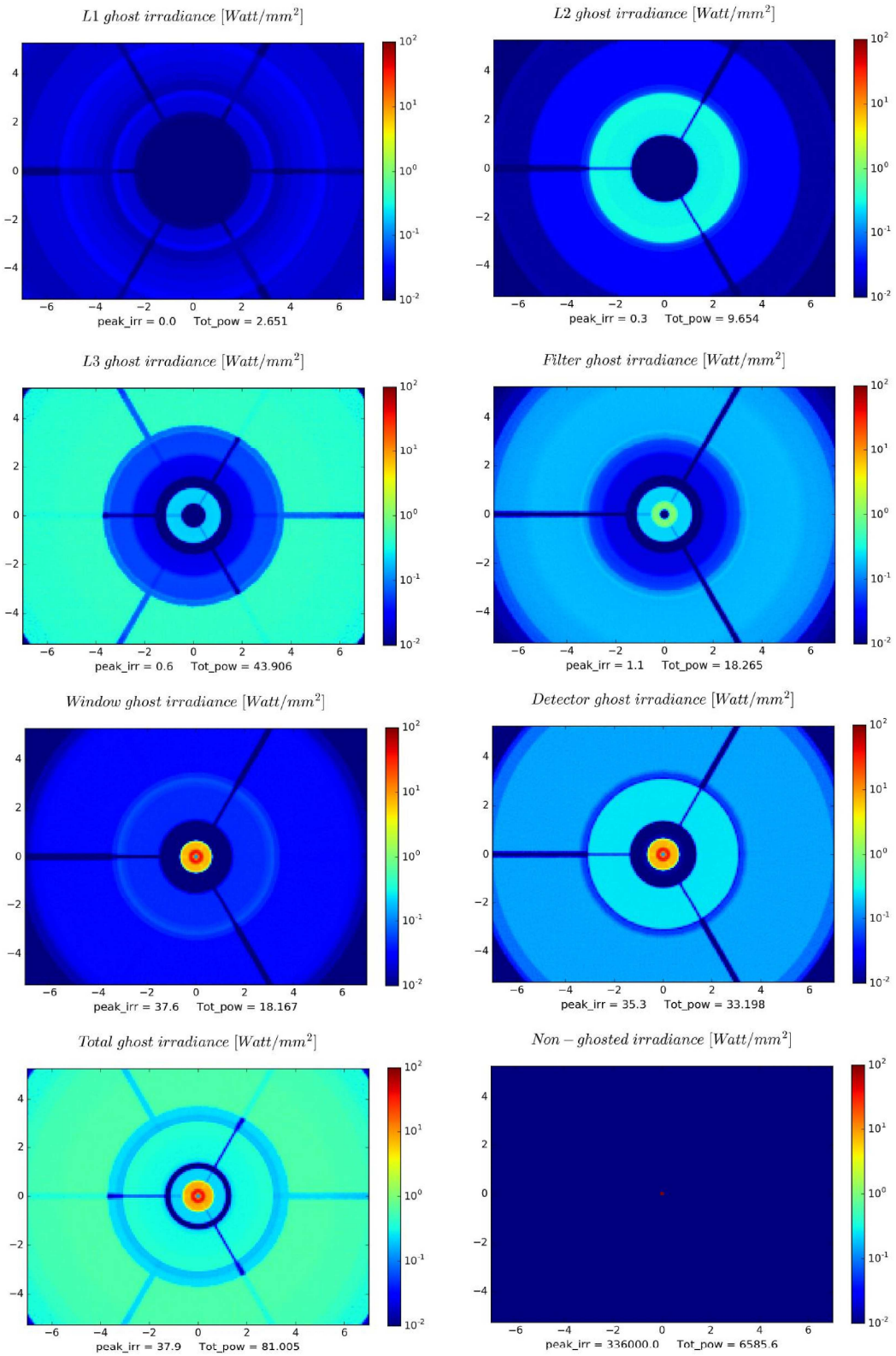

Figure 2.27: Irradiance of the ghost images.

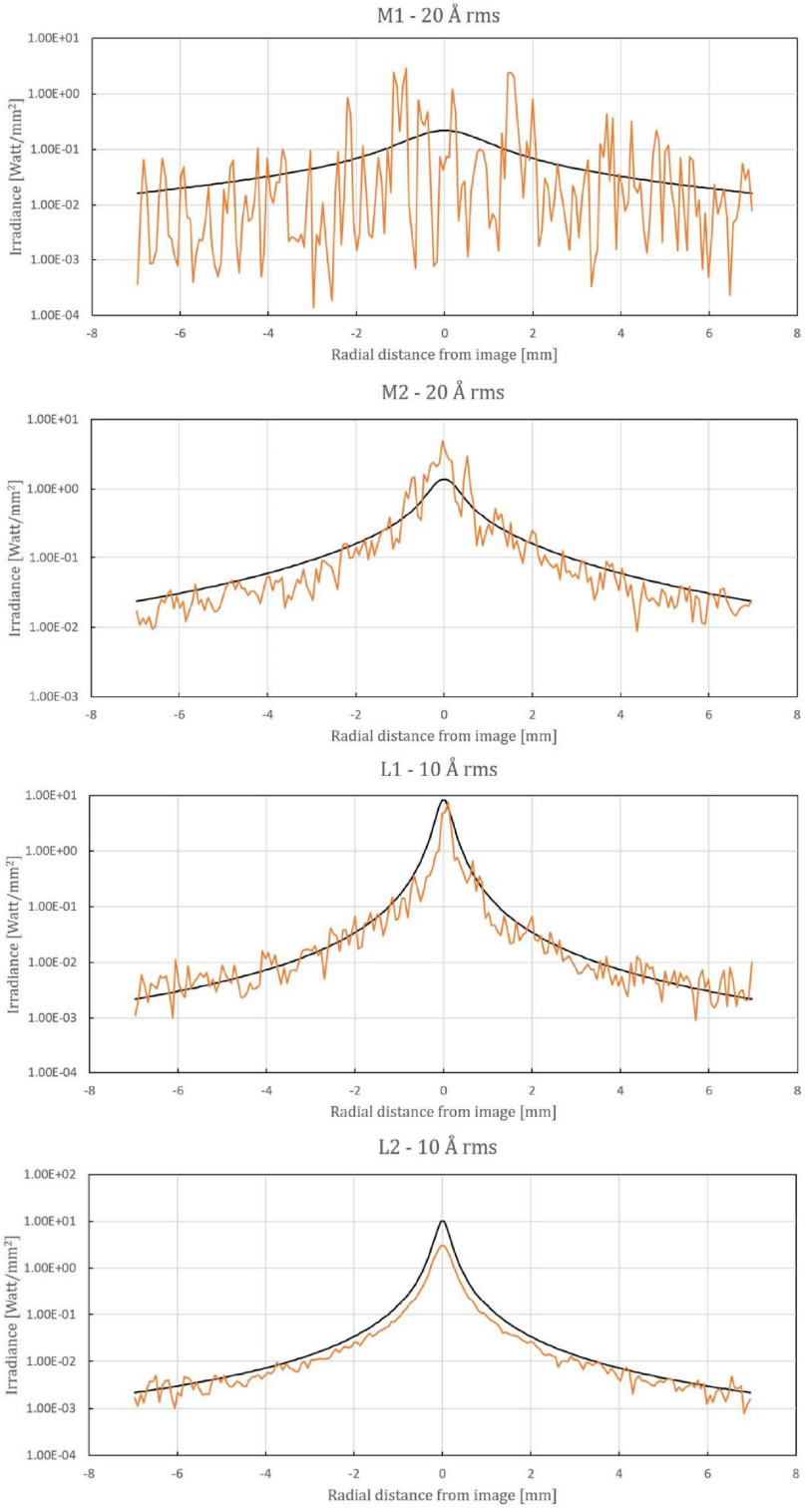

Figure 2.28: Radial irradiance distribution: comparison between analytical model (black curve) and simulation (orange curve).

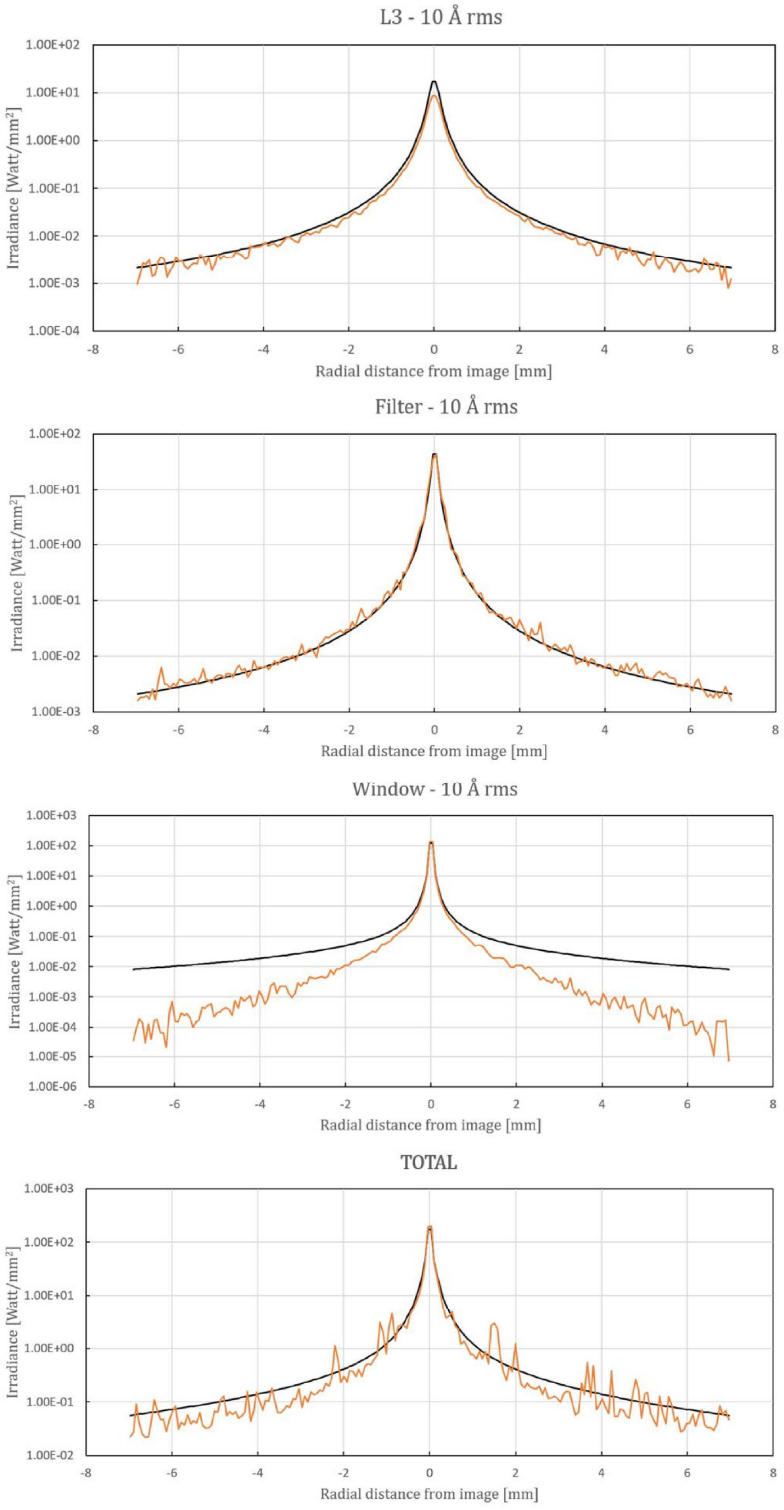

Figure 2.29: Radial irradiance distribution: comparison between analytical model (black curve) and simulation (orange curve).

Chapter 3

SHARK

3.1 Introduction

SHARK is an instrument proposed for LBT in the framework of the *"2014 Call for Proposals for Instrument Upgrades and New Instruments"* [23]. It is composed of two channels, a visible and a near infrared arm, to be installed one on each LBT telescope. SHARK will produce, in its binocular fashion, unique science from exoplanet to extragalactic topics with simultaneous spectral coverage from R to H band, taking advantage of the outstanding performances of the binocular eXtreme Adaptive Optics (XAO) LBT capability. Furthermore, the spectral coverage can be extended to K, L and M bands, thanks to the simultaneous support of LBTI LMIRcam.
Two channels are foreseen, a visible one (SHARK-VIS, see [24] for preliminary experimental results in the visible), operating from $0.5\mu m$ to $1.0\mu m$, and a near infrared one (SHARK-NIR), operating between $0.96\mu m$ and $1.65\mu m$. The instrument successfully underwent a Conceptual Design Review in December 2015, and it has been endorsed for final design and construction. During the PhD, I have been working on the SHARK-NIR channel, as the person responsible for the optical design of the instrument. In the following sections I'll describe the reason for proposing such an instrument, the trade-off choices which lead to the final design, and the work conducted for the design and characterization of the system performance.

3.2 Scientific goals

3.2.1 SHARK-NIR motivation

The initial motivation of SHARK is the idea of building an instrument that can take full advantage of the LBT XAO system, executing a strong science case, which requires such an extreme correction.
Coronagraphy is the direction toward which several astronomical facilities in the world are strongly pushing, both because the performance of the AO systems available today are reaching excellent correction, and because the science case is indeed very interesting. The research of rocky planets with characteristics similar to our Earth is of course very attractive, even if the very high resolution required, due to the vicinity to the star of such planets, is pushing toward telescopes characterized by very large apertures, as the next generation of ELT will be.

Indeed, with the current generation of 8-10m class telescopes, it is possible to explore the area around nearby stars where giant planets are orbiting, still a very interesting research topic. This can be exploited in synergy with the various space mission, which will identify a huge number of possible targets to be then observed from the ground with greater resolution.
Nevertheless, there are AO systems which not only provide performance in term of Strehl that is greater than 90% even in H band, but they are also pushing the high Strehl regime toward fainter magnitudes, making it possible to extend the exo-planets search beyond the few very closeest stars, and increasing considerably in this way the number of possible targets. LBT has, in this sense, a clear advantage with respect to other telescopes, since the Pyramid WFS has a greater sensitivity compared to other commonly used WFS, which can lead to a gain ranging from one to two magnitudes (depending on the seeing conditions) for the 8-10m class telescopes ([25] and [26]).
Additionally, the coronagraphic world is in continuous evolution, and there are several techniques that allow astronomers to get closer and closer to the central star, and to achieve very good contrasts (more than 14 magnitudes of raw contrast at 200mas of distance, and more than 16 magnitudes at distances larger than 400mas [27]).
Furthermore, the LBT AO system provides a very good performance even in the Visible domain (also due to the excellent adaptive secondary mirror (ASM) performance, characterized by a large number of actuators and by a very large actuator stroke [28]), and the performance of both the WFS and of the ASM will soon be improved thanks to an upgrade (SOUL, already endorsed by LBTO) that foresees a new detector with nearly zero RON and a new ASM firmware, capable to halve the mirror settling time (see [29]).
All these arguments led to the idea of SHARK, which is an instrument initially presented and conceived to operate from the VIS to the NIR domain, in binocular fashion, similarly to the way LBC already operates at LBT. After the call for proposals of February 2014, the VIS and NIR channels have been proposed as two instruments, to better optimize the resource allocation and to proceed as fast as possible. The two instruments are absolutely complementary, and most of the science cases presented in the following sections must be executed in binocular observing mode.
Also, considering the international scenario, a coronagraphic instrument in the LBT framework looks to be a favorable choice. In fact, both SPHERE (Spectro-Polarimetric High-contrast Exoplanet RE-search instrument for the VLT) [30], GPI (Gemini Planet Finder) [31] and MagAO (Magellan AO) [32] are operating in the Southern Hemisphere.
In the Northern Hemisphere, the two main competitors are SCExAO (the Subaru Coronagraphic Ex-treme Adaptive Optics) [33] and Palm-3000 (Palomar AO) [34], both of which are already operating on sky with initial performance far from that obtained at LBT, particularly for faint targets. Considering that SCExAO is upgrading its AO system by implementing a pyramid WFS and a 2000 actuators DM ([35]), it will most probably be the only competitor of SHARK.

3.2.2 The scientific case

The direct detection of extra-solar planets is one of the most exciting goals, as already mentioned in the previous sections. Indeed, the resolution achievable with a 10-m class telescope allows us to access, in the NIR domain, gaseous giant planets of Jupiter size or bigger. This is still a very challenging task, due to the very high contrast required and the vicinity to the host star. There are several scientific goals to be possibly exploited in the exo-planet science case,

ranging from the direct detection of unknown giant planets, to the follow up of known planets (through spectroscopic and photometric characterization). The latter requires of course the implementation of a spectroscopic mode with modest spectral resolution, which is currently foreseen in SHARK-NIR through a long slit positioned into the intermediate focal plane.
But the science to be exploited with SHARK-NIR is definitely not only limited to the exo-planet case. For instance, the study of proto-planetary disks is fundamental to comprehend the formation of our own solar system, as well as of extra-solar planetary systems. To understand how matter aggregates to form the building blocks of planetary bodies, there is the need to investigate not only the evolution of the disk itself, but also the role of jets in shaping its structure. This requires observing the system at high angular resolution as close as possible to the parent star, occulting its light to enhance the area where the interplay between the accretion and ejection of matter dominates the dynamics.
Other very interesting and challenging topics can be found in the extragalactic science, where the capabilities of SHARK-NIR in terms of spatial resolution and contrast enhancement may be applied to study the AGN-host relations as well as Dumped Ly-α systems (DLAs) [36], to constrain the Black Hole feeding mechanism and to trace, in bright quasars, molecular outflows powerful enough to clean the inner kilo-parsec and quench the star formation.
There is anyhow an important feature of the LBT AO which, exploited in the proper way, may give to SHARK-NIR the possibility to explore unique coronagraphic science. The Pyramid WFS has a demonstrated gain in sensitivity compared to other WFS commonly used, such as Shack-Hartmann (SH) [37]. This fact gives to the LBT AO systems the capability of achieving high Strehl Ratio (of the order of $SR = 70\%$) at moderately faint magnitude ($R \sim 12$ or even occasionally fainter, depending on the observing conditions), as shown in the impressive collection of FLAO (First Light Adaptive Optics) results reported in Esposito et al. (2011) [38] (figure 3.1). This excellent performance will be further enhanced with the

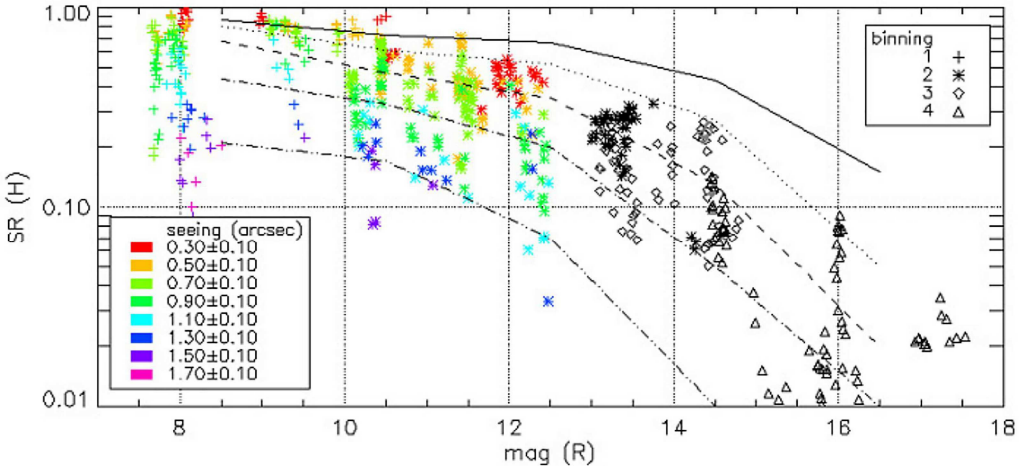

Figure 3.1: A summary of the FLAO performance obtained in H band with different observing

implementation of the AO upgrade SOUL, as shown in figure 3.2 where, depending on the CCD choice, the capability of achieving Strehl as high as 70% can be pushed to stars as faint as magnitude R=13.5. It has to be emphasized that these curves have been computed not in excellent seeing conditions (0.8 arcsec). This performance will open the field of high-contrast AO coronagraphic imaging to stars much fainter than feasible using other coronagraphic in-

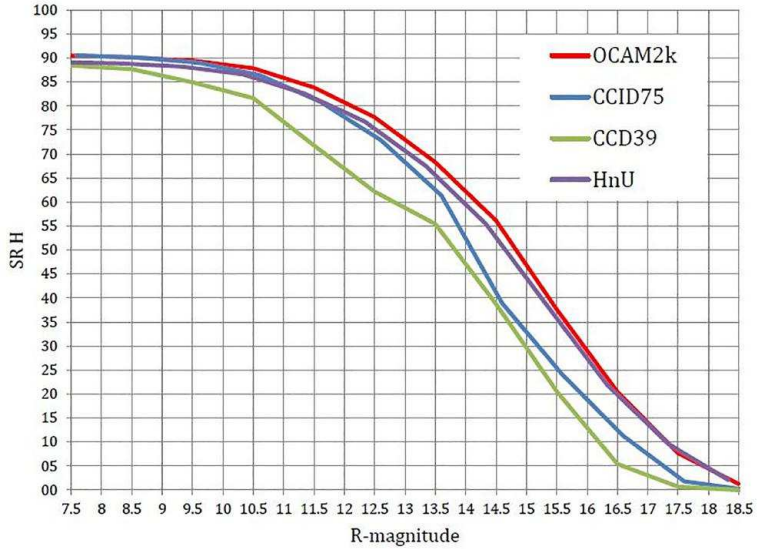

Figure 3.2: the SOUL improvement in the LBT AO performance (green line shows the current performance) with different CCD choices, computed with a seeing of 0.8 arcsec.

struments, allowing deep searches for planets around targets such as M dwarfs in nearby young associations. Also, in the extragalactic field, the sample of AGN and, above all, of quasars to be explored will go from a few tens to a few hundreds, changing the perspective of the science to be achieved. This will be discussed more in detail in the following sections. This is definitely the characteristic which may give to SHARK-NIR unique opportunities in the coronagraphic instrument scenario.

3.2.3 Planets in star-forming regions

The identification and the physical properties of planets in their very early stages will allow us to obtain decisive inferences about the formation mechanisms [39] (core accretion, disk instability, disk fragmentation), together with studying the interactions between planets and disks [40]. Indeed, several features observed in circum-stellar disks, such as spiral arms, gaps, and warps are possibly linked to the gravitational perturbation of planets.
In this context, SHARK may allow the detection of planets in formation phase in the well-studied Taurus-Auriga star forming region [41]. This is northern and thus, badly accessible with SPHERE and GPI. The bulk of the members have ages of about 1-2 Myr, at a distance of about 140 pc. About 350 members have been identified, 130 of which are brighter than R=15. Recently, a survey has been performed by Daemgen and collaborators using Gemini-N [42], yielding the identification of a planet candidate. A candidate in the gap of the circum-stellar disk around LkCa15 has also been proposed by [43] as a possible planet caught in the formation phase.
The search for planets in star-forming regions represents a program capable of fully exploiting the potential of SHARK as proposed. The NIR channel will be used to reveal planet thermal emission. The visible channel could be used for narrow band imaging in $H\alpha$ to reveal signatures of accretion from their circum-planetary disks. Simultaneous observations uniquely allowed by LBT would highly mitigate the issue of variability. Solar-type stars

in Taurus-Auriga SFR represent targets for which LBT is uniquely competitive (faint mag, northern declination). Considering the distance of Taurus-Auriga SFR (140 pc) this science case motivates the instrument design with an inner working angle (IWA) as small as 100 mas.

3.2.4 Giant planets around low-mass stars

This is a special niche for LBT AO at faint magnitudes, especially with the AO upgrade. In the last two years, several members of young moving groups (age 10-100 Myr) were recently identified, with particular focus on low-mass stars [44], [45]. There are several tens of potential targets, depending on the exact magnitude limit of the instrument, accessible for a deep search for planets in wide orbits, thus complementing the results of SPHERE and GPI, which will be mostly limited to solar-type and early-type stars. In particular, with the current limit at R<10.5, our sample comprises 33 targets (basically FGK-type stars), whereas adopting R=12.5 as a magnitude limit would gain us more than a factor of three in sample size (that is, 108 objects).

3.2.5 Spectroscopic characterization of known planets

The physical characterization of the known planets is becoming increasingly important as planet discoveries accumulate. SHARK has the unique capability of performing high-SR imaging in the optical. The planets currently detected in direct imaging are expected to be significantly fainter in the optical than in the NIR ($\sim$ 4 mag in I and $\sim$ 6 in R). The measurement of their fluxes in I and/or R bands would provide a relevant extension of the spectral energy distribution (SED) and would allow a comparison with the atmospheres of highly-irradiated transiting planets. Unexpectedly optically-bright planets, such as Fomalhaut b, can also be identified using SHARK. A long-slit spectroscopic (LSS) coronagraphic mode will be implemented with two different resolutions: a low-resolution mode ($R \sim 100$), in order to target faint targets, and a medium-resolution mode ($R \sim 1000$) to get spectral information for the brightest objects, by resolving molecular features and thus inferring their chemical properties. For example, we will be able to obtain medium-resolution spectra for planetary systems orbiting HR8799 [46] (see Figure 3.3 - LMIRCAM L' band observations for HR8799 systems).
These LSS observations would shed light on the L-T transition (e.g. [47]) and on the characteristics of brown dwarfs and giant planets, which are expected to somewhat overlap but also significantly differ in terms of chemistry of the atmospheres and mechanisms of cloud formation.

3.2.6 Disks and Jets around young stars

The circumstellar environment of a young star, where planets are believed to form, consists of an accretion disk and its associated stellar jets. The study of proto-planetary disks is fundamental to comprehend the formation of our own solar system, as well as that of extra-solar planetary systems.
Optical and NIR diffraction limited images reaching angular resolutions of 20-40 mas obtained with a coronagraphic mask of 100 mas and a camera with a pixel scale of 5-20 mas/pixel will allow us to reach contrast ratios of $10^4 - 10^5$, hence probing the small (μm-size) dust grains in the disk through scattered light imaging down to a few AU from the star. This is crucial to probe the disk structure and planetary dynamics in the planet-forming region (<30 AU).

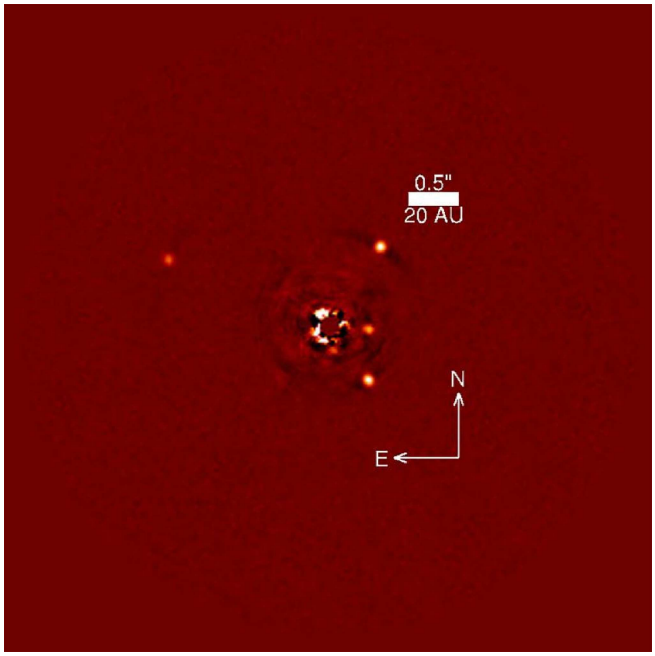

Figure 3.3: LMIRCAM L' band observations of the HR8799 system. [46]

For example, the detection of asymmetries in the spatial distribution of dust, such as warps, gaps, spirals, and rings, provides evidence for unseen co-orbital planetary-mass companions through their dynamical interactions with the disk grains (e.g., [48]).
AO observations of the base of jets disclose a clear picture of the jet as close as possible to the launching point and of the instabilities and shocks in the flow. Conversely, measurements of jet opening angles and collimation scales can give stringent constraints on the launch mechanism and the consequent removal of angular momentum from the disk. Coronagraphy with a 50-100 mas occultation would constitute a big leap in the observational modes available today, and would allow, in principle, to sample the jet as close as 10 AU from the source in nearby systems like Lupus and Taurus (a contrast of $10^2 - 10^3$ is sufficient to image the bright jet nebulae). This distance is within the upper boundary of the acceleration region. Also, the imaging mode of LBT/SHARK can reach an angular resolution of 50 mas (FWHM) in the infrared (and foreseen 25 mas in the VIS channel), to be compared with the 100 mas of HST in the visible. In addition, in the case of jets the targeted radiation is concentrated in emission lines, so an obvious improvement on the contrast is obtained using the coronagraph in combination with a narrow-band filter. Finally, the subtraction of the stellar PSF cleans the image to its best. These steps allow one to form much deeper images of the jet close to the star than ever been attempted.

3.2.7 Extragalactic science with SHARK

The unique capabilities of SHARK in terms of spatial resolution and contrast enhancement can be also used to study the feeding/feedback mechanism in nearby sources, the AGN-host relations, and the dumped Ly-α systems (DLAs). In this context the goals will be: (1) to discover and fully characterize the AGN close pairs; (2) to constrain the Black Hole feeding mechanism (e.g. supernovae driven winds vs gravitational asymmetries) in local

Seyfert galaxies, and (3) to trace, in bright quasars, molecular outflows powerful enough to clean the inner kpc and quench the star formation (SF). This will be done by mapping dust lanes on scales down to hundred pc, and by investigating whether outflows are dusty or rather the AGN feedback has already swept the ISM. Moreover, color maps and IFU follow-up of SF regions in the galaxy nucleus and disk, will allow to constrain the SF rate, the age, and the metallicity.

3.3 Requirements

The basic idea of SHARK-NIR is a camera for direct imaging, coronagraphy and spectroscopy, using the corrected wavefront provided by the LBT ASM, operated through the existing AO WFS. Since SHARK-NIR is also a coronagraphic instrument, the camera has to be designed to deliver extreme performance, iin order to not decrease the correction provided by the AO system. In fact, all the coronagraphic techniques that may be implemented need a SR as high as possible to provide very good contrast. This require optics machined to state-of-the-art technology and polished to nanometric level of roughness, properly aligned and installed on very robust mounts. The whole instrument mechanics has to be very stiff and designed to minimize the effect of flexure.
Additionally, to maintain the performance at every observing elevation, it is necessary to implement an Atmospheric Dispersion Corrector (ADC) to compensate for atmospheric differential refraction.
Moreover, some of the foreseen science cases require field de-rotation. Hence, the whole instrument has to be mounted on a mechanical bearing.
A very suitable position for the installation of SHARK-NIR is at the entrance of the Large Binocular Telescope Interferometer (LBTI, see figure 3.4), very close to the WFS that is dedicated to LBTI itself. The WFS should be used to sense and drive the ASM, providing the corrected wavefront to SHARK-NIR. A dichroic mirror, deployable in front of the entrance window of LBTI, shall pick-up and re-direct the wavelength range between 0.9 and 1,7 μm toward SHARK-NIR, transmitting the VIS light to the WFS. The volume available for SHARK-NIR is quite small, limited by the telescope rotator flange on one side (red in figure 3.4) and by the LBTI structure on the other (gray and green in figure 3.4). This constraint, along with other more general considerations (thermal background, instruments available at the LBT, etc...), lead to several modifications and trade-offs at design level, which will be summarized in the following section.

3.3.1 Instrument trade-off

The first design proposed for SHARK-NIR was characterized by a working waveband in the range $1 - 2.4\mu m$ covering the J,H and K photometric bands [49]. The camera was very simple. It was composed of a couple of off-axis parabolae: one used to re-image the pupil on an intermediate pupil plane where the Lyot stop was placed, the second one to make the image on the scientific detector, a 2048x2048 HAWAII 2 detector covering a FoV of 30x30 arcsec. The occulting mask was placed at the F/15 entrance focal plane of the telescope and the entire instrument was enclosed in a cryostat at liquid nitrogen temperature to minimize thermal background. This necessity had the following consequences:

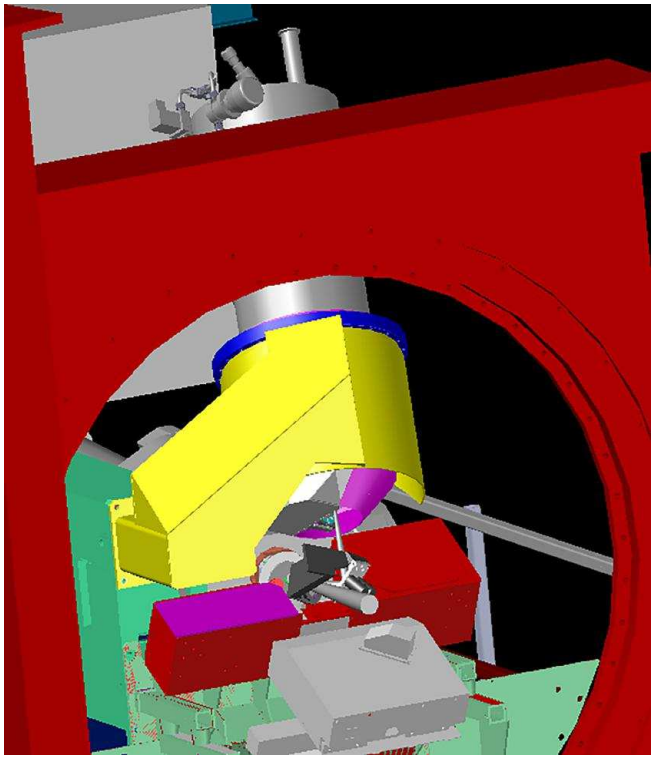

Figure 3.4: The SHARK-NIR instrument positioned at the entrance of LBTI

- Size requirement: the whole optical design was required to be as compact as possible, and this did not allow us to implement several coronagraphic techniques with different requirements (e.g. the presence of an intermediate pupil plane, prior to the occulting mask, for apodization)

- Optics material: to minimize the stress between the various opto-mechanical components, when going from ambient to operating temperature, the fully reflective design was foreseen to be implemented using aluminum optics, in order to keep the same CTE of the mechanics. On the other hand, aluminum optics, despite being light and suitable for cryogenic systems, can be machined only up to a certain level of micro-roughness, limiting the nominal performance of the full optical train.

During the Conceptual Design Phase (CDP), we studied an alternative design of SHARK NIR-Channel, which is the one described in this thesis, considering a camera operating from 0.9 to 1.7 μm and characterized by a FoV of about 15 arcsec. This arose from the strategy proposed by LBTO of developing an instrument as much as possible complementary with the other NIR cameras present at LBT, in a way to maximize the synergy between the LBT instruments. After the official start of the CDP (May 2015), there was a discussion inside the science group and between the partners to assess the real needs of the different science cases, considering the different capabilities of the instruments already installed at LBT and the foreseen upgrades of some of them (such as SOUL and the upgrade of LMIRcam). The resulting message was very clear, and is summarized in the following:

- SHARK-NIR, as presented in September 2014, had a FoV of the order of 30 arcsec; since

a camera with these characteristics, LUCI, had successful first light reaching good Strehl performance (of the order of 75% on axis, which may even increase with additional fine tuning of the instrument), why push for a 30 arcsec FoV camera? From the science point of view, supposing that SHARK NIR will reach top Strehl ratios of the order of 90% or greater, no scientist could envisage a scientific target, in direct imaging, for which the small increase of Strehl (from 75% to 90%) is needed in a FoV larger than few arcsec, considering that the isoplanatic angle is causing a very considerable performance degradation in terms of Strehl going off-axis. For all the coronagraphic science cases, the maximum FoV is ranging from a few arcsec to maximum 10-15 arcsec.

- All the partners have been pushing on the project schedule. Above all, for the exo-planet science case, a fast-track project is mandatory to produce outstanding science. In this framework, we have received from some partners the suggestion to consider the possibility to have an instrument operating only in J and H band, having in this way only the camera cryogenic, with some advantages: the instrument design and AIV would be simpler and faster, there would be more space available (no large tank needed) and, moreover, it would be much more simple to implement more efficient coronagraphic techniques, adding scientific appeal to the instrument.

These arguments pushed us to make the alternative design, characterized by a smaller FoV and by a non-cryogenic design (except the detector, which still needs to be cryo-cooled), covering the wavelength range 0.9-1.7 μm.
Of course, to give up the K band has its drawbacks in the science that can be performed with the instrument itself. First of all, we compared the achievable contrast, for the classical Lyot technique, in H and K band. The contrast loss by giving up the K-band is about a factor of in bad seeing conditions, while it is of the order of 25% in good seeing conditions. This loss is expected to be largely compensated by using more efficient coronagraphic techniques.
In exo-planet science, we need to exploit photometric techniques in different bands in order to build up the spectral energy distribution (SED) of sub-stellar objects and to define the L/T transition (for example, in the colour-magnitude plane J vs J-H, see [50]). The more extended the spectral coverage, the better we can characterize the exoplanet properties. The counterpart to the H-band observation with SHARK-NIR can come from L' coronagraphic observations carried out with LBTI.
On the other hand, other scientific cases need to obtain data from molecular oxygen lines, the strongest of which are in the K band. Also in this framework, an agreement with the LBTI group is under definition, with the goal to exploit the synergy with a coronagraph working in the K band on LMIRcam.
Given the choice of optimizing the design for a smaller bandwidth (which does not require cold optics) and for a smaller FoV, we take advantage of the saved space (given the envelope allowed by the telescope interface) to increase the complexity of the optical design. This is particularly interesting in view of introducing an intermediate pupil plane. This, of course, requires an increase in the number of optical elements in the design, which has also the drawback to slightly decrease the total throughput and increase scattering. This throughput loss can be estimated comparing the number of reflecting surfaces in the two designs. The original design presented included 2 off-axis parabolic mirrors (OAPs) and 3 folding mirrors, while a design which also re-images an intermediate pupil plane includes 4 OAPs, 3 folding mirrors and a DM, which means an increase of 3 reflections. If we only consider the mirrors contributions (neglecting ADC, masks and filters, for the moment), assuming a conservative

98% reflectivity for each mirror, this would reduce the overall throughput by about 5%. On the other hand, the bandpass cut-off change (from K to H) relaxes the requirements on the thermal behavior of the opto-mechanical design, since the thermal range is reduced a lot, not being the full optical train cryogenic anymore. As already mentioned, glass mirrors (instead of the previously foreseen Aluminum ones) can be used, and this choice could improve the performance of the system in terms of scattered light (lower micro-roughness). The huge advantage of a design in which the pupil plane is re-imaged is the flexibility of the overall system to the implementation of different and more sophisticated coronagraphic designs, already implemented in other planet finders (GPI, SHERE), like the Apodized Lyot or the Shaped Pupil [51].

3.4 Optical design

3.4.1 The science channel

To achieve the desired science goals foreseen for SHARK, and based on the trade-off considerations given in the previous section, the optical design of SHARK should meet the following requirements:

- the implementation of two intermediate pupil planes and one intermediate focal plane for coronagraphic purposes.
- operation in the wavelength range from 0.95 to 1.70 μm.
- Nyquist sampling of the PSF on the scientific camera at the shortest wavelength, translating to a plate scale of 14.5 mas/px.
- atmospheric dispersion correction adjustable to the altitude of the object.
- minimization of wavefront errors introduced by the instrument to minimize Non-Common Path Aberrations (NCPA).
- implementation of an internal tip-tilt mirror to keep a perfect centering of the star PSF on the occulting mask during observations. The TT mirror will be driven by a dedicated wavefront sensor.
- provide enough space for the positioning of a filter wheel for each of the coronagraphic planes plus a couple of wheels for science filters and neutral density filters.
- provide a long-slit spectroscopic mode with low ($R \sim 100$) and medium ($R \sim 1000$) resolution.
- study a calibration unit for flat field and wavelength calibration of the instrument.

The requirements allow some degrees of freedom in the optical design. For example, the size of the intermediate pupils and the plate scale on the intermediate focal plane are not strictly fixed, although some limitations due to manufacturing constraints apply. From this point of view, a greater pupil diameter is to be preferred because small scale structures on coronagraphic masks are easier to produce. The lower limit to pupil diameter set by manufacturing constraints of the coronagraphic masks is of the order of $D \sim 11 - 12mm$.

On the other hand, bigger pupils means also bigger optics and larger filter wheels, which is a big problem given the very small volume available. For this reason, it is required to do a careful trade-off between pupil size and instrument size, not forgetting that also étendue conservation will play a significant role. In fact, although the FoV is very small (15×15 arcsec), the de-magnification factor between the entrance pupil and a 12mm pupil is 8220/12=685, which means that the field angles at the small pupil will be of the order of 2-3deg.
The relay optics used to make the intermediate images of the pupil and focal planes are Off-Axis Parabolic (OAP) mirrors. There are four parabolic mirrors in total: the first to make the first image of the pupil, the second to make the intermediate focal image, the third to make the second pupil image and the fourth to produce the scientific image on the detector. The relation between the off-axis angles of the parabolae and their magnification factor was optimized as described in Ghedina (1997) ([52]). This approach allows us to achieve a very good optical quality but imposes some restrictions on the direction of the light beam. In particular, for each pair of parabolae, the outgoing beam is bent on the same side of the incoming beam, as depicted in figure 3.5. For this reason, in order to avoid superposition of the optical components and keep the instrument to a very small volume, three additional flat mirrors are used to fold the system.
Another aspect to consider in the design is the position of the tip-tilt mirror. The optimum

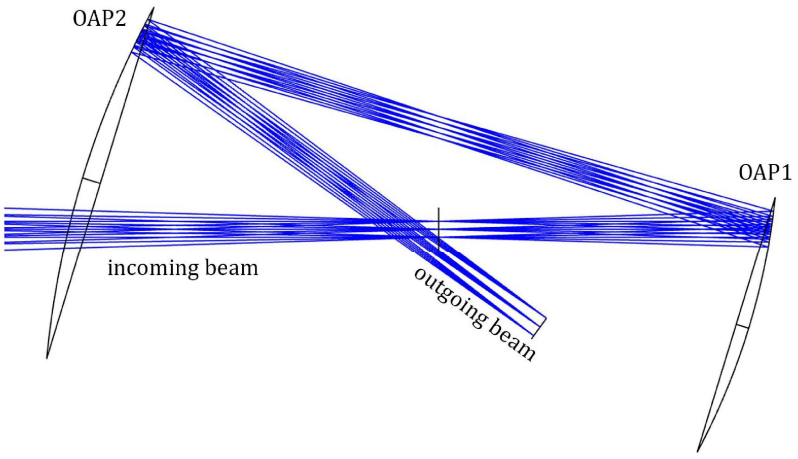

Figure 3.5: Optimum configuration for two off-axis parabolae used as collimator and camera respectively.

position of the internal tip-tilt mirror is the first pupil plane. The reasons are the following: (1) a tilt of the mirror should not shift the following pupil image, (2) the correction needs to be performed before the occulting mask. Unfortunately, the TT mirror is not the only optical component that should be placed at the first pupil plane. In fact, the apodizing masks for coronagraphy and the ADC should also be placed as close as possible to this pupil plane. Apodizers are generally optimized with numerical codes based on fourier transformations between focal planes and pupil planes (see [53]), so they give the best performance when placed at the pupil plane. ADC, on the other hand, compensate the fact that rays of different wavelengths enter the telescope with different angles because of atmospheric refraction. Since the ADC acts directly on the ray angles, if the correction is performed far from the pupil, the ADC will generate a transverse chromatic aberration on the following pupil planes. Actually,

this also happens when placing the TT mirror far from the pupil: a tilt far from the pupil plane will produce a shift of the pupil position. Since in the case of the ADC the tilt is wavelength dependent, several pupils will be produced with a position dependent on wavelength. Moreover, the ADC needs to be placed before the occulting mask, in order to efficiently block the light of the star.
Given the very small volume available, a trade-off was necessary and the adopted solution is characterized by the TT mirror placed exactly at the pupil plane, followed by the apodizer and then by the ADC. The effect of placing the apodizer out of pupil has been estimated via coronagraphic simulations and the deterioration in performance is negligible. The chromatic aberration introduced by the ADC has been estimated with Zemax and is presented later.
Figure 3.6 shows the optical layout of SHARK-NIR prepared for the Final Design Review. The overall size of the optical assembly is quite small and can be mounted on an optical bench ~ 300 mm wide and ~ 800 mm long. Following the light path from the left side of the figure, the light beam from the telescope is picked-off before the Nasmyth focus by a dichroic mirror which directs the light between $\lambda = 0.9\mu m$ and $\lambda = 1.7\mu m$ inside SHARK-NIR and transmits the visible light to the WFS of LBT. Then, the light is directed inside the instrument by a motorized TT mirror (IN-TT in figure 3.6). The motorized axes are able to center the pupil image on the coronagraphic masks with a precision better than $1/100^{th}$ of the pupil diameter. The rest of the instrument is enclosed by a cover to prevent particulate contamination of the optics. The light enters the instrument through a flat entrance window. All the optics after the window are placed on an optical bench, which can be mechanically de-rotated through a bearing (see figure 3.7). The science channel is composed as follows:

- An off-axis parabola (OAP-1) creates a pupil plane of 11.2mm of diameter at the internal TT mirror. Here, the TT mirror could also be replaced by a DM for low order correction of NCPA (in order to avoid using the pyramid dynamic range of FLAO). The size of the pupil, and the volume around it, is compatible with the ALPAO DM9715 containing 97 actuators, a pupil diameter of 13.5 mm and actuator pitch of 1.5 mm.

- A filter wheel will select between different apodizing masks, which are positioned 50mm after the pupil plane.

- Immediately after, in the collimated beam, the ADC is placed.

- Between the ADC and the second off-axis parabola (OAP-2), a beam splitter will send a small portion of the light ($5 - 10\%$) to the tip-tilt sensor (which is placed out of the plane of the page in figure 3.6), composed of a lens and a commercial detector sensitive to J band. The TT-WFS would give the advantage of monitoring (at low frequency, once every minute for example) possible drifts of the spot during a single exposure, to be then compensated with the local DM, ensuring in this way proper mask alignment.

- OAP-2 refocusis the beam on an intermediate focal plane with an $F/\# = 22$, where a filter wheel can select between different occulting masks. The same wheel will accommodate the slit for the spectroscopic mode, to do spectral characterization of the science targets. The clear aperture required for the filters in this focal plane, in order to not vignette the FoV, is about 1 inch in diameter.

- After a folding mirror (FM-1), a third off-axis parabola creates the second re-imaged pupil plane, where a filter wheel can select between different pupil stops used to properly

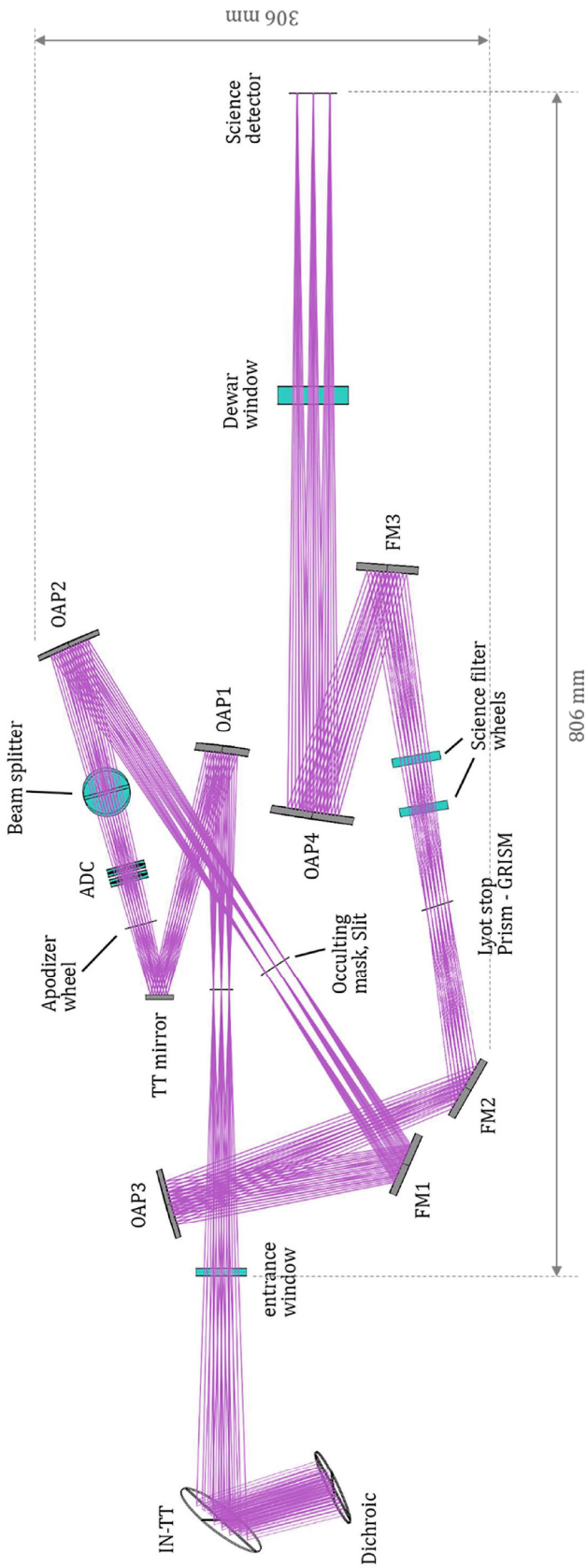

Figure 3.6: Optical layout of SHARK (top view of the optical bench). The light beam enters the instrument on the left side of the figure.

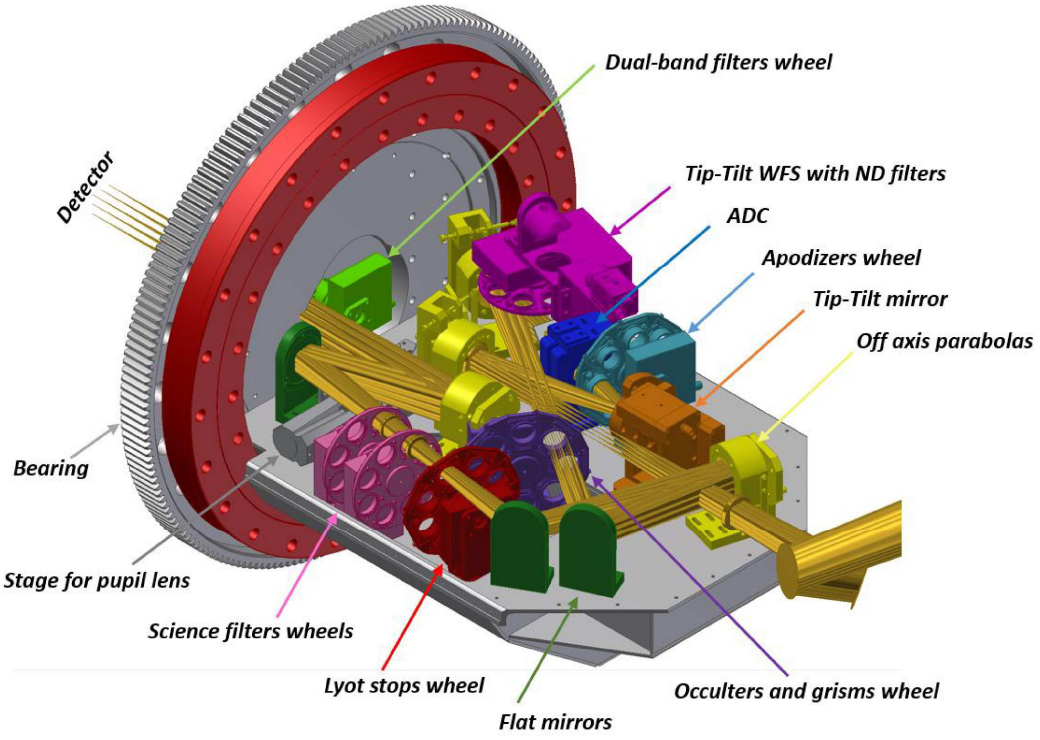

Figure 3.7: Opto-mechanical concept of the SHARK-NIR optical bench.

mask the spiders and the secondary mirror, to minimize diffraction effects (Lyot stop in figure 3.6). The pupil diameter is 14.9 mm. The dispersive elements for the spectroscopic mode will be placed in the same wheel.

- In the collimated beam, two additional filter wheels (positioned between the pupil plane and a folding mirror, (FM-3) will allow the insertion of the scientific filters.

- After this folding mirror, the fourth off-axis parabola (OAP-4) creates the final focal plane (FP) on the detector. A deployable small optical group (an achromatic doublet), not shown in figure 3.6, can be inserted between OAP-4 and the dewar window to create an image of the pupil on the detector. This can be used to align the coronagraphic pupil masks before observation and for general diagnostics.

The entrance window of the dewar is kept at 200mm distance from the detector, 180mm being the minimum length of the cold baffle, which has to be implemented in front of the camera to minimize the thermal background.
Table 3.1 gives a list of the characteristic of each optical element. The diameter of the optics is in the range between 1" and 2".

3.4.2 Nominal optical quality

SHARK-NIR is a coronagraphic instrument based on XAO. Hence, it is of paramount importance that the nominal optical quality be kept as high as possible (few nanometers rms), especially in the central regions close to the star where the AO correction can reach SR as high

Element	R_{curv}	**Diam.**	**Off-axis**	**Material**	**Thickness**
Dichroic		54 mm		fused silica	≈8 mm
IN-TT		70 mm		mirror	
Ent. window		35 mm		fused silica	5 mm
OAP-1	330 mm	36 mm	-45.188 mm	mirror	
TT-Mirror		18 mm		mirror	
Apodizer		≈12 mm		TBD	
ADC-1		26 mm		ZnS/ZnSe	5 mm
ADC-2		26 mm		ZnS/ZnSe	5 mm
Beam splitter		44 mm		fused silica	3 mm
OAP-2	480 mm	44 mm	-72.807 mm	mirror	
FM-1		44 mm		mirror	
OAP-3	650 mm	48 mm	75.549 mm	mirror	
FM-2		44 mm		mirror	
Lyot stop		≈15 mm		TBD	
Sci filter 1		25.4 mm		fused silica	3 mm
Sci filter 2		25.4 mm		fused silica	3 mm
FM-3		42		mirror	
OAP4	919.838 mm	56 mm	125.953 mm	mirror	
Dewar window		50.8 mm		fused silica	12 mm

Table 3.1: Surface data for the optical elements of the science channel.

as 95% in the case of bright targets and good seeing conditions. In the outer regions, the AO correction drops very quickly, due to the anisoplanatic angle of atmospheric turbulence. At these positions, a slightly worse image quality can be tolerated. To evaluate image quality, we considered the polychromatic rms wavefront error at the exit pupil of SHARK as a function of the field position. The resulting wavefront rms map appears in figure 3.8. The wavefront rms error is of the order of a few nanometers in almost all the image frame, except the corners of the image where the quality drops to a few tens of nanometers of wavefront error. The best image quality is not achieved at the on-axis field because of the optimization over the whole FoV. However, the wavefront error on the central part of the image can be considered negligible with respect to other sources of error (i.e. alignment and manufacturing). The corresponding Strehl ratio map is represented on the right of figure 3.8. The nominal SR is greater than 94% all over the FoV and is of the order of $SR \sim 99\%$ in the central part. In the same way, we also evaluated the image quality on the coronagraphic focal plane, where the occulting mask is placed. The rms wavefront error map is very similar to the one of figure 3.8 with $SR \sim 99\%$ in almost all the frame, dropping at the edge of the FoV to $SR = 97\%$. Of course, the polishing errors and alignment errors will add to the nominal wavefront error, decreasing the optical quality. A budget will be provided in the tolerance analysis presented later.

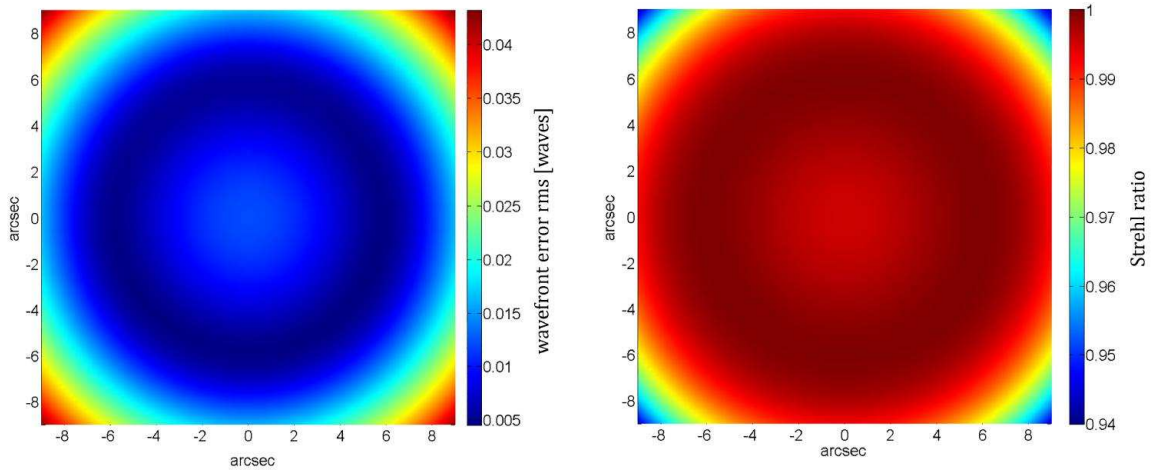

Figure 3.8: Left: nominal polychromatic wavefront error of SHARK-NIR at the scientific focal plane. Right: strehl ratio map corresponding to the plot on the left.

3.4.3 Atmospheric Dispersion Corrector

The masking efficiency of the light of the central source is related to the quality of the PSF at the intermediate FP in which the mask is placed. In addition to turbulence, the atmosphere also produces a chromatic dispersion which introduces a wavelength dependent tilt term to the incoming wave-front. The strength of this effect depends mainly on the Zenith angle of observation and on the wavelength range, and it can deteriorate the PSF significantly. To evaluate the dispersion effect of the atmosphere, we have used an atmospheric surface in the Zemax software. The parameters used are listed in figure 3.9 (left).
Figure 3.9 (right) shows the atmospheric dispersion for the wavelength range 1.1 – 1.4 μm as a function of the Zenith Angle (blue line). The orange line represents the angular dimension of the Airy radius (projected on sky) for the wavelength 1.2 μm. It is clearly visible that, for Zenith angles greater than ~ 20, deg the atmospheric dispersion needs to be corrected.
To correct for atmospheric dispersion, we use a corrector made up of two counter-rotating Amici prisms (see [54]). Each Amici prism is composed of two cemented prisms made from glasses with different dispersion. The angles of the prisms are chosen in such a way as to provide zero deviation for a central wavelength and produce a dispersion equal to half that of the atmosphere. The working principle of this atmospheric dispersion corrector is sketched in figure 3.10 (left). When the prisms are positioned as in figure 3.10 (a) their dispersive power adds up, while when they are rotated by 180 deg (configuration b), their dispersive power cancels out. For intermediate angles of rotation, they correct a smaller amount of dispersion, so it is possible to tune the system to correct different Zenith angles. In order to limit aberrations, as discussed in Wynne (1984) [55], it is necessary to use two glasses with similar refractive index for the central wavelength, but different dispersion. In the IR wavelength range, this is a more difficult task, due to the smaller number of available glasses. In our design, we used Zinc Selenide (n=2.47 at $\lambda = 1.25$ μm) as the high dispersion glass and Zinc Sulfide (n=2.28 at $\lambda = 1.25$ μm) as the low dispersion glass. The high refractive index of these glasses allow to achieve the required dispersion with small apex angles of the prisms, resulting in a more compact design. The optical layout of the ADC and the properties of the prisms are shown in figure 3.10 (right).

Parameter	Value
Zenith angle	$0 - 65$ deg
Height	3221 m
Temperature	273 K
Pressure	670 mbar
Humidity	0.5
Latitude	32 deg

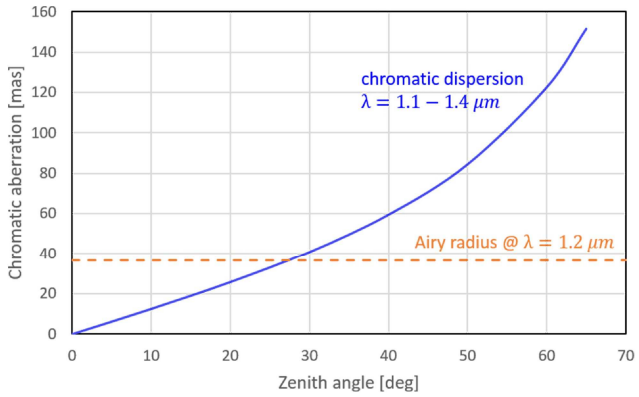

Figure 3.9: Left - Parameters used to simulate atmospheric dispersion. Right - Blue line: Dispersion for the wavelength range $1.1 - 1.4$ μm as a function of the Zenith Angle. Orange line: dimension of the Airy radius (equivalent to the FWHM of the Airy disk) for the J band (1.2 μm).

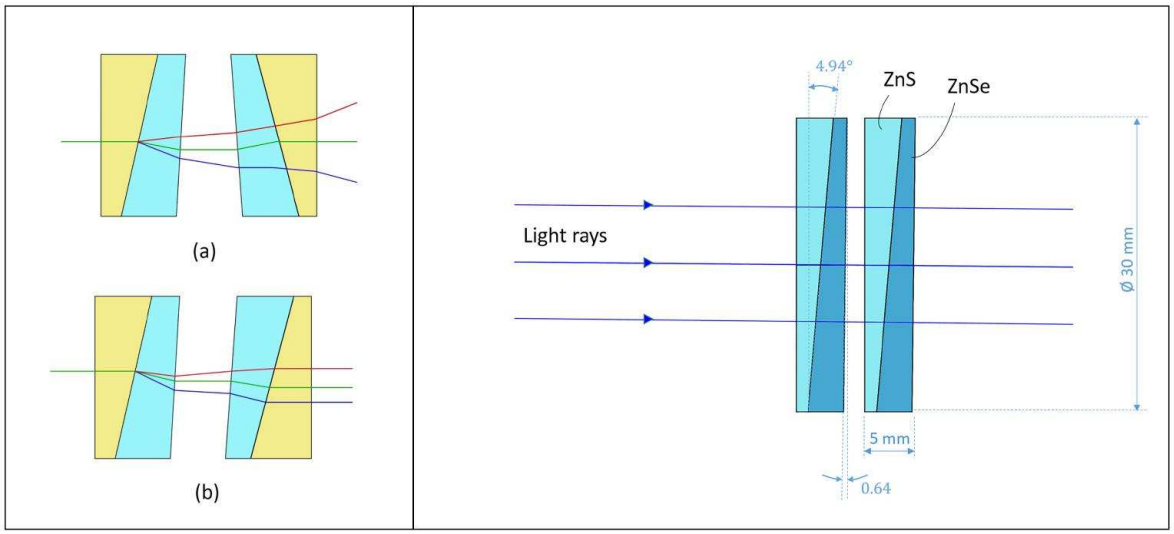

Figure 3.10: Left: Working principle of the counter-rotating Amici prisms. (a) The orientation of the two prisms produces the maximum dispersion; (b) The effect of the two prisms cancels out and gives zero dispersion.Right: SHARK-NIR ADC corrector with specifications.

The diameter of the prisms is 30 mm and the central thickness of each Amici prism assembly is 5 mm (2.5 mm for the ZnSe prism + 2.5 mm for the ZnS prism). The system is designed to correct until a zenith angle of 65 deg. The corrector is placed in the collimated beam, 80 mm after the first image of the pupil.

ADC performance

The combined effect of atmospheric dispersion and ADC is visible in figure 3.11, which shows the on-axis spot diagrams for different zenith angles up to the maximum working ZA of 65 deg. The atmospheric dispersion is very well corrected, but a residual lateral chromatic aberration is still visible, due to the mismatch between the atmospheric dispersion law and the dispersion of the glasses used in the ADC. This partial correction slightly deteriorates the image quality (see figure 3.12). For example, when observing at a ZA=50 deg, the on-axis SR decreases to $\approx 98\%$ while the SR at 10.8 arcsec radial field decreases to $\approx 94\%$.

When the ADC is rotated, there is also a small movement of the image on the FP. We have

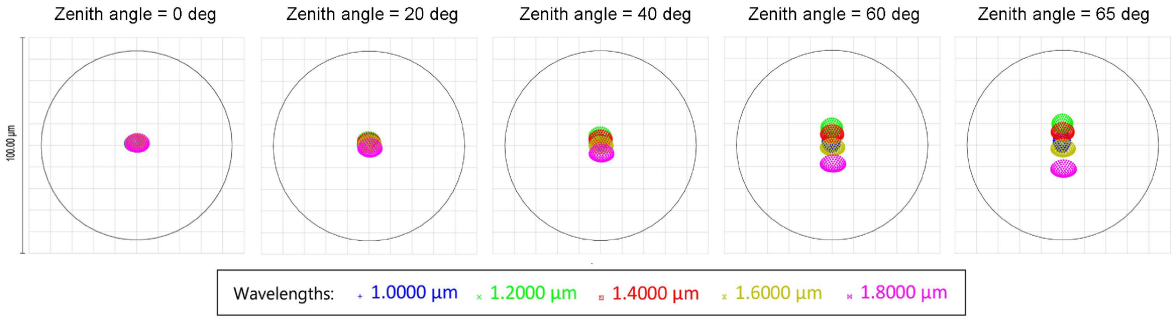

Figure 3.11: On-axis spot diagram at the scientific focal plane for different zenith angles. The circle represents the Airy disk at $\lambda = 1.2\ \mu m$ while the side of the box is 100 μm long. The ADC keeps the chromatic dispersion within the Airy disk until the maximum working zenith angle of 65 deg.

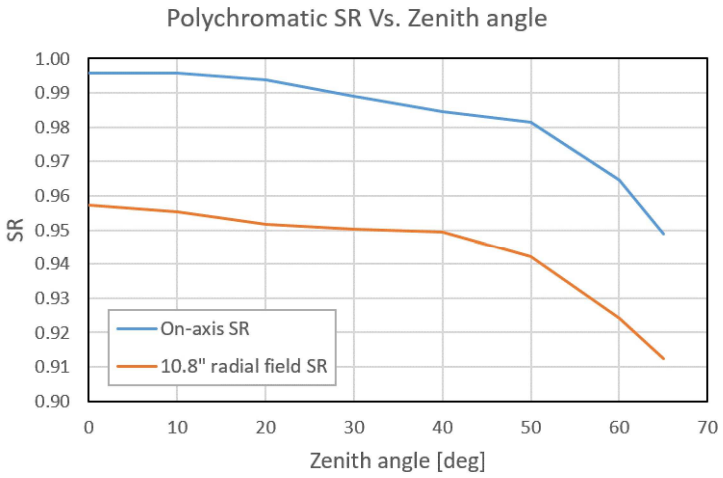

Figure 3.12: Optical quality when observing with the ADC as a function of the Zenith angle. The blue curve represents the on-axis SR while the orange curve represents the SR at the corner of the detector

estimated this movement by calculating the polychromatic centroid position as a function of the Zenith angle. The results for the on-axis field and the four corner fields are summarized

in figure 3.13. For the on-axis field, the maximum centroid movement is of the order of 0.5 μm in the full ZA range, while, for the corner fields, the movement is of the order of 10 μm. Anyway, we emphasize that, during a single exposure, the ZA change is much smaller than 65 deg leading to a negligible movement of the image centroid also for the off-axis fields.

ADC rotation law

To drive the ADC during observations, it is necessary to know the optimum rotation law as a function of the Zenith angle. The angle of rotation will depend on the atmospheric parameters, such as temperature and pressure, and also on the waveband of observation. For example, when using narrow-band filters, the atmospheric chromatic dispersion will be negligible.
The detailed characterization of the ADC rotation law will be done at the telescope during pre-commissioning. However, in order to understand the sensitivity to the different parameters, we calculated in Zemax a set of case studies representing the expected extreme conditions in which the ADC will be used:

- Standard conditions: $T = 0°$C, $P = 0.73\ atm$, waveband=0.95-1.7 μm
- Highest Temperature:$T = 20°$C, $P = 0.73\ atm$, waveband=0.95-1.7 μm
- Lowest Temperature: $T = -20°$C, $P = 0.73\ atm$, waveband=0.95-1.7 μm
- Highest Pressure: $T = 0°$C, $P = 0.80\ atm$, waveband=0.95-1.7 μm
- Lowest Pressure: $T = 0°$C, $P = 0.67\ atm$, waveband=0.95-1.7 μm
- Narrow-band HeI: $T = 0°$C, $P = 0.73\ atm$, waveband=1.08-1.1 μm
- Broad-band Y: $T = 0°$C, $P = 0.73\ atm$, waveband=0.95-1.1 μm
- Broad-band H: $T = 0°$C, $P = 0.73\ atm$, waveband=1.4-1.7 μm

The results appear in figure 3.14. The difference in the rotation is greater at high zenith angles, where the dispersion grows very quickly. As expected, for cold temperatures or high pressures, the atmospheric dispersion is greater and consequently the rotation angle of the ADC is closer to zero (maximum dispersion correction). The opposite happens for high temperatures or low pressures. The dependence on the waveband is less easy to understand, because it also depends on the dispersion characteristics of the glasses at different wavelengths. Anyway, the maximum spread between the different observing conditions is of the order of 15 deg for the ADC rotation angle, suggesting that the rotation law should be tuned on the atmospheric parameters, especially for high zenith angles.

ADC tolerance analysis

An analysis was dedicated specifically to identify the tolerance on the rotation of the ADC. In particular the questions we wanted to answer were: (1) what is the required update frequency for the ADC? (2) What is the maximum rotation speed? (3) what is the effect on the image quality and residual dispersion? The answer to these questions depends obviously on the observing conditions, such as the declination of the object, the time of observation, and the atmospheric parameters. For what concerns the atmospheric parameters, we put ourselves

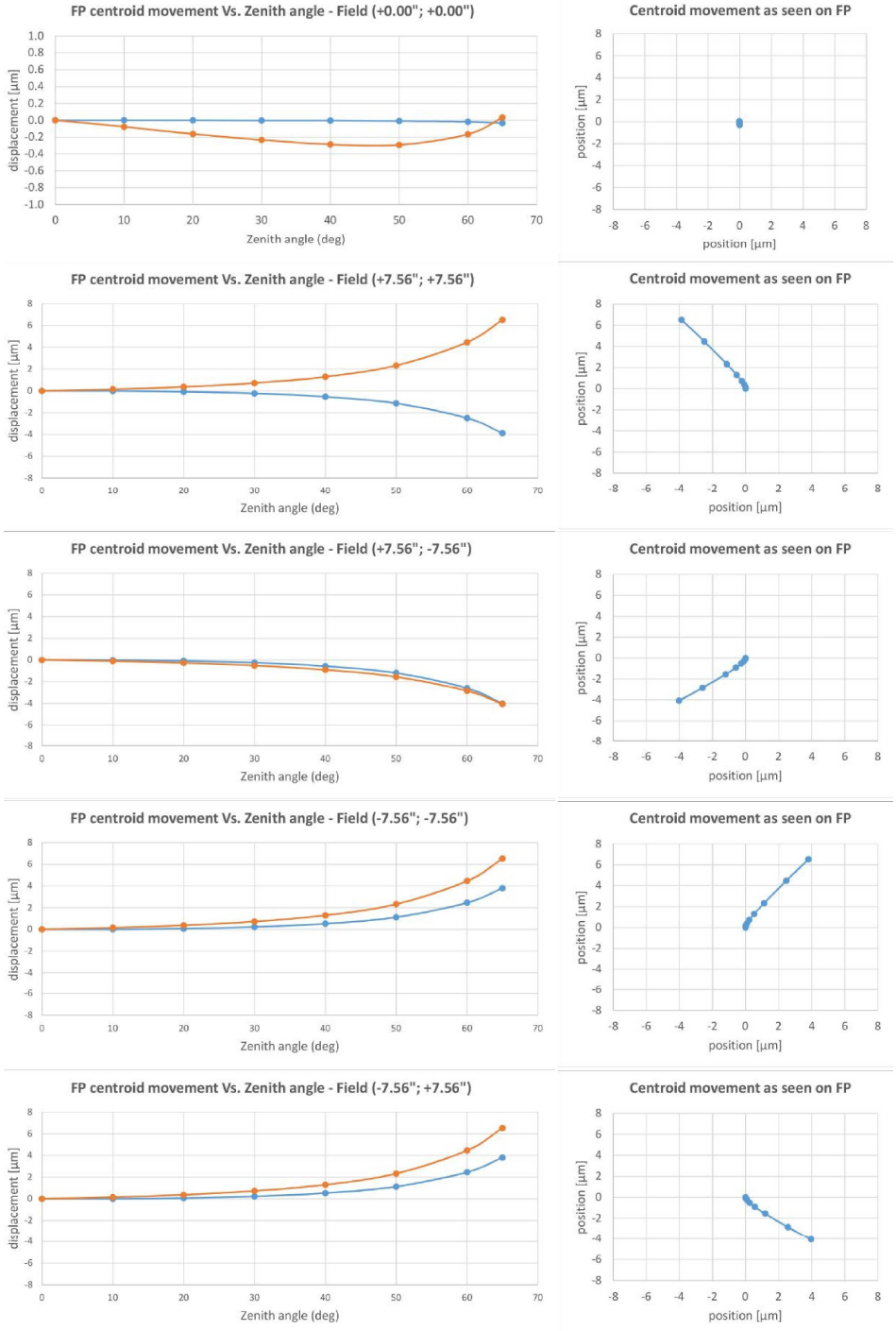

Figure 3.13: Polychromatic centroid movement due to ADC rotation. On the left is represented the displacement in the X (blue) and Y (orange) directions as a function of the zenith angle for the central field and the four corner fields. On the right is shown the centroid movement as seen on the focal plane

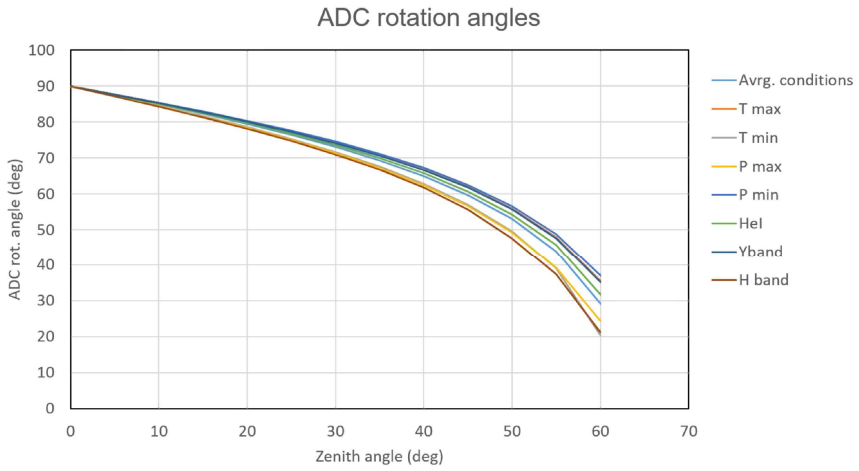

Figure 3.14: Best rotation angles of the ADC for different observing conditions.

in the average conditions described in the previous section. For the object parameters, we calculated which is the maximum rate of change of the Zenith angle for an object at the LBT. The Altitude as a function of the Hour Angle for different object declinations appears in figure 3.15. The maximum steepness is reached for objects on the celestial equator, when they are rising from the horizon. For these objects the rate of change of the ZA is 12 deg/hour.

These conditions correspond also to the region where the ADC rotation is faster, since we

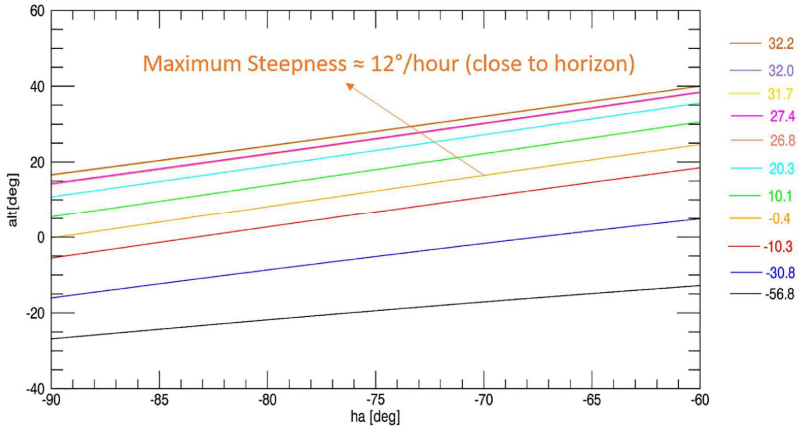

Figure 3.15: Altitude vs. hour angle at LBT for different declinations.

are very close to the horizon and the atmospheric dispersion increases very quickly. In the case of SHARK-NIR, the rotation rate of the ADC when observing an object at ZA=64 deg is equal to 7.4 deg of rotation for every deg of altitude. We can conclude that the maximum rotation rate of the ADC is:

$$v_{ADC-max} = 7.41 \cdot 12 = 89\ deg/hour\ =\ 1.5\ deg/min \tag{3.1}$$

This answers to question number (2) and the value is well within the maximum speed allowed by the ADC motorized stage. Moreover, this represent the worst condition possible, since observations will likely be performed close to the meridian.
To answer questions number (1) and (3), we made the assumption that the position of the ADC is updated every minute (although faster rotation is possible). This means that the maximum error on the ADC rotation is 1.5 deg. Feeding the number in Zemax we got a loss of 1% in strehl ratio due to the residual atmospheric dispersion and considering the full wavelength range of SHARK-NIR. The conclusion is that the ADC position can be updated with a 1 minute cadence with negligible losses in performance and that the tolerance on the rotation precision is within the error of common rotating stages.
As a further check, we considered the observational scenario of the Taurus-Auriga star forming region, close to the meridian. Considering an observation of 1 hour (from half an hour before the transit on the meridian to half an hour after), the zenith angle changes from ZA=10 deg to ZA=8 deg (see figure 3.16). Moreover, the atmospheric dispersion is very small, since we are close to zenith. In fact, inserting the parameters in Zemax and keeping the ADC fixed for all the observation, the PSF does not change significantly during the observation and the SR is always higher than 99%. We underline that the Taurus-Auriga SFR is very close to Zenith during the crossing of the meridian. This means that the field rotation is very fast, which is a very favorable condition to perform angular differential imaging.

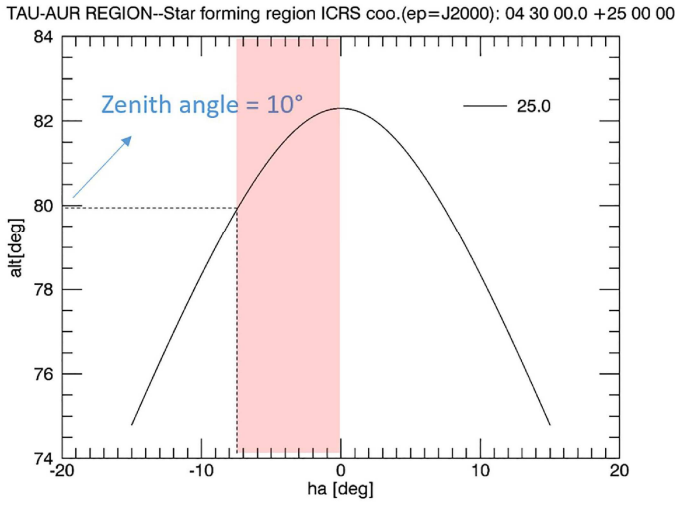

Figure 3.16: Altitude vs. hour angle for the Taurus-Auriga SFR close to the meridian.

3.4.4 Pupil re-imager

The pupil re-imager is an achromatic doublet that can be inserted between OAP-4 and the dewar window (figure 3.17) to make an image of the pupil on the scientific detector to be used for alignment of the pupil masks (Apodizer and Lyot stop) before observation. The lens is a 1" commercial achromatic doublet by Thorlabs. The focal length is $f = 300\ mm$ and it is optimized over the wavelength range $\lambda = 1050 - 1700\ nm$. The diameter of the pupil image is ≈ 11.8 mm and is sampled by the scientific camera with approximately 650 pixels.

The pupil re-imager could also be used, together with a $\pi/2$ phase mask on the intermediate

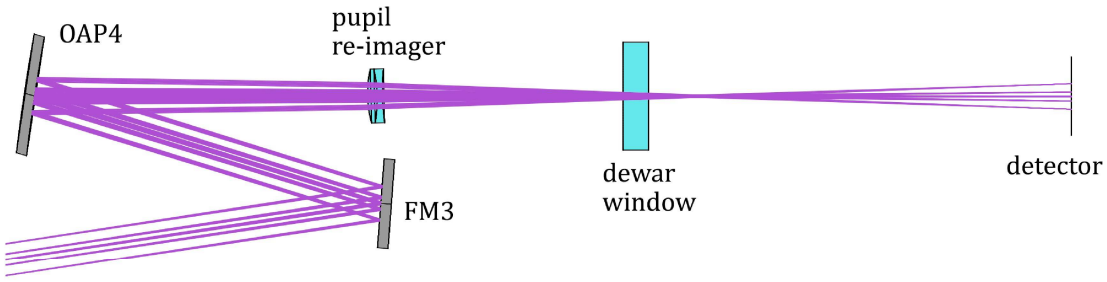

Figure 3.17: Optical layout of the deployable doublet used to re-image the pupil on the scientific detector.

FP, for low-order wavefront sensing, according to the Zernike phase mask concept described in N'Diaye et al. (2013) [56]. The working principle consists of using a $\pi/2$ phase mask in the intermediate FP to transform the phase aberrations of the wavefront into intensity variations in the following pupil plane that can be measured by the scientific detector. This technique could be a more efficient alternative to the proposed method for NCPA correction, based on applying random modes to the ASM until the SR is optimized. The drawback of the phase mask concept would be the use of a position in the intermediate focal plane filter wheel which is already entirely used for the occulting masks and the slits for the spectroscopic mode.

Pupil image quality

The image quality achieved for the pupil image is directly related to the centering precision that we want to obtain for the apodizing masks. The most sensitive mask has a centering tolerance of the order of $1/200^{th}$ of the pupil diameter, which corresponds to approximately 3 pixels on the science camera.
To evaluate the image quality of the pupil, we have considered the secondary mirror (M2) of the LBT as the object source. When the telescope is pointing to a star, the secondary mirror is ideally illuminated by a single field direction. This means that each point of M2 emits rays in a specific direction, i.e. the object cone angle is zero. However, the atmospheric turbulence spreads the rays into a cone angle (at the primary mirror of the telescope) given by the seeing condition of the night. To evaluate the pupil image quality, we constrained the system to trace rays coming only from these angles putting a field stop in the bent Gregorian FP of LBT. The field stop has an angular size of ± 0.5 arcsec (not very good seeing condition). Note that the AO module then corrects the rays direction. Thus the chosen value for the cone angle is a conservative estimate.
Figure 3.18shows the polychromatic spot diagram in the J broadband filter for different points in the pupil. The blue spot correspond to $\lambda = 1.159\mu m$ and the green spot to $\lambda = 1.356\mu m$. The plot on the left shows the spot diagram when observing at zenith, the plot on the right is the same spot diagram when observing at a zenith angle of 50 deg. It is clearly visible that the pupil image suffers from a chromatic lateral aberration generated by the ADC that increases with the zenith angle of observation. In fact, the ADC produces a chromatic dispersion opposite to the atmospheric one. Atmospheric dispersion by itself is not visible in a pupil

plane image since it only affects the angle of the rays but not their position on the pupil image. However, since the ADC is not placed in a pupil plane, it is correcting the angles of the rays in a plane far from the pupil. This translates into a chromatic dispersion on the following pupil planes that is dependent on the distance between the ADC and the pupil image. The maximum lateral chromatic shift in J band is of the order of 30 μm at ZA=65 deg, which corresponds to approximately 2 pixels. The aberration could be greatly reduced if observations will be performed with a narrowband filter. On the other hand, using a narrowband filter, the pupil will be illuminated by fewer photons and a trade-off is necessary depending also on the brightness of the target.

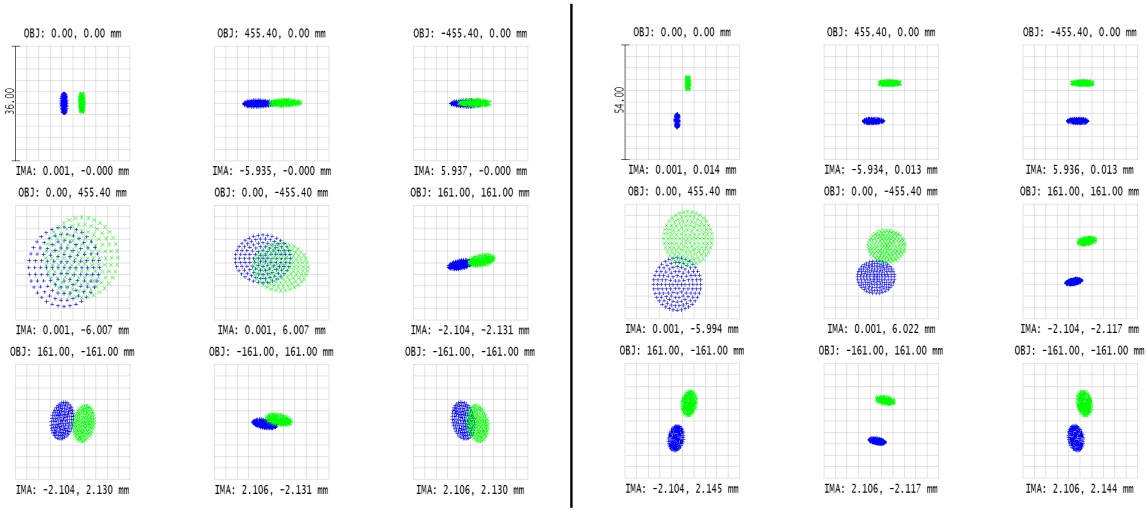

Figure 3.18: Spot diagram of the pupil image produced by the pupil reimager. Blue color corresponds to $\lambda = 1.159 \mu m$, green color corresponds to $\lambda = 1.356 \mu m$. Left: spot diagram at ZA=0 deg, The side of the box is 2 pixels. Right: spot diagram at ZA=50 deg. The side of the box is 3 pixels.

3.4.5 Tip-tilt wavefront sensor

The tip-tilt WFS module is shown in figure 3.19 and is made up of three components:

1. A beam splitter to send a small portion of the light $(5 - 10\%)$ to the WFS. The beam splitter is always inserted in the science channel.
2. An achromatic doublet to image the star on the WFS detector with proper sampling
3. A detector used to record the spot.

The detector selected for the design is the "Basler ace acA1300-60gm-NIR GigE Camera" produced by Basler. It is a CMOS sensor enhanced for the NIR. The specifications of the product are summarized in table 3.2.

The imaging lens is a commercially available achromatic doublet produced by Thorlabs. It is a Ø1" cemented doublet optimized for the wavelength range 1050-1620 nm. The focal length is 150 mm and it images a field of view of 10 x 13 arcsec on the detector with an F/13 focal ratio. The resulting plate scale is 10 mas/px and the spot is sampled with ≈ 20 pixel across

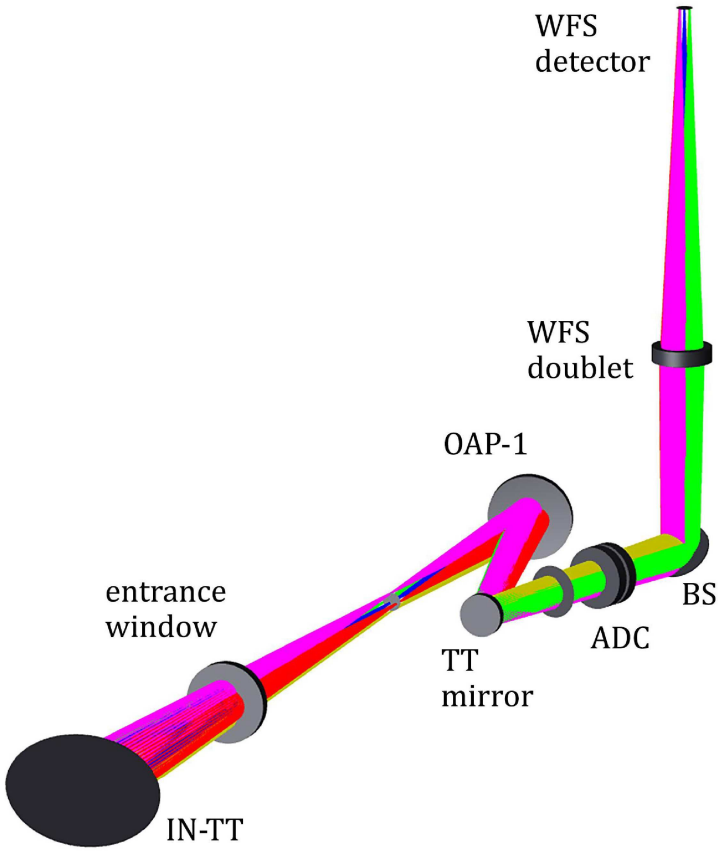

Figure 3.19: 3D shaded layout of the internal TT-sensor.

the diameter. Provided that we will be able to achieve a 0.5px precision in the determination of the spot centroid, this would correspond to a sensitivity of 5 mas on-sky. Some tests are on-going to assess the best procedure for the determination of the spot position.

3.4.6 Centering the pupil mask and occulting mask

To center the pupil of the telescope on the apodizers and the image of the star on the occulting mask, we can act on the two tip-tilt mirrors of SHARK: IN-TT and the internal TT mirror (see figure 3.6). A tilt of the IN-TT mirror will move both the pupil image and the image of the star because it is neither in a pupil plane nor in a focal plane. On the other hand, a tilt of the internal TT mirror will move only the image of the star. The best procedure to align both planes is to first move IN-TT to center the pupil on the mask and then, to use the internal TT mirror to center the star on the occulting mask (without moving the pupil).
To understand the precision needed to guide the two mirrors, we calculated their interaction matrices i.e. the movement produced by the mirror when it is tilted by a given angle. For what concerns the IN-TT mirror, there is a complication. In fact, the mirror is placed outside the de-rotator of SHARK-NIR. This means that the coupling between the x and y rotation axes of the mirror and the corresponding axes of the fundamental coronagraphic planes, will rotate together with the de-rotation angle. To account for this effect a rotation matrix R_{derot}

Parameter	Value
Sensor format	1/1.8”
Imaging device	e2v EV76C661
Type of sensor	Progressive Scan CMOS
Pixels	1280×1024 px
Pixel size	5.3×5.3 μm
Frame rate (fps)	60
Dimensions	54 x 29 x 29 mm

Table 3.2: Specifications of the “Basler ace acA1300-60gm-NIR GigE Camera”

should be applied to the interaction matrix. The interaction matrices have been calculated in Zemax and are:

- **Internal TT mirror - Image plane**

$$\begin{bmatrix}\theta_x\\ \theta_y\end{bmatrix}_{sky} = \begin{bmatrix}0 & 0.002626647\\ -0.002719305 & 0\end{bmatrix} \cdot \begin{bmatrix}\theta_x\\ \theta_y\end{bmatrix}_{TTmirr} = A \cdot \begin{bmatrix}\theta_x\\ \theta_y\end{bmatrix}_{TTmirr} \tag{3.2}$$

- **IN-TT - Image plane**

$$\begin{bmatrix}\theta_x\\ \theta_y\end{bmatrix}_{sky} = R \cdot \begin{bmatrix}0 & -0.00582395\\ 0.00459162 & 0\end{bmatrix} \cdot \begin{bmatrix}\theta_x\\ \theta_y\end{bmatrix}_{IN-TT} = R \cdot B \cdot \begin{bmatrix}\theta_x\\ \theta_y\end{bmatrix}_{IN-TT} \tag{3.3}$$

- **IN-TT - Lyot Stop**

$$\begin{bmatrix}d_x\\ d_y\end{bmatrix}_{Lyot} = R \cdot \begin{bmatrix}0 & 2.12931\\ -1.67876 & 0\end{bmatrix} \cdot \begin{bmatrix}\theta_x\\ \theta_y\end{bmatrix}_{IN-TT} = R \cdot C \cdot \begin{bmatrix}\theta_x\\ \theta_y\end{bmatrix}_{IN-TT} \tag{3.4}$$

where angles are in arcsec and lengths are in microns. Note that the interaction matrices have been denoted with the letters A, B and C to simplify the notation. The alignment procedure is as following:

1. Calculate movement of IN-TT to center the pupil on the mask:

$$\begin{bmatrix}\theta_x\\ \theta_y\end{bmatrix}_{IN-TT} = -(R \cdot C)^{-1} \cdot \begin{bmatrix}Ed_x\\ Ed_y\end{bmatrix}_{Lyot} \tag{3.5}$$

   where Ed_x and Ed_y are respectively the decenter of the pupil in the x and y direction with respect to the Lyot stop.

2. Calculate the shift of the image (which is the sum of the original decenter plus the one introduced by IN-TT):

$$\begin{bmatrix} E\theta_x \\ E\theta_y \end{bmatrix}_{sky} = \begin{bmatrix} E\theta_{x,0} \\ E\theta_{y,0} \end{bmatrix}_{sky} + R \cdot B \cdot \begin{bmatrix} \theta_x \\ \theta_y \end{bmatrix}_{IN-TT} \tag{3.6}$$

3. Calculate movement of the internal TT mirror to compensate for image decenter:

$$\begin{bmatrix} \theta_x \\ \theta_y \end{bmatrix}_{TTmirr} = -(A)^{-1} \cdot \begin{bmatrix} E\theta_x \\ E\theta_y \end{bmatrix}_{sky} \tag{3.7}$$

Of course, iteration of the above procedure will lead to more accurate results. Moreover, the real interaction matrices will need to be calculated at the telescope during pre-commissioning of the instrument.
From the interaction matrices, it is also possible to estimate the precision with which the mirrors need to be moved in order to correct misalignment of the masks. So, for example, if the centering of the star on the occulting mask should achieve a precision of 3 mas, the corresponding tilt of the internal TT mirror is of the order of 1 arcsec. In the same way, for the pupil, a movement of $1/200^{th}$ of the diameter of the Lyot stop ($\sim 150\ \mu m$) is produced by a tilt of IN-TT of ≈ 35 arcsec. To achieve these accuracies, both mirrors are drived, in closed loop, by piezo actuators acting on a gimbal mount.

3.5 Tolerance analysis

The tolerance analysis for SHARK-NIR is divided in two parts. The first analysis, conducted for the Conceptual Design Phase, consists in a sensitivity analysis to misalignment of optical components. The second analysis, prepared for the Final Design Phase, is devoted to the estimation of preliminary manufacturing tolerances for the optics.
The alignment procedure for SHARK-NIR is not completely defined yet. Once it is defined, it will be possible to detail the tolerance analysis in a more accurate way, using the proper compensators and following the alignment procedure. Nevertheless, the results presented in the following section have been useful for a first definition of the requirements of optics, mountings and motors to be used for SHARK-NIR.

3.5.1 Alignment sensitivity analysis

In order to assess the system sensitivity to misalignment of optical components we performed a preliminary tolerance analysis on the science channel, based on Monte Carlo simulations. For the analysis, we proceeded in the following way:

- We considered sensitivity to defocus, decenter x, y and tilt x, y, and z (clocking error) for every optical component (not single surfaces)
- We allowed compensation moving the scientific detector in decenter and defocus
- The adopted image quality criterions were RMS wavefront error + field centering on the detector (Boresight error)

- We performed 10000 Montecarlo simulations moving each optical component by a random quantity between a minimum and maximum allowed range and looked at the results
- We adjusted the minimum and maximum values, tightening the specification for the most sensitive components and iterating the process until we reached a reasonable performance degradation.

The definition of movements is sketched in figure 3.20: x and y decenter movements are defined along the plane of the optical surface, defocus is parallel to the normal at the surface center. Tilt x, y and z are respectively rotations around the x, y and z axes passing through the center of the optical elements. The results of the tolerance analysis are summarized in table

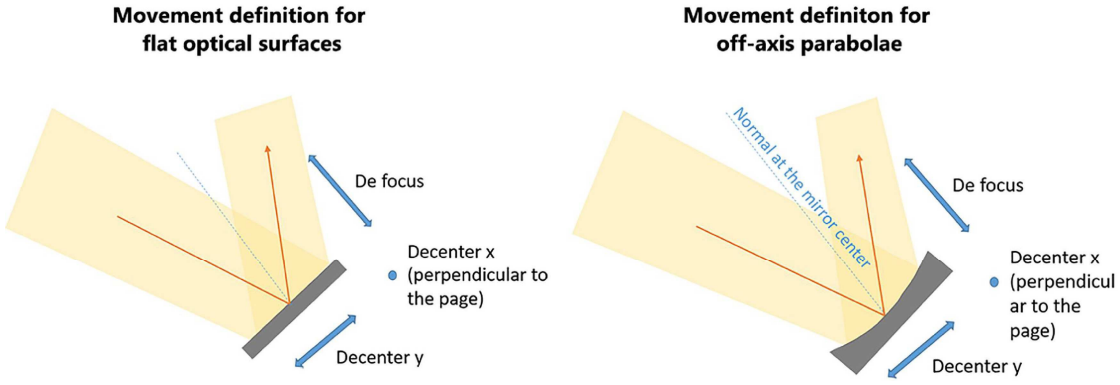

Figure 3.20: Definition of movements used in the sensitivity analysis for flat optical elements (left) and for off-axis parabolic mirrors (right).

3.3, which lists the estimated maximum amount of misalignment for each optical element. In general, the system is quite tolerant to misalignment and typical values of movement are between 100 and 200 μm for decenter/defocus and 1 – 3 arcmin for tilt. However, some considerations should be kept in mind:

- The tolerances are computed looking only at the optical quality and boresight error on the scientific FP. Of course, for some elements, requirements are driven by other criteria (i.e. Coronagraphic performance, position of pupil image on detector, tolerances for the local tip-tilt WFS, etc.)
- The only compensation used is the position of the detector. For this reason, tilt tolerances are quite tight in some cases. A tilt of 0.02 deg for a surface of 12 mm diameter means a movement of $\sim 2\mu m$ at the edge of that element. Probably the numbers can be relaxed if necessary, but a more detailed simulation is needed.
- The numbers provided in the table are the positioning precision required during alignment and not position stability (which we expect to be tighter).
- Some of the parameters are completely irrelevant for the final optical quality (for instance the tilt z of flat mirrors). For these specifications a quite big tolerance value is provided (of the order of 1mm or 1 deg), and the only real requirement is not to vignette the scientific beam.

	Defocus [mm]	**Decenter x [mm]**	**Decenter y [mm]**	**Tilt x [deg]**	**Tilt y [deg]**	**Tilt z [deg]**
OAP1	±0.2	±0.2	±0.1	±0.05	±0.05	±0.5
TT mirror	±1.0	±1.0	±1.0	±0.02	±0.02	±2.0
ADC1	±1.0	±1.0	±1.0	±0.2	±0.2	±0.1
ADC2	±1.0	±1.0	±1.0	±0.2	±0.2	±0.1
BS	±1.0	±1.0	±1.0	±0.2	±0.2	±0.2
OAP2	±0.2	±0.2	±0.2	±0.05	±0.05	±0.05
Fold1	±1.0	±1.0	±0.2	±0.2	±0.2	±2.0
OAP3	±0.2	±0.2	±0.1	±0.05	±0.05	±0.5
Fold2	±1.0	±1.0	±0.2	±0.03	±0.03	±2.0
Fold3	±1.0	±1.0	±0.2	±0.03	±0.03	±2.0
OAP4	±0.2	±0.2	±1.0	±0.05	±0.05	±0.5
Window	±1.0	±1.0	±1.0	±2.0	±2.0	±2.0

Table 3.3: Tolerances for each optical element estimated from the sensitivity analysis.

Figure 3.21 shows the comparison between the SR map of the nominal design (left) and the SR map obtained in the worst case Monte Carlo simulation (right). The color scale is the same for both pictures and the estimated performance degradation is around $2-3\%$ in terms of SR.

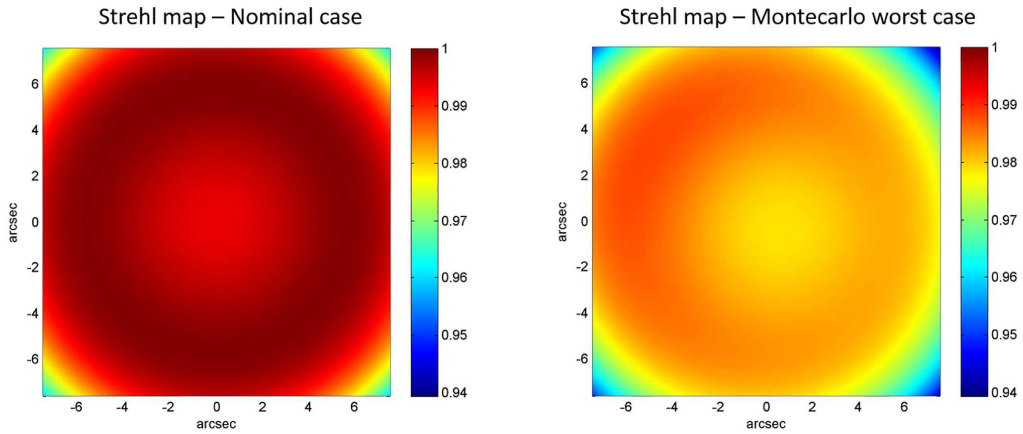

Figure 3.21: Strehl ratio maps of the nominal optical design (left) and of the Montecarlo simulation worst case (right).

3.5.2 Manufacturing tolerances

The manufacturing tolerances determine the precision with which the optical elements must be produced to satisfy the instrument requirements. In our analysis, we considered a tolerance for the following parameters:

- Radius of curvature: we considered an error of $\pm 0.1\%$ for the radius of curvature of the OAP mirrors.

- Flatness: it is the deviation from a perfect planar surface, usually measured in fringes. We simulated deviation from perfect flatness by applying a curvature to flat surfaces that results in 0.5 fringes of deviation.

- Wedge: it consists in the non-perfect parallelism between two surfaces of the same optical element. We considered it to be ± 2.5 arcsec for every face of filters/windows.

- Figure error: i.e. the deviation of the optical surface from the nominal shape. We simulated it by applying low order Zernike terms to the OAP mirrors. As input aberrations, we used astigmatism, coma, trefoil and spherical with a total amplitude of $\lambda/20$ rms per mirror.

We ran 1000 Monte Carlo simulations, allowing the system to compensate focus error by moving the detector along the optical axis. The re-focusing was the only compensator used for the re-optimization of the system.
The rms wavefront error map of the full FoV for the worst-case Monte Carlo system is represented in figure 3.22. The average wavefront error is $\approx 50\ nm$ rms. The most critical parameters, are the figure errors of the OAP mirrors and the flatness of the dichroic and IN-TT mirror. If the wavefront error is static within an observation, in principle it is possible

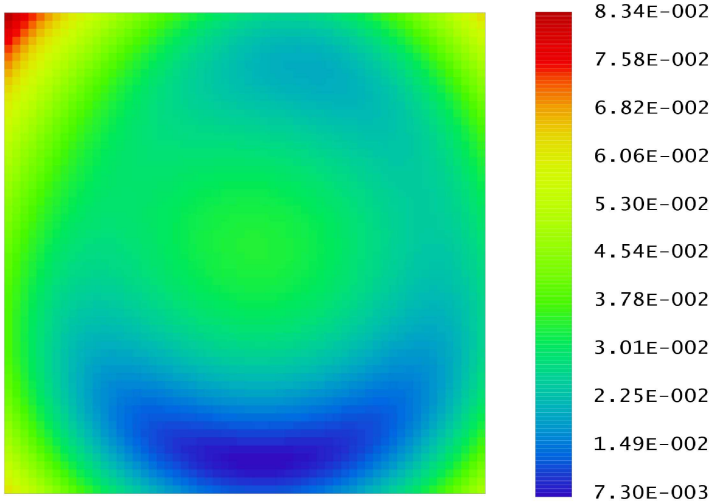

Figure 3.22: RMS wavefront error map of the worst Montecarlo system. Units are waves.

to recover it by correcting the non-common path aberrations with the adaptive secondary mirror of LBT, giving an offset to the wavefront measured by the AO system of the telescope. However, the amplitude of the NCPAs should not be too high. Otherwise, they will affect the performance of the AO Wavefront sensor. For this reason, it is mandatory to limit the figure error to about 30 nm rms for each mirror. For what concerns the high spatial frequency surface error, i.e. in the regime of micro-roughness, a separate analysis is provided later.

3.6 Dual band imaging

Dual band imaging (DBI) consists in producing two simultaneous images of the same target on the science camera. Each image passes through a different passband filter so that two colors are recorded at the same time. Dual band images can be used to perform spectral differential imaging in a very efficient way. Spectral differential imaging is a differential imaging technique for increasing the contrast of an image, taking advantage of the different spectral emission of two nearby sources (see [57], [58]). In general, one of the filters coincides with a strong absorption band and the other to the continuum just outside the absorption band. So, for example, when observing a planet characterized by strong methane absorption, it will be very faint in the methane filter and it will be brighter in the continuum filter. Making the difference between the two images will subtract most of the speckles originating from residual aberrations and will keep the light from the planet.
SDI is a standard observing mode in current high contrast imaging instruments (SPHERE and GPI) and has been successfully applied on sky e.g. for the study of debris disks (see [59]). Based on the above considerations, a possible implementation of DBI has been studied for SHARK-NIR. To use DBI in coronagraphic mode, the splitting of the two images should be performed in the second pupil plane, after the occulting mask. The separation is provided by a Wollaston prism, a device that exploits the birefringence of some materials to angularly separate the "s" and "p" polarization states of the incoming unpolarized radiation. The angle of divergence ($\delta_o + \delta_e$ in figure 3.23) between the two beams is determined by the birefringence of the material, the prism wedge angle and the wavelength of the light. Figure

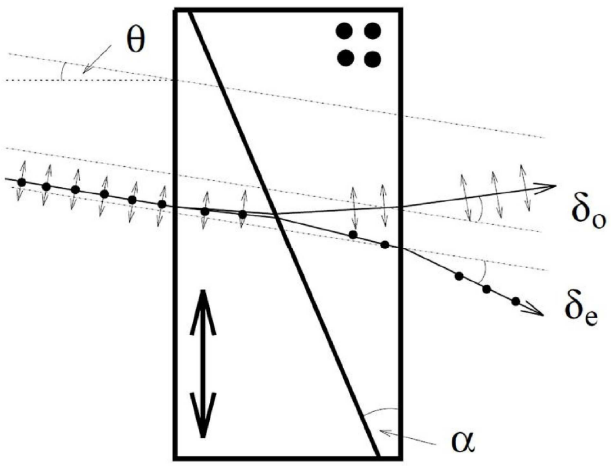

Figure 3.23: Schematic representation of a Wollaston prism and ray-tracing (adapted from Fig. 11 of Bennet 1995)

3.23 is a sketch of a Wollaston prism with schematic ray-tracing. In the first (entrance) prism the "o" (ordinary) light beam vibrating perpendicular to the optic axis has a refractive index n_o while the "e" (extraordinary) ray has a refractive index n_e. At the prisms interface, the refractive index of the "o" ray changes from n_o to n_e and the opposite occurs for the "e" ray, and when exiting the second prism the angle between the two rays is increased further. For most practical applications, the deviation δ can be considered symmetric around θ (i.e.

$\delta_o \approx -\delta_e$) and the separation between the o and e rays is given by [60]:

$$\delta = \frac{\delta_o - \delta_e}{2} \approx \Delta n \cdot \tan(\alpha) \tag{3.8}$$

where $\Delta n = n_e - n_o$ is the birefringence index of the crystal. The deviation δ is chromatic because Δn varies with λ. This means that broadband images seen through a Wollaston prism are elongated. The amount of lateral chromatism over a given wavelength range $\lambda_1 < \lambda_2 < \lambda_3$ follows from equation 3.8 and can be quantified by the parameter:

$$V = \frac{\Delta n(\lambda_2)}{\Delta n(\lambda_1) - \Delta n(\lambda_3)}, \tag{3.9}$$

as proposed in [60]. The image elongation is then given by:

$$\epsilon = \frac{\delta}{V} \tag{3.10}$$

In the case of SHARK-NIR, the deviation angle produced by the prism is limited by the following constraints:

1. **maximum deviation**: the maximum deviation plus the single image FoV should be smaller than the total FoV of the instrument. Considering a FoV of 18 arcsec and a single image FoV of 2 arcsec, the on-sky separation should be equal to 16 arcsec which corresponds to an angle at the second pupil plane equal to $\delta_{max} = 16 \cdot D_{tel}/D_{pup} = 2.4\ deg$.

2. **minimum deviation**: in order to apply different filters to the two images, the "s" and "p" polarized beams should be spatially separated. Very close to the image plane, the minimum separation that prevents the overlapping of the beams is of the order of half the instrument FoV. However, placing the dual-band filters just before the focal plane means that they will be inside the cryostat, adding a lot of complications to the design of the dewar and the control of the motors for the cryogenic filter wheel. Fortunately, limiting the FoV to 2 arcsec for the DBI mode, it is still possible to place the dual-band filters outside the cryostat, just before the dewar window. With this arrangement, the minimum deviation allowed is $\delta_{min} = 1.5\ deg$.

For the choice of the material of the prism, the best solution is to use crystals with a good transmittance in the NIR and with low lateral chromatic aberration. The birefringence index and V parameter of some IR birefringent crystals is provided in [60]. The most commonly used material for Wollaston prisms is calcite, which has a quite high birefringence index ($\Delta n = 0.155$ in H band) but also a non-negligible chromatic dispersion ($V_H = 36$). Other possible materials which are now produced by several companies are MgF_2 and YVO_4. MgF_2 has a smaller birefringence ($\Delta_n = 0.011$) which requires bigger angles of the prism to achieve the same deviation, while the birefringence of YVO_4 is similar to that of Calcite ($\Delta n = 0.203$). For what concerns lateral color, and assuming observations with narrowband filters with a bandwidth of $\Delta\lambda = 50nm$, the on-sky projected elongation in H band calculated with equation 3.10 is:

- $\epsilon = 58\ mas$ for Calcite;

- $\epsilon = 22\ mas$ for MgF_2;
- $\epsilon = 13\ mas$ for YVO_4.

Given the good performances, we selected $YVO-4$ as the baseline material for the Wollaston prism and we already found a company able to produce it.
To check the calculations and the design parameters, we produced a ray-tracing model of the prism using the "birefringent" surface type provided by Zemax. To define the birefringent surface, it is necessary to provide the orientation of the axis of the crystal, which defines the axis of symmetry of the material, and the refractive index for the ordinary and extraordinary ray.
Figure 3.24 shows the optical layout of SHARK-NIR with the Wollaston prism inserted.

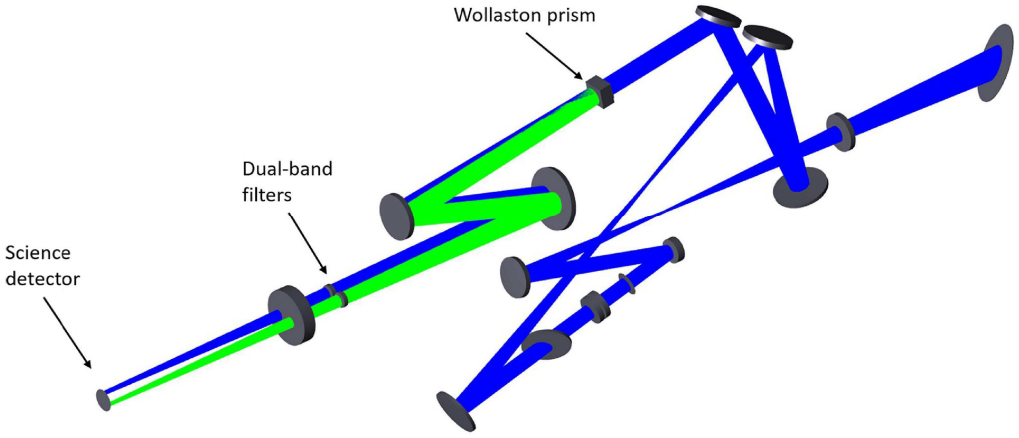

Figure 3.24: 3D optical layout of the DBI mode of SHARK-NIR.

The two colors denote the two different beams exiting the prism and corresponding to the "s" and "p" polarization states. The prism is made of YVO_4 and has an apex angle of $\alpha = 5.2$ deg. The beam deviation at $\lambda = 1.5\mu m$ is $\delta = 2.1$ deg, corresponding to an angle of approximately 14 arcsec on sky. Placing the dual-band filter 44 mm before the cryostat window and accounting for a radial FoV of 1 arcsec, the separation of the beams is 5.9 mm (figure 3.25, left), leaving a bit of margin with respect to the clear aperture of the filters.
Depending on the volume available, the filters can be inserted in the optical beam by a linear stage or by a filter wheel. With the filter wheel option, at least 3 pairs of filters can be accommodated, giving a lot of flexibility to DBI observations. Currently, the company that is doing the mechanical design study of SHARK-NIR is evaluating if it is possible to accommodate a custom filter wheel for the DBI mode. The dual-band filters currently selected for SHARK are summarized in the right of figure 3.25.

3.7 Thermal background

For an instrument working in the infrared, it is extremely important to evaluate the thermal emission from the environment. This is particularly true for SHARK-NIR in which most of

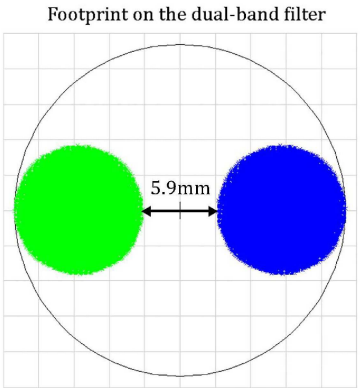

Dual-band filters

Filter	λ_c [nm]	$\Delta\lambda$ [nm]
H2-H3	1588.8 – 1667.1	TBD
Cont J – Pa β	1215.7 – 1281.3	18.3 – 20.9
Cont H – Fe II	1557.8 – 1645.5	24.1 – 26.1

Figure 3.25: Left: footprint diagram of the "s" and "p" polarized beams on the dual-band filter. Right: list of dual-band filters foreseen for SHARK-NIR.

the optical train is at ambient temperature and only the detector is cooled to the temperature of liquid nitrogen. The thermal emission is produced both by structural elements (spider, mountings, etc..) and by optical elements. The purpose of our calculations is to estimate the number of photons/s/px coming from thermal emission in order to: (1) constrain the length of the cold baffle in front of the detector, (2) estimate the upper cut-off wavelength (3) identify possible critical aspects in the design.
The requirement on the maximum acceptable thermal noise comes from S/N ratio estimations: considering a typical detector integration time (DIT) of 60 s, the estimated thermal noise (Th_{noise}) can be computed as $(Th_{noise} \cdot 60)^{1/2}$, to be kept below the detector expected readout noise, which is $< 15\ e^-/pix/readout$ (information taken from Teledyne technical specification). This comparison leads to a reasonable acceptable number of 4 to 5 photons per pixel per second.
In SHARK-NIR, we can limit the thermal background through a low-pass interference filter placed in front of the science detector. The filter will be characterized by a cut-off wavelength and by a cut-off efficiency which is defined as the fraction of photons (with $\lambda > \lambda_{cut-off}$) that are not blocked by the filter. Typical achievable efficiencies are of the order of $10^{-4} - 10^{-5}$. Moreover, a Narcissus mirror is placed in front of the dewar window to limit the solid angle through which the detector sees the external environment. The Narcissus mirror is coated with gold, characterized by a very low emissivity in the NIR.
To calculate thermal emission, we assumed the elements to emit like a perfect black-body:

$$BB_i(\lambda, T) = \frac{5.99584 \cdot 10^{22}}{\lambda^4} \frac{1}{\exp \frac{14387.9}{\lambda T} - 1} \qquad \left[\frac{ph}{s\ cm^2\ sr\ \mu m}\right] \tag{3.11}$$

where the index i denotes the i-th emitting element and the constants are valid for the adopted measurement units. Equation 3.11 gives the spectral irradiance of the black body. To get the photon flux on the detector it is necessary to multiply the irradiance by the étendue of the optical system and integrate it over the whole spectral range. In addition to this, the emissivity ϵ of the body and the throughput of the system should alsobe considered. Accounting for all these aspects, the thermal background is given by:

$$Th_{noise} = \sum_{i=1}^{n} \int BB_i(\lambda, T) \cdot A \cdot \Omega \cdot \epsilon_i \cdot \eta_i \cdot \eta_{filt}(\lambda) \cdot QE(\lambda)\ d\lambda \tag{3.12}$$

where the sum is done over all the optical elements, $A\Omega$ is the étendue, ϵ_i is the emissivity of the i-th element, η_i is the throughput of the system after the i-th element, η_{filt} is the throughput of the interferential filter and QE is the quantum efficiency of the detector.
To compute the expected thermal background for different parameter configurations, we used two different approaches:

- The first (pessimistic) estimation has been obtained assuming that the free solid angle allowed by the Narcissus mirror emits like a black body at the given temperature, with efficiency equal to 1. The assumed emissivity for the Narcissus mirror is 0.01, while the inner part of the cryostat is emitting at -80°C, with efficiency 1. The same computation has been repeated for different temperatures, combinations of interference filter efficiency, and detector response cut-off wavelength (λ_{cut-QE}), at which $QE < 50\%$.
- The second approach we followed to estimate the thermal background includes assumptions on the thermal emission of each optical element (as seen by the detector through all the subsequent optics). Basically, the contribution of each component is computed as a black body at 0°C, with an efficiency computed as 1-R (where R is the reflectivity) for the mirrors and T (transmissivity) for the refractive elements, considering the subtended solid angle and damped by the efficiencies of the optics positioned after the considered component. This can be considered as an optimistic estimation, since it considers only the thermal emission of optical elements.

3.7.1 Pessimistic thermal background estimation

For the pessimistic estimation of the thermal background we considered a dewar window of 2" diameter. The Narcissus mirror is placed 43mm before the window and has a hole of 43mm diameter to transmit the science FoV. The transmission profile of the interference filter is modelled as a step function equal to 1 for $\lambda < \lambda_{cut-off}$ and equal to the filter efficiency for $\lambda > \lambda cut - off$ (see figure 3.26, left). The detector QE is modelled by the following profile function (figure 3.26, right):

$$\begin{aligned} QE(\lambda) =& 0.8 \cdot e^{-\left(\frac{\lambda}{\lambda_{cut-QE}}\right)^{60}} && if \ \left(\frac{\lambda}{\lambda_{cut-QE}}\right)^{60} < 60 \\ QE(\lambda) =& 0 && if \ \left(\frac{\lambda}{\lambda_{cut-QE}}\right)^{60} > 60 \end{aligned} \tag{3.13}$$

Where λ_{cut-QE} is the wavelength at which the $QE = 50\%$.
The thermal background has been evaluated for temperatures of -10°C, 0°C and $+10$°C, cut-off wavelengths between 1.60 μm and 1.75 μm and detector QE cut-off of $\lambda_{cut-QE} = 2.5$ μm and $\lambda_{cut-QE} = 2.7$ μm. For all the cases, the thermal noise comes from inside the Narcissus mirror where $\epsilon = 1$, while the noise coming from the Narcissus and the cryostat is orders of magnitude smaller. The results are summarized in table 3.27. Basically, except for a case study in which the interference filter efficiency is 10^{-4} and, at the same time, the detector QE cut-off occurs at 2.7 μm, a scientific wavelength cutoff at 1.7 μm would keep the thermal background below the 5 ph/s/px required.

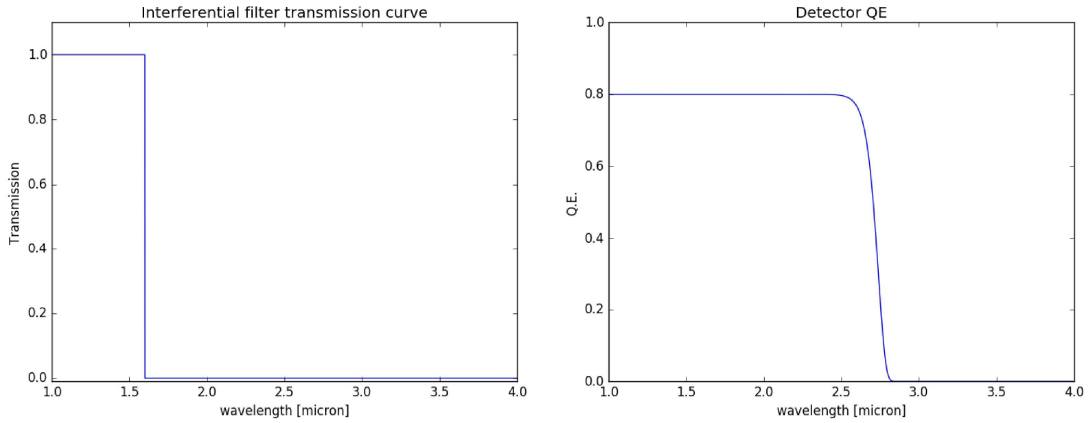

Figure 3.26: Left: transmission efficiency profile assumed for the interference filter. Right: QE curve assumed for the science detector.

3.7.2 Thermal background from optical elements

For the estimation of thermal background coming from optical elements, we made assumptions of the emissivity and temperature of each component. For the temperature we considered two case studies: one at $T = 0°\text{C}$ and one at $T = +10°\text{C}$. For the emissivity, we considered it to be equal to 1-R, where R is the reflectivity of the mirror (or transmission for refractive elements). The values assumed in the simulation are:

- LBT mirrors emissivity: 0.15 for M1, 0.1 for M2 and M3
- SHARK-NIR mirrors emissivity: 0.01
- SHARK-NIR refractive elements emissivity: 0.05
- Apodizing mask emissivity: 0.5

The étendue is the same for every optical element, since the quantity is conserved throughout the optical system. Since we are interested in the photons per pixel reaching the detector, we used the area of a single pixel to calculate the étendue:

$$A \cdot \Omega \approx A_{pix}/F_{\#}^2 = 2.66 \cdot 10^{-9} \quad [sr \cdot cm^2] \tag{3.14}$$

The efficiency of the interference filter has been assumed to be 10^{-4} with a cut-off wavelength of $\lambda_{cut-off} = 1.7\ \mu m$. The detector QE has a 50% QE cut-off at $\lambda_{cut-QE} = 2.5\ \mu m$.
The resulting total optics thermal background is 0.05 ph/s/px for $T = 0°\text{C}$ an 0.14 ph/s/px for $T = +10°\text{C}$. Of course, in this case, the expected thermal background is lower than for the conservative case, for two main reasons:

- the total system throughput is considered and is 0.23 (e.g. note apodizing mask throughput is 0.5), without the detector.
- the solid angle resulting for the incoming $F/_{\#}$ is $\sim$ 30 times lower than the angle subtended by the hole in the Narcissus mirror.

Of course, this estimation is strongly dependent on many assumptions, as described above.

Temperature [°C]	$\lambda_{cut\text{-}off}$ [µm]	Background [ph/px/s]			
		$E_{IF} = 10^{-4}$, $\lambda_{cut\_QE} = 2.5\mu m$	$E_{IF} = 10^{-5}$, $\lambda_{cut\_QE} = 2.5\mu m$	$E_{IF} = 10^{-4}$, $\lambda_{cut\_QE} = 2.7\mu m$	$E_{IF} = 10^{-5}$, $\lambda_{cut\_QE} = 2.7\mu m$
-10	1.60	0.6	0.1	2.2	0.26
-10	1.65	0.6	0.17	2.3	0.34
-10	1.70	0.8	0.36	2.5	0.52
-10	1.75	1.2	0.77	2.9	0.94
0	1.60	1.4	0.28	4.9	0.64
0	1.65	1.6	0.54	5.1	0.89
0	1.70	2.2	1.1	5.7	1.49
0	1.75	3.5	2.5	7.1	2.82
10	1.60	3.1	0.81	10.2	1.52
10	1.65	3.4	1.62	11	2.33
10	1.70	5	3.44	12.9	4.15
10	1.75	8.4	7.32	16.7	8.03

Figure 3.27: Estimated thermal background (for the pessimistic case) varying the working temperature and the wavelength

3.8 Sky background

On top of read-out noise and thermal noise, the noise arising from sky background should also be considered. The surface brightness of the sky can vary a lot from night to night and even within the same night due to airglow emission from the atmosphere. The variation is particularly strong in the H band while it becomes smaller at shorter wavelengths [61]. To evaluate the sky background for SHARK-NIR, we used the night sky spectrum provided by Patat [62], visible in figure 3.28. The spectrum is a combination of an optical spectrum obtained at Paranal with FORS1 and a synthetic NIR spectrum from the Gemini Exposure Time Calculator. Integrating the spectrum over the spectral range covered by SHARK and taking into account the throughput and the other parameters of the instrument, the resulting irradiance is equal to $F_{sky} = 9.7\ ph/s/px$. Of course, the sky background will be fainter when filters are used.

3.9 Impact of micro-roughness and contamination

3.9.1 Simulation strategy

In a high-contrast imager like SHARK-NIR, the light scattered by micro-roughness or dust contamination of optical surfaces can have a non-negligible impact on the performance. Evaluating scattered light is not an easy task in such a complex instrument, and a non-sequential ray-trace simulation like the one performed for JANUS would be extremely time consuming. In fact, even if we limit the analysis to on-axis stray-light generated by the central star, the number of optical surfaces is extremely high and the scattering direction would need to be accurately constrained for every surface, in order to provide good statistics of rays reaching

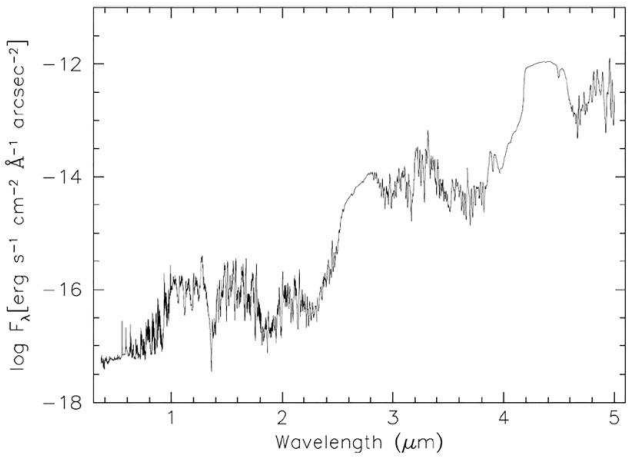

Figure 3.28: Night sky spectrum used for the estimation of the sky background (taken from Patat - 2006 [62])

the detector. Moreover, such an approach would be prone to error and would require a careful check of every input parameter of the scattering surfaces. For these reasons, we decided to use an analytical model instead of a ray-tracing one. In particular, we based our calculations on the model provided by Peterson (2004) [22]. This is the same model that we used to check the results of the stray-light analysis of JANUS and that showed good agreement with the ray-tracing results (see figures 2.28 and 2.29). There are a number of reasons that make the Peterson model very appealing for the stray-light analysis of SHARK-NIR:

- The model is valid for in-field sources of stray-light. In SHARK-NIR, the brightest source is by far perfectly on-axis.
- It is based on the 3-Parameter Harvey model for the BSDF, which can model both scattering from micro-roughness and scattering from particulate contamination.
- It provides the stray-light irradiance on the detector as a function of the radial distance from the source. Thus, the results can be integrated very easily into the detection curves coming from coronagraphic simulations (see figure 1.13).
- The simulation is very fast
- The input parameters can be changed easily, allowing us to simulate different case studies in a straightforward way. For instance, it is possible to change micro-roughness of some elements, or the amount of particulate contamination to understand the sensitivity to different input parameters

The stray-light irradiance as a function of the radial distance r from the image on the detector is given by (see also paragraph 2.11.1):

$$E_{SL,j} = \pi T (na)^2 \frac{a_{ent}^2}{a_j^2} b_0 \left[1 + \left(\frac{(na) r}{l \; a_j} \right)^2 \right]^{s/2} E_{ent} \tag{3.15}$$

where T is the instrument transmission, $na = 0.016$ is the numerical aperture of the system, $a_{ent} = 8220\ mm$ is the beam diameter at the entrance, a_j is the beam diameter at the j-th element, b_0, l and s are the three parameters of the Harvey model and E_{ent} is the irradiance from the source at the entrance of the instrument.
In the case of micro-roughness, the Harvey parameters have been calculated as described in Fest (2013) [3]. We used a slope of the BSDF $s = -1.8$ and a roll-off angle $l = 0.01 rad$. The b_0 parameter has been scaled to provide the proper amount of total integrated scatter. We considered a micro-roughness of 2nm rms for mirrors inside SHARK-NIR, 1nm rms for refractive surfaces and 10nm rms for the primary, secondary and tertiary mirrors of LBT.
In the case of particulate contamination, we used different Harvey models for the optics integrated in clean-room environments and those exposed to the ambient environment as suggested in [3]. The models are obtained from a fit to the BSDF obtained through a Mie scattering simulation.
For the optical surfaces exposed to ambient environment, i.e. the telescope, the dichroic, IN-TT mirror and the entrance window of SHARK, we used a Harvey profile with slope $s = -1.75$ and roll-off angle $l = 0.0035$. In the case of a contamination equal to PAC=250 ppm, the parameter $b_0 = 0.562$; for different levels of contamination, the b_0 parameter needs to be scaled by the ratio between the surface PAC and the one of the input model.
In the case of optics assembled in a clean-room environment, we used a double Harvey profile. For contamination equal to PAC=250 ppm, the Harvey parameters are: $s_1 = -2.7$, $l_1 = 0.001$, $b_{0,1} = 32.4$ and $s_2 = -0.5$, $l_2 = 0.1$, $b_{0,2} = 5 \cdot 10^{-5}$.
The total amount of particulate contamination is a very difficult parameter to estimate. For the external optical surfaces, we adopted a conservative value of PAC=23700 ppm ($\sim 2\%$ obscuration factor) that, according to Dittman (2002) [63], is a reasonable limit beyond which the Harvey model is not accurate anymore. For the clean-room optics, we estimated the contamination from the ISO class of the clean-room and the time required for the AIV procedure as described in [3]. Assuming a clean-room ISO class of 4, an integration period of 300 days, and a vertical orientation of the surfaces, we get a PAC=1778 ppm. Actually, the ISO class that we foresee to use for SHARK-NIR integration is 3, but we decided to use the conservative value of 4, to also account for contamination coming from the operators inside the room.
Since most of the star-light is blocked by the occulting mask, the optical elements placed after the mask do not contribute significantly to stray-light and we neglect them in the analysis.

3.9.2 Results

Figure 3.29 (left) shows the stray-light irradiance profile generated by micro-roughness (red) and particulate contamination (black). The y axis is logarithmic and data have been normalized by the irradiance of the source so that they can be compared to contrast curves. Here, we made the assumption that 100% of the energy of the star is sampled by 2x2 pixels (Nyquist hypothesis) so the source irradiance is defined as the source power divided by 4. The same will also happen for the light from a planet. With these working assumptions, the stray-light generated by PAC is about 100 times higher than that from micro-roughness. The total stray-light irradiance at 300 mas from the star is $\sim 10^{-5}$ and is comparable to the expected contrast ratio achievable in extremely good observing conditions. An example is provided on the right of figure 3.29. This is a simulation with seeing of 0.4 arcsec, a guide star magnitude R=8 and a residual jitter of 3 mas. At 300 mas angular separation and performing

ADI post-processing of the data, the Gauss coronagraph reaches a 5σ detection contrast of $\sim 10^{-5}$.

Figure 3.30 shows the relative contribution to stray-light of the different optical surfaces in

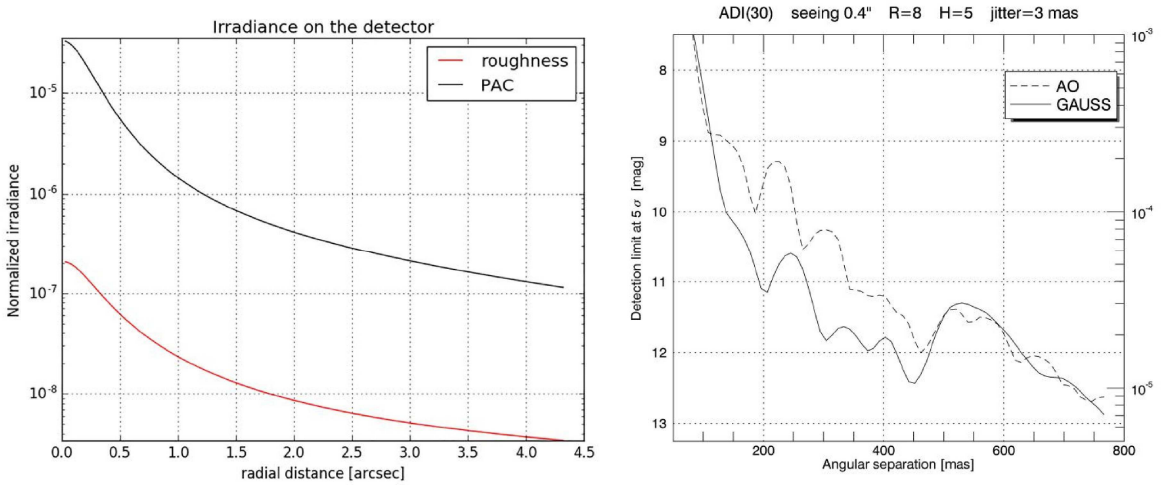

Figure 3.29: Left: simulated stray-light irradiance profile due to micro-roughness (red line) and PAC (black line). Data are normalized by the irradiance of the source. Right: simulated detection curve for SHARK-NIR in good observing conditions (credits: Daniele Vassallo).

the case of micro-roughness (left) and PAC (right). The data refers to the *mean* irradiance on the detector produced by each surface, normalized by the mean value of the total stray-light. In the case of micro-roughness the major contributors are the off-axis parabolic mirrors. This is due to the higher roughness rms and by the fact that they are reflective surfaces. In the case of dust contamination, the relative contribution is quite constant for every optical element except the telescope mirrors (M1, M2 and M3), which have a negligible impact on the stray-light.

The results are preliminary and the routine is now being implemented directly on the coro-

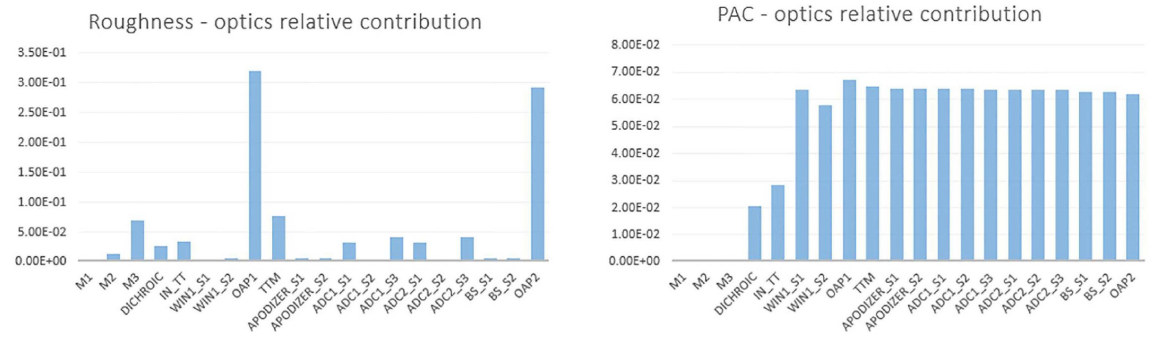

Figure 3.30: Relative contribution to stray-light of the optical surfaces for micro-roughness (left) and PAC (right).

nagraphic simulations so that a more detailed study of the different input parameters will be possible. However, one should remember that results are strictly dependent on the input

parameters. An example of this dependence is shown in figure 3.31, where the roughness of SHARK optical elements has been doubled and the values of particulate contamination are less conservative: ISO class 3 for the clean-room (PAC=3000 ppm) and PAC=7400 ppm for the exposed optical elements. Contamination is again the main contributor to stray-light, but now it is only ~ 7 times higher than micro-roughness. The total stray-light at 300 mas has decreased by a factor of 5 with respect to the previously described simulation.
Moreover, another source of error comes from the accuracy of the scattering profiles. In general, scattering profiles are not very good at small angles [63] and consequently, they should be used with care when dealing with long focal length systems. This is exactly the case of SHARK-NIR.
The conclusion that one can derive from this preliminary analysis is that stray-light from scattering can be of the same order of magnitude as the flux from a detectable planet, and particular care should be taken to limit scattering sources as much as possible. In particular, for NIR observations, scattering from dust particles is probably more relevant than that from micro-roughness. To prevent contamination the system should be assembled in a clean-room, and then sealed to avoid further deposition of dust. Moreover, since big dust grains scatter more strongly at small angles, a cleaning process of the optics aimed at removing large particles would reduce stray-light in the more relevant region, i.e. close to the central source.
Another approach to estimate the amount of scattered light is based on the Power Spec-

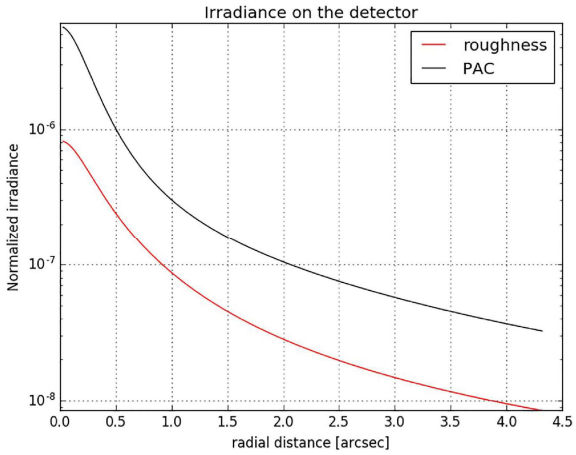

Figure 3.31: Same as in figure 3.29 but with different input parameters (see text for details).

tral Density of the optical surfaces. Church [64], defines optical surface quality in terms of fractal finish, defining three different classes according to their spatial frequency power law: extreme fractal (f^{-2}), Brownian (f^{-3}) and marginal (f^{-4}). Well polished surfaces (with micro-roughness of 1-2 nm rms) tipically exhibit extreme fractal behaviour (see [65]). Applying this model, it is possible to get the amount of scattered light as a function of radial distance from the source. A comparative study following this approach will be conducted to confirm the results obtained with the BRDF method.

3.10 Thermal model

Temperature variations could affect the performance of SHARK and generate a mismatch between the fundamental coronagraphic planes. Moreover, temperature variations during an exposure can lead to changes in the plate scale and the image position that will affect differential imaging techniques. To assess their impact, we developed a simplified thermal model of the SHARK-NIR optical bench. The model is based on the following assumptions:

- Steel optical bench (assumed $CTE = 17 \cdot 10^{-6}$)
- Uniform, isotropic expansion
- the LBT Bent Gregorian focal plane is assumed to be a fixed point for the thermal expansion
- Detector moves only along z direction with $CTE = 24 \cdot 10^{-6}$ (Aluminum)
- Only SHARK optical components are moved, while the telescope is fixed
- The mirror substrate is assumed to be zerodur, leading to negligible changes in the radius of curvature

In the analysis, the details of the optical mountings have not been considered. The optical elements change their size, shape and index of refraction with temperature, and the change in position is only determined by the expansion or contraction of the optical bench. The behavior of the model is sketched in figure 3.32, in which is visible the position of the optical elements for a cold (blue color) and a warm (red color) configuration. The ΔT has been exaggerated for display reasons. As is visible in the figure, the input focal plane is assumed as the fixed point for the expansion.

The image shift induced by thermal variations in the range $-20 - +25°$C is linear and characterized by a shift $\Delta Y = 0.9\ \mu m/°$C (see figure 3.33, left). This corresponds approximately to a shift of about 1 $mas/°$C on-sky.

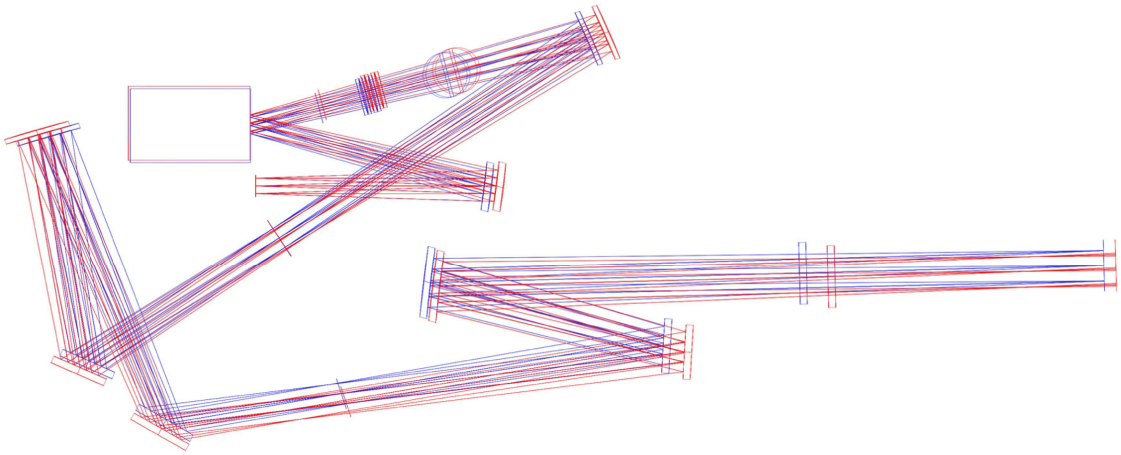

Figure 3.32: Schematic representation of the movements induced by thermal variations.

For what concerns the image plate scale, the estimated variation is $3 \cdot 10^{-5}\ mas/px/°$C, which

corresponds to a movement of about $1/100^{th}$ of pixel at the edge of the FoV for a $\Delta T = 4°C$. Also in this case, the relation is linear in the temperature range under examination (see figure 3.33, right). The results have been corrected for the effect of distortion using a distortion map calculated at nominal temperature.
During an observation, the temperature will probably change of 1-2 deg at most, leading to a negligible evolution of the plate scale of the system, so we can conclude that intra-observation calibrations of plate scale are not necessary.
The thermal model can also be used to evaluate the relative displacement of coronagraphic

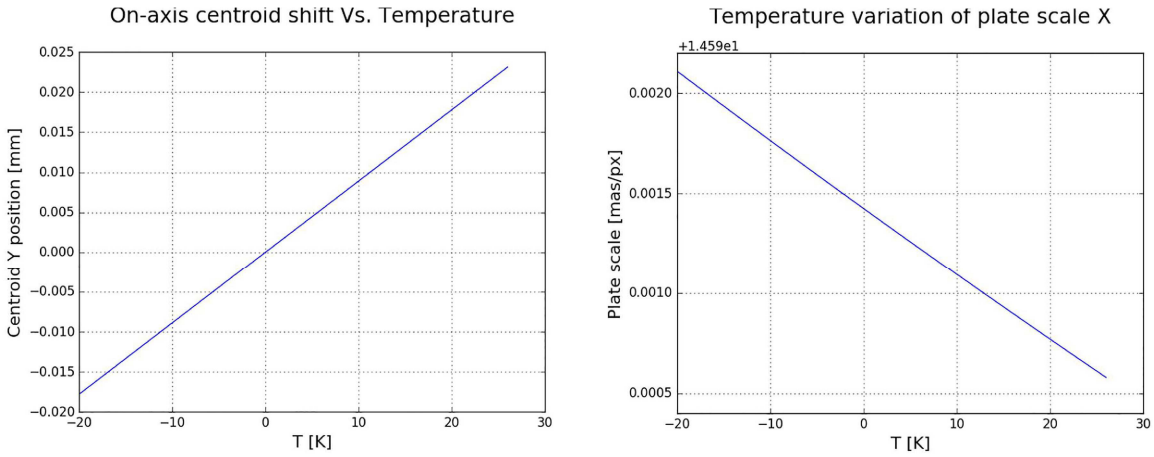

Figure 3.33: Left: on-axis image movement on the science focal plane as a function of temperature. Right: plate scale variation with temperature.

planes. For instance, the relative movement between the TT-WFS focal plane and the occulting mask focal plane could affect the performances of the TT correction. This analysis will be conducted before the FDR and will be included in the error budget of the instrument.

3.11 Conclusions

SHARK-NIR is an instrument designed for high contrast imaging that will exploit the extreme adaptive optics correction provided by the Pyramid based LBT AO systems. As described, three observing modes will be implemented: direct imaging, coronagraphic imaging and spectroscopy. This flexibility will allow to take full advantage of the LBT binocular capabilities, and will give clear opportunities to obtain primary science goals, in combination with the excellent LBT AO performance and also in synergy with other LBT instruments designed for very high contrast imaging, such as LMIRCam.
The optical design of SHARK-NIR is characterized by two intermediate pupil planes and an intermediate focal plane, and will allow the implementation of advanced coronagraphic techniques, such as the Apodized Pupil Lyot Coronagraph or the Shaped Pupil coronagraph. The nominal optical quality is characterized by a very low wavefront error, and an error budget has been allocated to keep NCPA of the since channel within a few tens of nanometers RMS. The analyses conducted so far, show that the instrument is capable of achieving the scientific goals it was conceived for, allowing to reach contrasts better than 10^{-5} at 500 mas separation, when observing bright stars in good seeing conditions [66]. Furthermore, the SOUL upgrade

will improve even more the performance of the AO systems, increasing the number of corrected modes and the speed of the adaptive secondary mirror.
SHARK-NIR has just passed the Final Design Review phase (end of January). If there are no major delays, the instrument is expected to be operative at the end of 2018.

Chapter 4

PLATO

4.1 Introduction

PLATO 2.0 (Planetary Transits and Oscillations of stars) is the ESA Cosmic Vision Program M3 mission selected by the Science Program Committee for launch in January 2024. The main goal of the PLATO mission is to detect terrestrial exo-planets in the habitable zone of solar-type stars and to characterize their bulk properties (radius, mass, density and age). The PLATO 2.0 instrument (figure 4.1) consists of 30 small aperture telescopes (28 with 25 s readout cadence and 2 with 2.5 s cadence), providing a wide field-of-view (2232 deg^2) and a large photometric magnitude range (4–16 mag). It focuses on bright (4–11 mag) stars in wide fields to detect and characterize planets down to Earth-size by photometric transits. The planetary masses can then be determined by ground-based radial-velocity follow-up measurements [67].
In the framework of the PLATO project, I have been involved in the design adaptation and procurement of optics for the realization of a prototype of one of the Telescope Optical Units (TOU). The purpose of the prototype is to test the AIV procedure and to detect possible critical aspects in view of the mass production required for the realization of the whole payload. In the following sections, I'll give a brief introduction to the PLATO project, focusing on the science goals and the telescope design. Then, I'll describe in detail the activity I have carried out for the prototype.

4.2 Science goals

4.2.1 Planetary science

PLATO is a survey mission with the primary target of detecting new planetary systems around bright stars with the transit method. PLATO will be able to detect earth-sized planets around solar-like stars. The determination of the bulk properties of the planets is of paramount importance for a series of reasons, including:

- determine the physical properties of planets for a wide range of systems and enable statistical studies
- understand the link between planetary properties and the formation environment
- determine how planets and planetary systems evolve with age

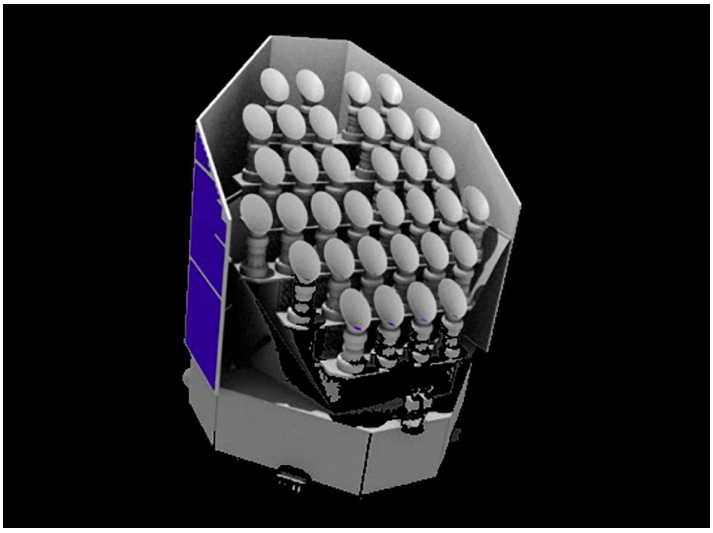

Figure 4.1: 3D model of the PLATO spacecraft

The answers to these questions require the accurate determination of bulk properties of a large number of planets.
The targets of PLATO, thanks to their brightness, are particularly suited for radial velocity follow-up observations from the ground and will provide primary targets for spectroscopic observations investigating their atmospheres. Nowadays, most super-Earths have been found at orbital distances to the star closer than the Habitable Zone (HZ). Some planets have been detected in the HZ by radial velocity or transit observations, but for none of them the mass and radius have been determined at the same time. The goal of PLATO is to provide targets for radial velocity observations of terrestrial planets in the habitable zone of solar-like stars. This necessitates the detection of planets orbiting bright host stars. PLATO's bright target stars allow also for asteroseismology studies increasing not only the accuracy of stellar, and thus planet parameters, but also providing the age of the systems detected. Thus, PLATO will be able to:

- Determine planet radii by transit observations
- Determine planet mass by radial velocity follow-up observations
- Determine the age and physical parameters of the host star by asteroseismology

Moreover, from mass and radius it will be possible to derive the mean density of the planet and infer its physical properties (i.e. whether it is a rocky or gaseous planet).

4.2.2 Observing strategy

The detection of Earth-like planets at intermediate orbital separations, as in the Solar System, is very time consuming, for RV as well as transit techniques. Furthermore, the geometrical transit probability decreases to 0.5% for Earth-like orbits (because of the increased semi-major axis of the orbit) around solar-like stars, affecting transit searches and also decreasing the chances of finding transits for planets previously detected by RV. Fortunately, a large scale, wide-angle space transit survey like PLATO can be optimized by observing a very large

number of stars at the same time continuously and by adopting an appropriate observing strategy. Two observing strategies are foreseen for PLATO: long continuous pointings and shorter coverage of different fields. The two strategies complement each other and allow a wide range of different science cases to be addressed. Long pointings will be devoted to surveys for small planets out to the Habitable Zone of solar-like stars. Short pointings will be devoted to shorter-period planet detections and will address a number of different science cases.
The current baseline observing strategy is the following:

- Two long-duration sky pointings at two different fields on the sky. The first pointing will last from a minimum of 2 years to a maximum of 3 years. The second pointing will last 2 years.

- A step-and-stare observation phase consisting of short-duration observations of several sky fields. This phase will last 1-2 years in total.

The long-period observation phase will significantly increase the number of accurately known terrestrial planets at intermediate distances up to 1 au. This detection range will be unique to PLATO and it is not covered by any other planned transit survey mission. Nor can it be achieved for a large number of RV detections in any feasible observing time.

4.3 Design description

As said before, the payload concept of PLATO is based on a multi-camera approach, involving a set of several Normal Cameras monitoring stars fainter than $m_V = 8$, plus a couple of Fast Cameras observing extremely bright stars with magnitudes brighter than $m_V = 8$. The telescope is based on a fully lens-based design, working in an extended visible light range. It has been designed to be able to observe a very large field, with a sufficiently large pupil diameter.
The 28 Normal Cameras are arranged in four sub-groups of 7 Cameras. All 7 Cameras of each sub-group have nominally the same Field of View, and the line of sight of the four sub-groups are tilted from the payload mean lines of sight, along which the two Fast Cameras are pointing (see figure 4.2). This particular configuration allows surveying a very large field, with various parts of the field monitored by 28, 14 or 7 Normal Cameras. This strategy optimizes both the number of targets observed at a given noise level and their brightness. The Cameras are mounted on an optical bench, which provides structural and thermo-elastic stability to ensure their relative lines of sight do not drift.
Each camera is composed of a Telescope Optical Unit (TOU), the Front End Electronics , the Thermal hardware and a CCD Focal Plane Array, comprised of 4 CCDs. The CCDs work in full frame mode for the Normal Cameras, and in frame transfer mode for the Fast Cameras. The Front End Electronics transmits to a corresponding Data Processing Unit that perform the basic photometric tasks and delivers light curves, centroid curves and images captured by the Cameras.
There is no difference in the TOU design between the normal and fast telescopes (N-TOU and F-TOU), but the latter will include broadband filters.

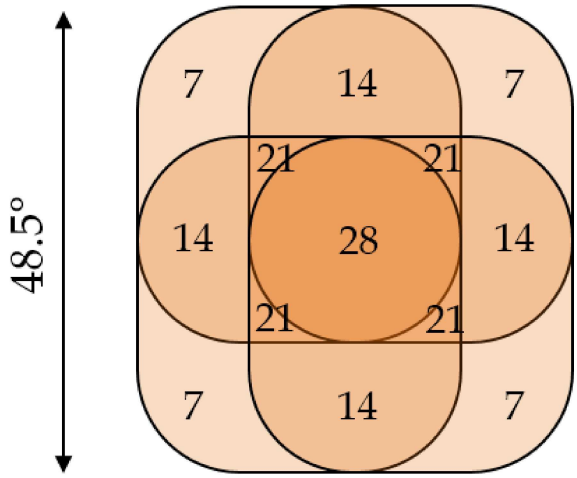

Figure 4.2: Schematic representation of the PLATO FoV with the numbers of telescopes covering each area of the FoV.

4.3.1 TOU Optical design

The current TOU design results from a trade-off of a number of solutions. For the optical design, the main driver comes from the analysis of glass properties with respect to the working environment (in laboratories, launch, and flight conditions), coupled with the capability to deliver performance satisfying the science requirements. The general system parameters and optical performance are reported in table 4.1.

The TOU optical configuration consists of a window, placed at the entrance of the telescope,

Parameter	**Value**
Spectral range	500 - 1000 nm
Entrance pupil diameter	120 mm
Effective focal length	247.527 mm @ 700 nm
F/#	2.06 @ 700 nm
TOU Optical FoV radius	18.8876 deg
Effective FoV Area	1037.3 deg^2
Image quality criterion	90% Enclosed energy $< 2 \times 2$ pix
Maximum field distortion	3.84%
Maximum vignetting	14.1%
Plate scale	15 arcsec/px
Pixel size	18 μm
CCD format	4510×4510 ($\times 4$) px
Nominal working temperature	$-80°$C

Table 4.1: PLATO TOU optical specifications

six lenses, and a physical aperture representing the stop of the optical system. The TOU focuses incoming collimated light onto a focal plane, on which the Focal Plane Array (FPA) is positioned. A layout of the design is shown in figure 4.3, while optical elements parameters,

referring to nominal working temperature and pressure, are reported in figure 4.4.
The inclusion of the window as the first optical element serves multiple purposes: it mitigates

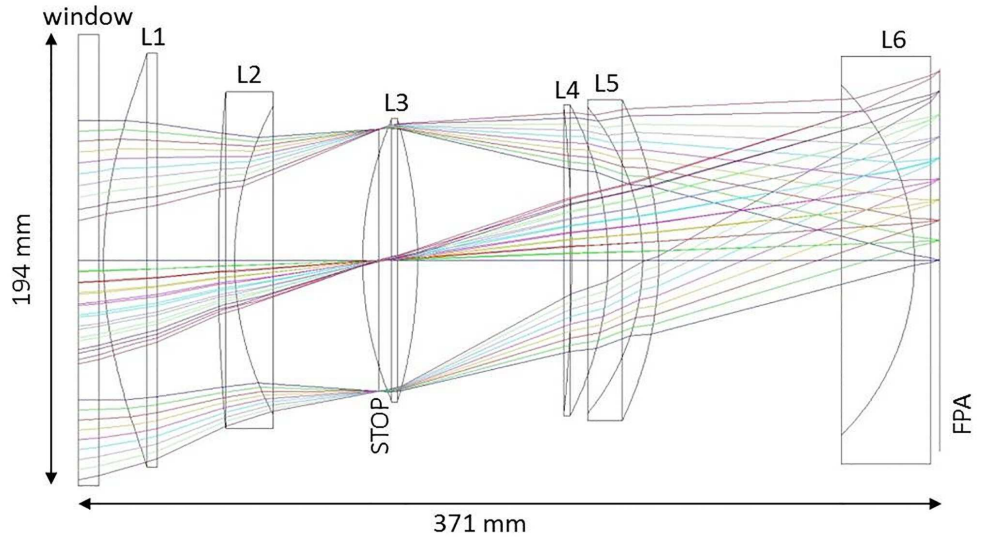

Figure 4.3: PLATO TOU 2D optical layout.

Label Optical Element		Radius of Cuvature (*) [mm]	Thickness [mm]	Aspheric Terms K	Aspheric Terms a^4	Aspheric Terms a^6	Glass	Aperture Shape	Clear aperture Diameter/Size [mm]	Physical aperture Diameter/Size [mm]	Physical Edge Thickness [mm]
Window	Surf. 1	-	9.000	-	-	-	SUPRASIL	Circular	190.000	194.000	9.000
	Surf. 2	-	2.000	-	-	-			190.000	194.000	
L1	Surf. 1	183.457	23.000	-3.87445	3.1477E-08	-4.0894E-12	S-FPL51	Circular	174.000	178.000	4.242
	Surf. 2	-	26.328	-	-	-			174.000	178.000	
L2	Surf. 1	824.888	7.000	-	-	-	N-KZFS11	Circular	140.800	144.800	20.420
	Surf. 2	140.673	62.198	-	-	-			128.260	132.260	
STOP		-	-7.000	-	-	-	-	Circular	112.608	112.608	-
L3	Surf. 1	154.050	23.600	-	-	-	LITHOTEC CAF2	Circular	116.600	120.600	2.612
	Surf. 2	-217.608	66.313	-	-	-			117.800	121.800	
L4	Surf. 1	-648.079	15.600	-	-	-	S-FPL51	Circular	129.400	133.400	2.739
	Surf. 2	-145.416	14.909	-	-	-			129.800	133.800	
L5	Surf. 1	-103.623	7.000	-	-	-	S-FTM16	Circular	128.000	132.000	15.016
	Surf. 2	-159.281	110.051	-	-	-			134.000	138.000	
L6	Surf. 1	-105.733	7.000	-	-	-	N-BK7 (G18)	Circular (**)	146.600 (**)	150.600 (**)	38.508 (**)
	Surf. 2	-	4.000	-	-	-			171.400 (**)	175.400 (**)	
FPA		-	-	-	-	-	-	Square	164.776	164.776	-

(*) Positive radius of curvature means convex surface, negative radius of curvature means concave surface.
(**) L6 has a particular shape (see description in the text). It will be cut in such a way to exploit only the FoV covered by FPA minimizing the lens mass. In the table, it is reported data related to the circular shape which envelope contains L6.

Figure 4.4: PLATO Optical elements parameters in working conditions.

the thermal shock on the first lens during launch; it shields the first lens (glass S-FPL51, moderate rad-hardened glass) from direct incoming high energy radiation (mainly solar protons) and, for this purpose, the current window material is SUPRASIL; for the N-TOUs the window allows the deposition of a high-pass filter in its internal surface, with cutoff wavelength at 500 nm able to define the blue edge of the wavelength spectral range. The red edge is determined by the detector quantum efficiency.
The first surface of the front lens presents even aspheric terms (K, a^4, a^6), while during the

optimization the second surface has been imposed to be flat in order to facilitate the surface interferometric measurement during lens manufacturing. The aspheric terms have been introduced to increase the FoV while maintaining the quality requirements. The L1 aspheric surface has a maximum deviation from the best fit sphere of about 1.086 mm.
The stop of the optical system is a physical circular aperture located in front of the third lens. The stop diameter has been set to 112.608 mm in order to deliver a real entrance pupil diameter of 120 mm.
All the other lenses (L2, L3, L4, L5, L6) have standard spherical surfaces.
The clear apertures of the lenses have been defined through a trade-off with optical elements overall mass. In particular, in order to reduce the impact on the mass, the lenses clear apertures have been undersized, introducing as consequence mechanical vignetting. The amount of mechanical vignetting at the edge of the FoV (field having coordinates 13.6, 13.6 degrees, i.e. radial distance from the line of sight 18.876 degrees) has been estimated to be about 14.1%.
As a working hypothesis, each lens has a margin of 2 mm over the radius between the clear aperture and the physical aperture and minimum edge thickness of 2.5 mm in order to allow mounting, and to introduce margin on the available surface for anti-reflection (AR) coating deposition.
The last lens, the one in front of the FPA, will be cut in such a way as to exploit only the FoV covered by the FPA (avoiding further vignetting), in order to reduce its weight. A scheme representing the L6 shape is shown in figure 4.5. In the current radiation analysis, the expected radiation dose for L6 will deteriorate excessively its transmissivity. For this reason, the L6 glass has been set to the radiation hardened version of N-BK7, i.e. N-BK7 grade 18.

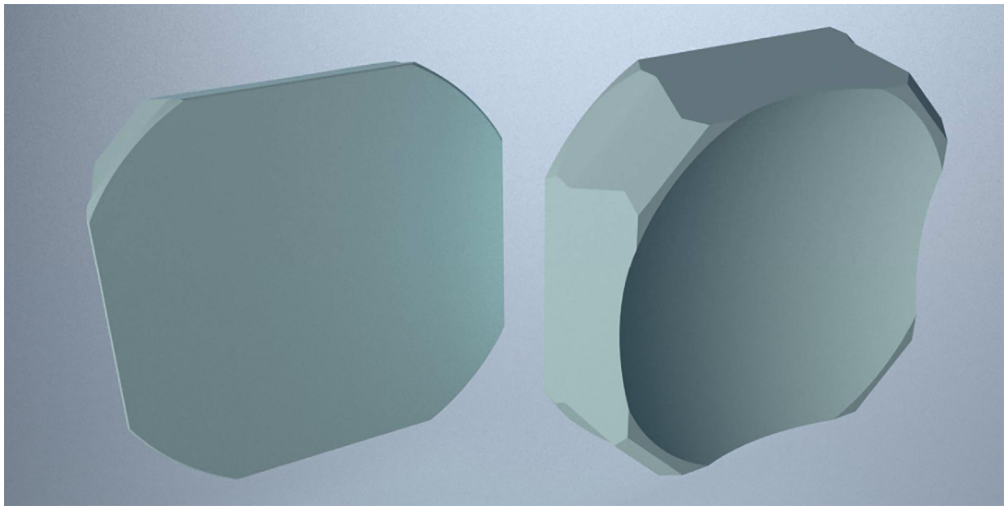

Figure 4.5: Two views of the L6 lens.

4.4 TOU Prototype

At the beginning of the definition phase, ESA raised a few warnings concerning the production and the AIT phase of the TOU units during the implementation phase. All of these concerned the feasibility of fabricating the 28+2 TOU units in a relatively short time schedule (about 2

years). The TOU team has thus decided on a strategy to address ESA warnings during the definition phase, which consist of two main actions:

- A number of studies have been committed by the TOU team to a number of European industries to assess procurement issues, manufacturing, assembly and testing procedures, to highlight critical aspects, planning constraints and costs. The industries consulted are among those having the potential to serve as prime contractors and/or sub-contractors. The delivered studies at the end of phase A allowed a more reliable estimation of the schedule of the implementation phase, of critical aspects if any, and of costs.

- A TOU breadboard has been designed, and produced during the phase A, with the main aim to test the assembly, integration and alignment procedures designed by the TOU team. The Bread-Board (also noted as BB) optics consist of a set of custom made lenses as close as possible to the final design lenses, differing only for some of the glasses and for the usage of a spherical lens instead of the aspherical one (L1). (in addition to that, the usage of a spherical lens instead of the aspheric one also imposes a change of L2 to maintain the on-axis performances).

- A TOU Prototype will be built during Phase B1. It will be an upgraded version of the Breadboard.

The Prototype consists of a refurbished version of the breadboard, in which lenses L1 (aspheric) and L2 are replaced with the final design lenses in order to check, after demonstration of the feasibility of the complete final set of lenses, the performance of a system which is very close to the Flight Model (FM). Moreover, the presence of the aspheric lens also allows an additional optical quality test (in term of PSF shape and dimension) on the whole FoV.

4.5 Prototype adaptation activities

The prototype optical design presents differences in surfaces curvatures, thicknesses and aperture with respect to the baseline optical design. The differences arise from an optimization process necessary to reduce manufacturing cost and time of the optical components of the prototype, but trying to keep the optical quality as high as possible. The company selected for the manufacturing of the lenses, Thales SESO, is the same one that produced the lenses for the breadboard model. The optimization activity was characterized by the following steps:

- **Statement of Work:** consists in the definition of the deliverables from Thales SESO with a first specification of the surface characteristics, the manufacturing tolerances and the schedule for the lens delivery.

- **Tool adaptation:** is the adaptation of the radius of curvature of each surface to the manufacturing tools of Thales SESO, in order to speed up the manufacturing process.

- **Lens cut and mounting interface:** the interface of the lens to the mechanical mounting has been optimized to reflect as much as possible the Flight Model configuration. For this purpose, some of the lenses will be cut in a way similar to that required for the flight model, in order to keep within the mass budget allocated by ESA.

- **Melt adaptation:** is the adaptation of the design after Thales SESO has provided the specific, as manufactured parameters of the glass blanks (index of refraction versus wavelength)

- **Inter-lens distance optimization:** the inter-lens distance has been optimized to account for thermal shift caused by the ΔT from assembly temperature($T = +20°C$) and working temperature ($T = -80°C$), based on a detailed CTE model of the mechanical structure.

In the following, each process is described separately.

4.5.1 Statement of work

The first step has been to discuss with the company Thales SESO the characteristics of the lenses to be produced and their manufacturing tolerances. This preliminary definition had the purpose to prepare the contract, agree on the deliverables, the schedule and the cost.
Considering manufacturing tolerances of radii, central thickness and polishing errors, two different options were proposed by Thales SESO: one with tight tolerances (option 2) and the other with more relaxed tolerances (option 1). They are summarized in table 4.6. Based on the cost and schedule, we opted for option number 1, also considering that:

- In option 1, tolerances on radii and thickness can be fine measured at the end. Thanks to a compensator philosophy, it is possible to create an "as built" optical file with Zemax and fine re-optimize some air spacing to recover performance like that obtained with Option 2.

- Concerning polishing errors, Option 1 takes into account that some surfaces are very far from the pupil (in particular L6) or at an intermediate position. So, their polishing errors over the complete pupil have been more or less relaxed but, if considered over a sub-pupil, they lead to the same performance as other lenses.

For what concerns the melt data of the glasses, the company will provide the standard inspection report giving index values in the visible range, at $\approx 20°C$ and with $\pm 10^{-5}$ uncertainty. Moreover, for reasons of cost, all glasses will be procured without any space-qualification requirements. In particular the N-BK7 grade that will be used for L6 is standard N-BK7 (from SCHOTT) and not the radiation hardened glass BK7G18.
As said before, during the design process, two main activities of design change are foreseen:

- A Tool adaptation, keeping theoretical values for the refractive index. This can be done shortly after ordering.

- A Melt adaptation, trying to keep Thales SESO standard catalogue values for the radii. This can be done when the blanks have been received by the company.

The foreseen time required for all the design adaptation and manufacturing activities is 10 months from the confirmation of order, plus one month in case anti-reflection coatings are requested.

Optical quality as par **Option 1** (relaxed tolerances)	Optical quality as par **Option 2** (improved tolerances)
Tolerances on radii < +/-0.2% but with real values measured to accuracy of +/-0.02%	Tolerances on radii < +/-0.05% and with real values measured to accuracy of +/-0.02%
Tolerances on thickness < +/-0.2mm but with real manufactured values measured up to an accuracy of +/-0.03mm	Tolerances on thickness < +/-0.05mm and with real manufactured values measured up to an accuracy of +/-0.03mm
L1 (having one aspherical side) 4 fringes (or λ/2 RMS) for aspherical side 2 fringes for plano side	L1 (having one aspherical side) 2 fringes (or λ/4 RMS) for aspherical side 1 fringe for plano side
L2 : 1 fringe per face	L2 : 1 fringe per face
L3: 1 fringe per face	L3: 1 fringe per face
L4: 2 fringes per face	L4: 1 fringes per face
L5: 4 fringes per face	L5: 1 fringes per face
L6: 4 fringes per face	L6: 2 fringes per face

Figure 4.6: Manufacturing tolerances options proposed by Thales SESO.

4.5.2 Tool adaptation

The tool adaptation consists of changing the radius of curvature of each optical surface to match a set of reference tools used during the manufacturing process. The tools serve as reference surfaces to evaluate the shape of the lens during polishing. They are different for convex and concave surfaces and have a maximum working aperture. The company suggested not to use tools with apertures less than 80% of the lens aperture to be manufactured, otherwise, the measurements would not be accurate.
The difference between existing tool radii and the nominal values can be partially compensated by changing the thickness of the lenses and their reciprocal distance. Moreover, the aspheric surface of L1 does not require tool adaptation, meaning that the aspheric parameters can be also used to re-optimize the design.
The figure of merit for the estimation of the loss of performance is the fraction of energy enclosed in 2x2 pixels. The estimation also considers a defocus error of $\pm 20\ \mu m$ for the positioning of the focal plane. Figure 4.7 shows the nominal "through focus" enclosed energy for different field positions (denoted by different colors). In the nominal design, the fraction of energy enclosed in 2x2 pixels is always higher than 90% in the defocus range of $\pm 20\ \mu m$.
There are several ways in which tool adaptation can be performed. For example, it is possible to change all the radii of curvature at the same time and then optimize the design a single time, or it is possible to change one surface at a time and optimize at every single step. We decided to use the second approach because it led to better results. When optimizing one surface at a time, the order of optimization matters. We tried different approaches, such as starting from the surfaces near the stop, starting from the radii of curvature closer to that of the tools, or hybrid approaches.
One complication during the analysis arises from the fact that the radius of curvature has to be matched at room temperature conditions, while optical quality needs to be evaluated at working temperature. This means that it is necessary to switch from warm to cold configurations at every optimization step, paying attention to track every change in thickness and

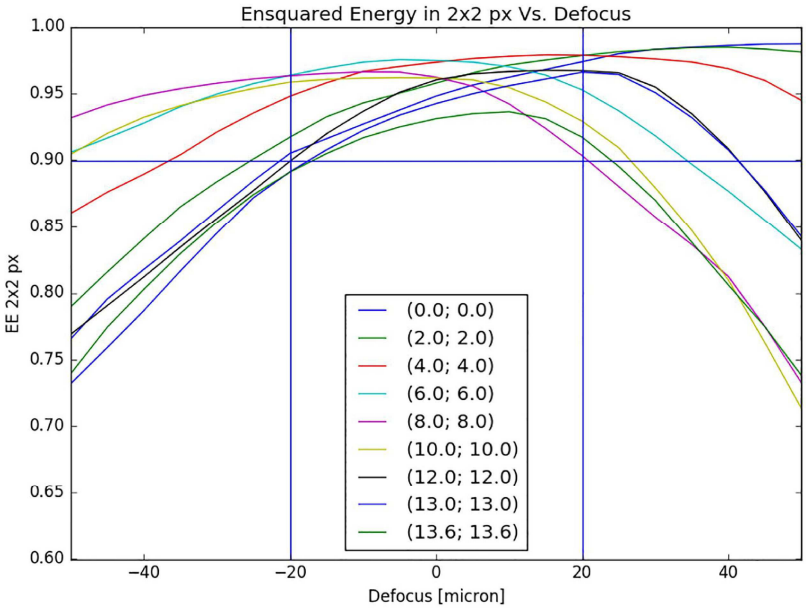

Figure 4.7: Flight model nominal "through focus" EE in 2x2 pixel for different field positions.

distance introduced by the optimization itself.
Figure 4.8 shows the enclosed energy for some of the simulated tool-adapted designs. The plot clearly shows that the outcome of the optimization is quite different, depending on the strategy adopted. System B is very good, but the compensation of the curvature requires an increase of about 3 mm in the thickness of L2 and L5, and of about 8 mm on the thickness of L6. We discarded this solution because it is too far from the flight model to be still representative. Other good options are configurations E and F. In these configurations, the radii of curvature of the first surface of L5 and L6 are not coincident with any manufacturing tool. However, the value of the radius of curvature of the two surfaces is the same ($R = -104.446\ mm$) and we asked Thales SESO to produce a new tool for them. In particular, the performance is very sensitive to the curvature of L6. That's why a new tool was necessary in order to keep the enclosed energy at reasonable values. The difference between configurations E and F is that, in config. F, the thickness of L3 has been slightly increased to have an edge thickness of at least 4 mm as asked by Thales SESO for manufacturing reasons. As a consequence, also the thickness of the other lenses is slightly changed to compensate.
The resulting 2x2 pixel enclosed energy is always higher than 80% accounting for a $\pm 20\ \mu m$ defocus tolerance. For reference, we report in table 4.9 the parameters of the optical surfaces before and after the tool adaptation process.

4.5.3 Definition of the interfaces

After the tool adaptation, we started a discussion involving both Thales SESO and colleagues from the University of Bern, responsible for the design and production of the mechanical structure, in order to define more in detail the mounting interfaces of the lenses, their diameters and adjustments of the thickness. The outcome can be summarized by the following

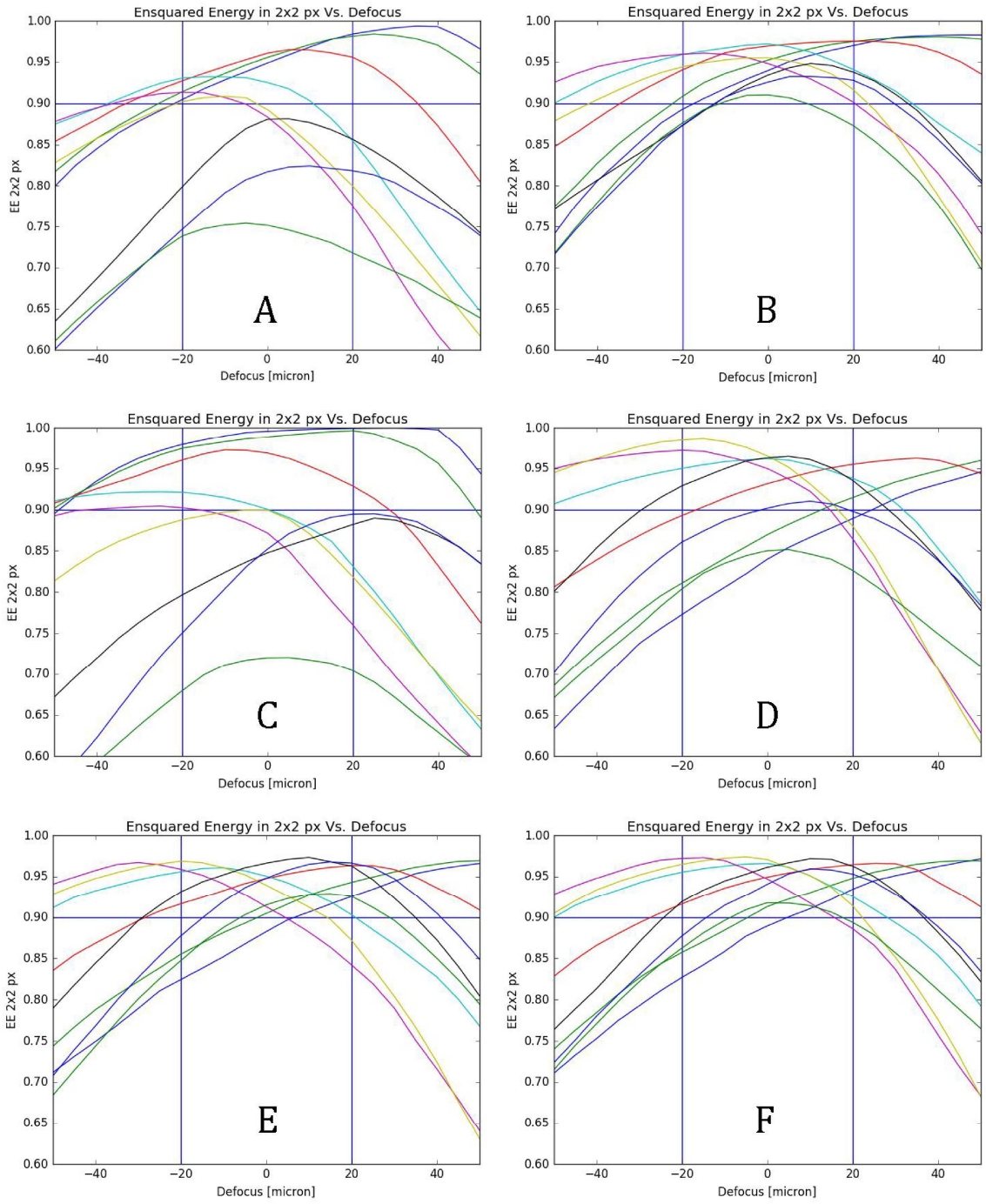

Figure 4.8: Through focus EE in 2x2 pixel for different tool-adapted designs.

design modifications/requirements:

- A chamfer of 0.3 mm should be applied to every sharp edge to prevent stresses and facilitate the mounting.

	Central thickness (mm)		Edge Thickness (mm)		Semi-diameter (mm)		Radius Curvature (mm)		Ø tool / Ø lens
	FM	Tool Adapt.	FM	Tool Adapt.	FM	Tool Adapt.	FM	Tool Adapt.	
L1S1	23.03	23.91	4.25	5.02	89.12	89.80	183.697	184.414	
L1S2					89.12	89.80	inf	inf	
L2S1	7.00	8.00	20.43	21.76	72.45	74.20	825.429	769.440	0.84
L2S2					66.34	67.70	140.766	140.760	1.14
L3S1	23.64	25.53	2.62	4.22	60.41	61.00	154.334	154.365	1.07
L3S2					61.01	61.00	-218.008	-217.170	1.25
L4S1	15.62	17.05	2.74	3.81	66.79	65.90	-648.928	-638.600	1.06
L4S2					66.99	67.90	-145.607	-146.735	0.96
L5S1	7.00	8.22	15.03	16.15	66.06	67.00	-103.716	-104.446	
L5S2					69.06	70.20	-159.424	-158.500	0.91
L6S1	7.00	8.50	38.53	41.41	75.35	76.10	-105.807	-104.446	
L6S2					87.76	89.20	inf	inf	

Figure 4.9: Surface parameters before and after the tool adaptation.

- The mounting interfaces of the lenses, should be polished to the "P2" ISO standard.
- The tolerance on the outer diameter of the lenses should be -0.1/0 mm.
- Lens L2 and L5 will be cut with a step on the outer diameter (as in figure 4.10) to have a flat surface to lay the lens on the mounting structure. In this way, the same mounting concept foreseen for the flight model can be used.
- Lens L4 has no flat surface on the concave side. Since the L4 blank of glass ordered by SESO is not big enough to extend the lens with a flat border, the edge thickness on the concave side was reduced in order to have a 2mm wide flat surface. As a consequence, the clear aperture will also be smaller, meaning that the polishing can be less precise at the edge of the aperture.
- The cutting of L6 will be done as for the breadboard, with some minor differences due to the smaller diameter of the Prototype lens with respect to the one of the breadboard

After this phase, a first set of manufacturing drawings were produced by Thales SESO to confirm all the design modifications.

4.5.4 Melt adaptation

The measured indices of refraction of the glass blanks procured by Thales SESO were sent in two sub-groups: first the melt data for L3, L2 and L6 and then the melt data for L1, L4 and L5. Consequently, the melt adaptation process has been performed in two steps. Here, we will present the final outcome of both optimizations.
To model the real index of refraction of the glasses, we used the "fitting melt data" function of Zemax, which takes as input the measured index of refraction at different wavelengths and interpolates the curve between the data points. The comparison of the catalog values and the fitted values of the refractive index in the wavelength range $0.5 - 1.0\ \mu m$ appears in figure 4.11. The maximum deviation is of the order of 10^{-4} for lens L1 (the biggest blank), while the typical deviation is of the order of $5 \cdot 10^{-5}$ for the other lenses.
Compensation is achieved by changing the thickness of the lenses, the surface parameters of L1 (radius of curvature and aspheric parameters) and the inter-lens distance. Table 4.12 summarizes the design parameters before and after the melt adaptation process. The data

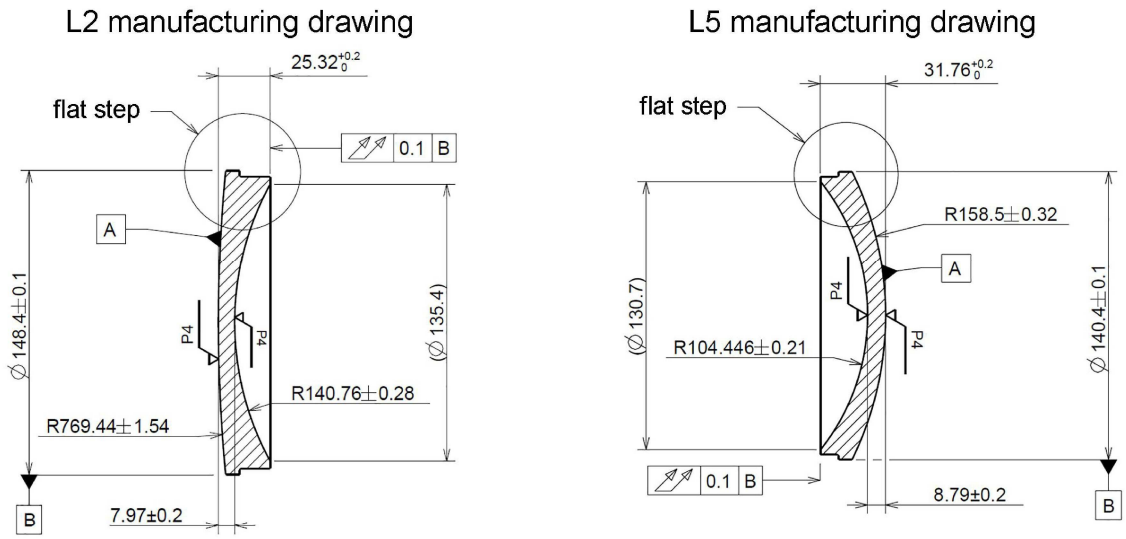

Figure 4.10: Manufacturing drawings of L2 (left) and L5 (right).

refer to room temperature ($T = 20°\text{C}$) and pressure ($P = 1\ atm$). The change in thickness is of the order of 200-500 μm and is slightly higher than the manufacturing error. The design changes have been sent to Thales and have been implemented in the final mechanical drawings of the lenses that have been used for the final optimization process i.e. the inter-lens distance optimization based on the thermal model of the mechanical structure.

4.5.5 Thermal model adaptation

This operation involved the optimizing the inter-lens distance at room temperature, in order to achieve the optimal performance at the working temperature. Going from warm to cold conditions, the distance between the lenses changes, due to contraction of the supporting mechanical structure and the change in index of refraction and curvature. The supporting structure for the Prototype is represented in figure 4.13. The lens mountings are fixed to 5 mount flanges (blue in figure) and each flange is connected to the following one by a set of three rods (purple in figure). The inter-lens distance can be easily adjusted by changing the length of the rods connecting the support flanges of the lenses. The rods are made of Inconel Alloy 601 with a CTE of $13.75 \cdot 10^{-6}\ K^{-1}$. However, the rods can control only the distance between four lenses (L3-L4-L5-L6) since there are only four sets of them. The distance between L1 and L2 and that between L2 and L3 can be changed by acting on the thickness of the shims that link the lens mount to the support flange. The shims are made of titanium alloy (Ti6Al4V) with a $CTE = 9.3 \cdot 10^{-6}\ K^{-1}$.

The CTE map of the structure was provided by the University of Bern, while for the thermal modeling of the optics we used catalog data provided by Zemax. The optimization was characterized by the following steps:

- Setup of the starting model from the manufacturing drawings of the lenses and the mechanical structure at room temperature. For each thickness of a given material of the mechanical structure, a different surface was used in order to have control on the CTEs of the different pieces.

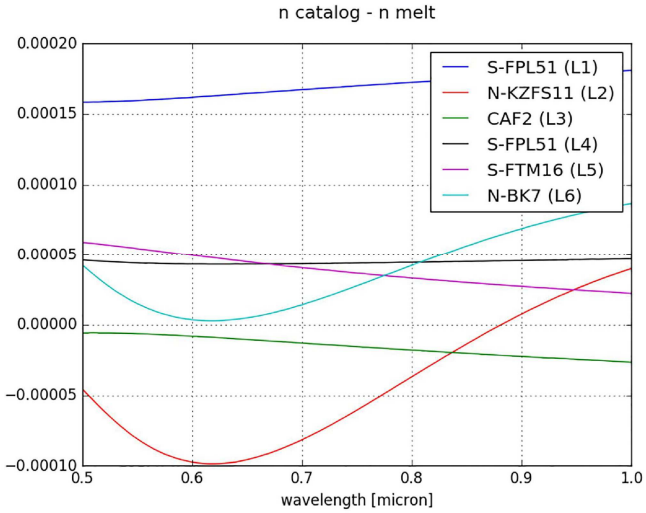

Figure 4.11: Refractive index difference between melt value and catalog value for all the six lenses.

- The model was transformed to its equivalent at cold temperature by modifying the thicknesses, the radii of curvature, and the refractive index, based on the CTEs. It was not possible to directly start from the cold model, because, although the cold optical model was already available, the effects of the mechanical model provided by University of Bern had to be introduced as well.

- The length of the rods and of the useful shims was allowed to change in order to maximize the optical quality at cold temperature. The figure of merit is again the 2x2 pixel enclosed energy.

- The system was transformed back to room temperature and the optimized length of the components was implemented in the mechanical design.

The output of each process is summarized in figures 4.14, 4.15 and 4.16 which show a schematic model of the thicknesses and distances between components. The figures refer respectively to: (1) the system at room temperature before optimization, (2) the system at cold temperature after optimization and (3) the optimized system at warm temperature. The modifications to the mechanical design are very small: below 100 μm. This is also because a uniform CTE of $13.9 \cdot 10^{-6}\ K^{-1}$ was already taken into account in the previous optimization processes and the value is not very far from the actual CTEs of the structure.
Once the Prototype will be built and tested at cold temperature, it will be possible to assess the accuracy of the thermal model. In fact, the temperature variation between the integration and working conditions is $\Delta T = 100°\text{C}$ and the thermal behavior can deviate from the linear regime. This test would be also helpful to assess if other compensation strategies will be needed for the flight model, like actively controlling the temperature of the structure and understanding reasonable ranges for the compensators.

Central Thickness [mm]		
Lens	Before melt	After melt
L1 S1	23.909	23.556
L2 S1	8.000	7.972
L3 S1	25.531	25.531
L4 S1	17.054	17.446
L5 S1	8.221	8.786
L6 S1	8.500	8.721

Edge Thickness [mm]		
Lens	Before melt	After melt
L1 S1	5.020	4.786
L2 S1	21.764	21.736
L3 S1	4.224	4.224
L4 S1	3.808	4.201
L5 S1	16.149	16.713
L6 S1	41.408	41.629

L1 Profile		
	Before melt	After melt
L1 Radius [mm]	185.613	185.782
K	-3.941435	-3.857031
a4	$3.061542 * 10^{-8}$	$2.917076 * 10^{-8}$
a6	$-4.017096 * 10^{-12}$	$-3.947929 * 10^{-12}$

Figure 4.12: Optical parameters of the lenses before and after melt adaptation.

4.6 Prototype Assembly, Integration and Test

The TOU opto-mechanics AIT plan is to realize, assemble and integrate a thermally equivalent prototype of the telescope opto-mechanics in the laboratories of INAF-Padova, where preliminary tests on the "warm" optical quality will also be performed. Tests on the TOU breadboard are finalized to reach a detailed design of the instrument, a consolidated development plan (procedure, schedule and cost) and a consolidated definition of the TOU interfaces with the rest of the payload. The AIT procedure of the telescope has been developed in close co-operation with industry (Leonardo-Finmeccanica), using as much as possible the same concept, the same opto-mechanical setup and the same Ground Segment Equipment (GSE) which will be used by the industry itself. In this way, the AIT tests performed at INAF-Padova will be significant not only in terms of feasibility of the TOU assembly and integration, but also in terms of the time required to successfully conclude it. The latter is of course a crucial issue, due to the considerable number of telescopes that will be delivered on a relatively short timeline of about two years. Also the "cold" test on the TOU prototype will be devised in close co-operation with the industry, and performed using facilities available at their premises, in order to identify at industrial level all the needed GSE and a clear strategy for the testing phase of the future TOUs to be delivered and qualified. Of course, one of the output of this prototyping strategy, devised and developed in co-operation with industry, as just mentioned, is also to ensure that an alignment procedure performed in warm conditions, and initially tested in warm too, allows us to obtain the required optical performance in cold conditions. At the end of phase B1, the prototype shall meet the requirements in term of optical quality and focal plane position, or should give advice to implement design modification to meet the requirements. At the same time, at the end of phase B1, the AIT procedure strategy shall be clearly devised; even more, an opto-mechanical concept for the AIT should be clearly identified and a strategy for the warm and cold test to be performed on the TOU opto-mechanics shall also be clear for their verification during the implementation phase. The latter shall allow us to verify, for each delivered TOU, the most crucial parameters, such as the optical quality and the position of the telescope focal plane.

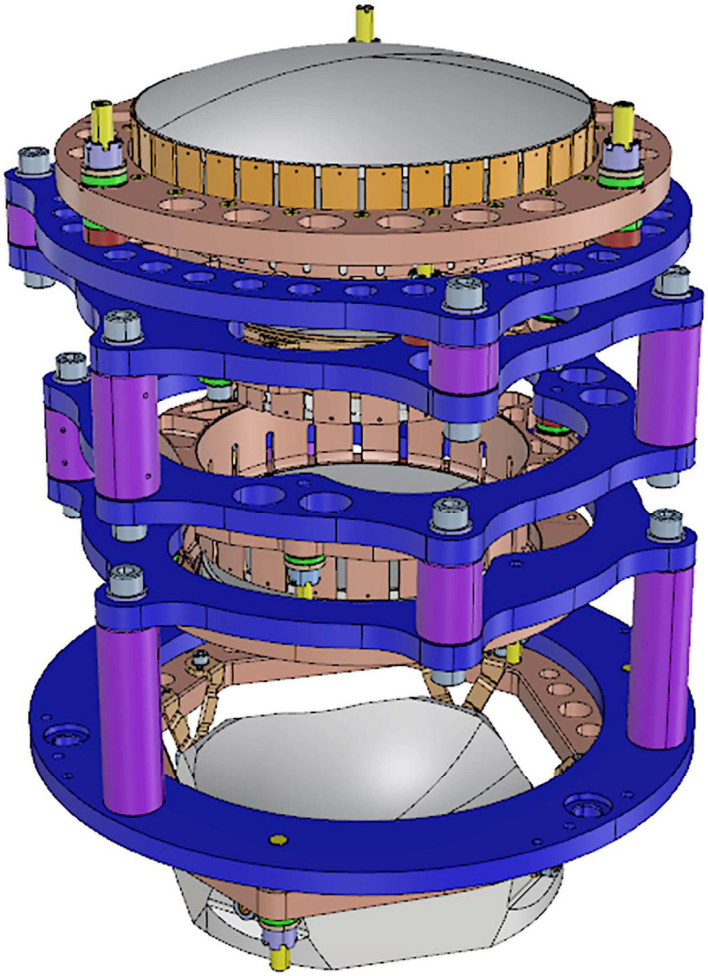

Figure 4.13: 3D layout of the opto-mechanical structure of the PLATO Prototype.

4.6.1 AIT concept

Figure 4.17 shows the concept of the TOU AIT. A collimated laser beam, with a variable diameter, will be used as reference for the alignment of the lenses, which will be inserted in the optical path one at a time and will be aligned with respect to the laser beam itself. The lens alignment will be performed looking at the back reflected spots and at the Newton rings, when visible, on a test camera collecting the light reflected by the lenses. On a second test camera the transmitted spot position is monitored as well. In order to maximize the contrast and the Airy and Newton rings visibility:

- Light shields will be inserted between each lens, to isolate the back reflected light, when needed, coming only from that lens.
- A variable diameter iris will be inserted in the collimated beam, to maximize the transmitted and back-reflected spot visibility.
- Both setup cameras will be focusable.

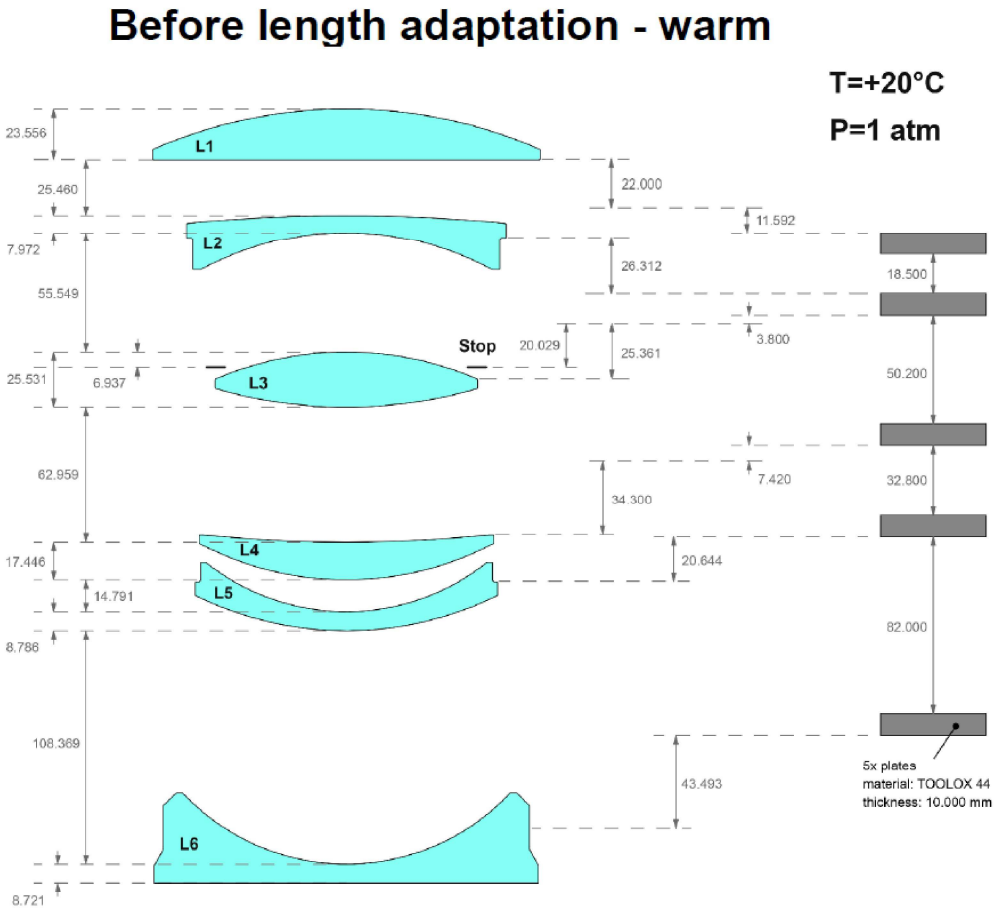

Figure 4.14: Prototype TOU Parameters at room temperature before optimization.

The opto-mechanical design of the TOU introduces some AIT constraints concerning the order in which the lenses have to be inserted in the TOU structure:

- Lens L3, the closest to the system physical pupil, will be the reference for the alignment, and it will be mounted on the mechanical structure centered with mechanical precision. It is the first lens to be inserted inside the structure and the laser beam which will be used as a reference for the alignment will be, as a first step, aligned to L3 itself.

- The lenses will be mounted one at a time, aligned to the reference beam and eventually tightened.

- To allow an easier assembly of the lenses inside the structure and, above all, the realization of a simple GSE for the centering of the mounts during the alignment of the system, the TOU mechanical structure will be kept vertical during the Prototype AIT, in a way gravity will help doing the job. In these phases, a handling structure is required, to hold the TOU mechanical structure vertically and to allow a 180 degrees rotation of the entire telescope, in order to insert the lens mounts always from the top.

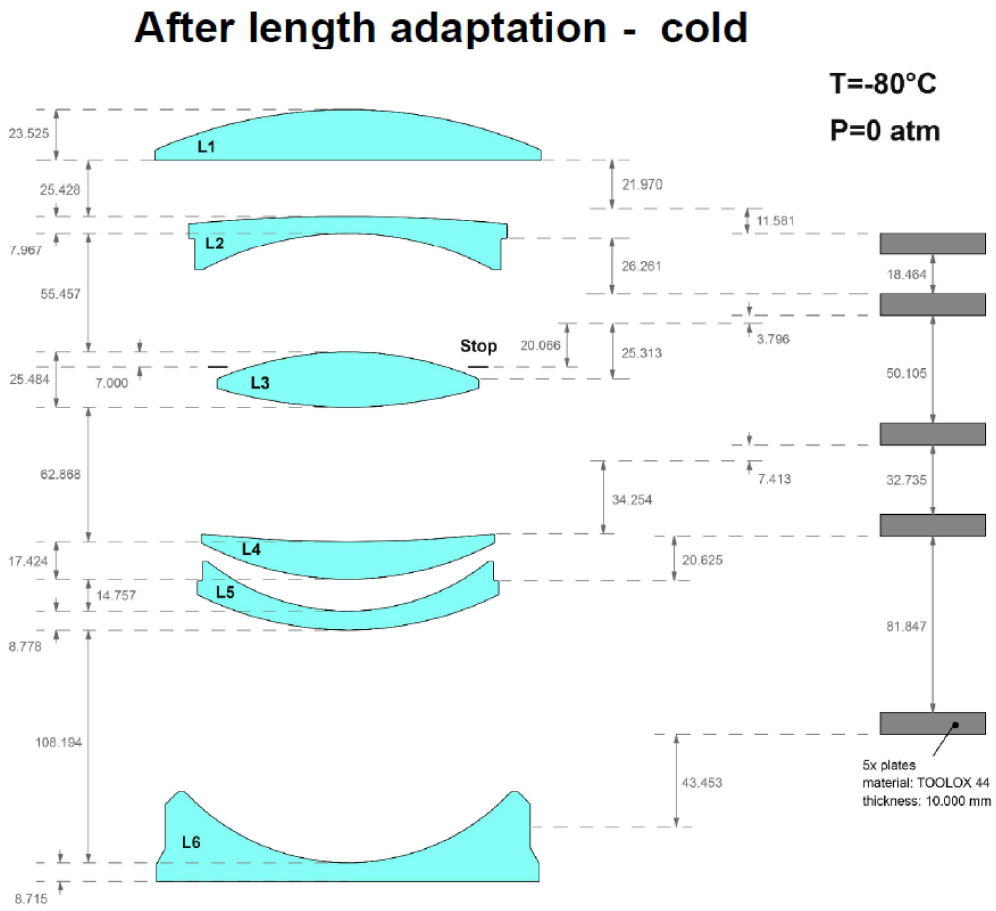

Figure 4.15: Prototype TOU Parameters at cold temperature after optimization.

4.6.2 Alignment sequence

During the assembly of the TOU, the convergence of the beam transmitted by the lenses is not guaranteed, or the beam may focus on an accessible position very far from the telescope. This depends also on the order of insertion of the lenses. In order to understand if there is an assembly sequence that allows us to have the transmitted focused spot in a position accessible by the test camera, we simulated the alignment procedure in Zemax. The purposes of the simulation were the following:

- Understand if there is any possible sequence for the mounting of the lenses that forms a focused spot at a reasonable distance from the telescope every time a new lens is added to the optical train.
- Find the sequence that minimizes the focal shift required by the test camera to reach the focal planes and that minimizes the number of rotations of the structure that holds the TOU.
- Keep track of the size of the spot to check the characteristics required of the test camera (pixel and format size).

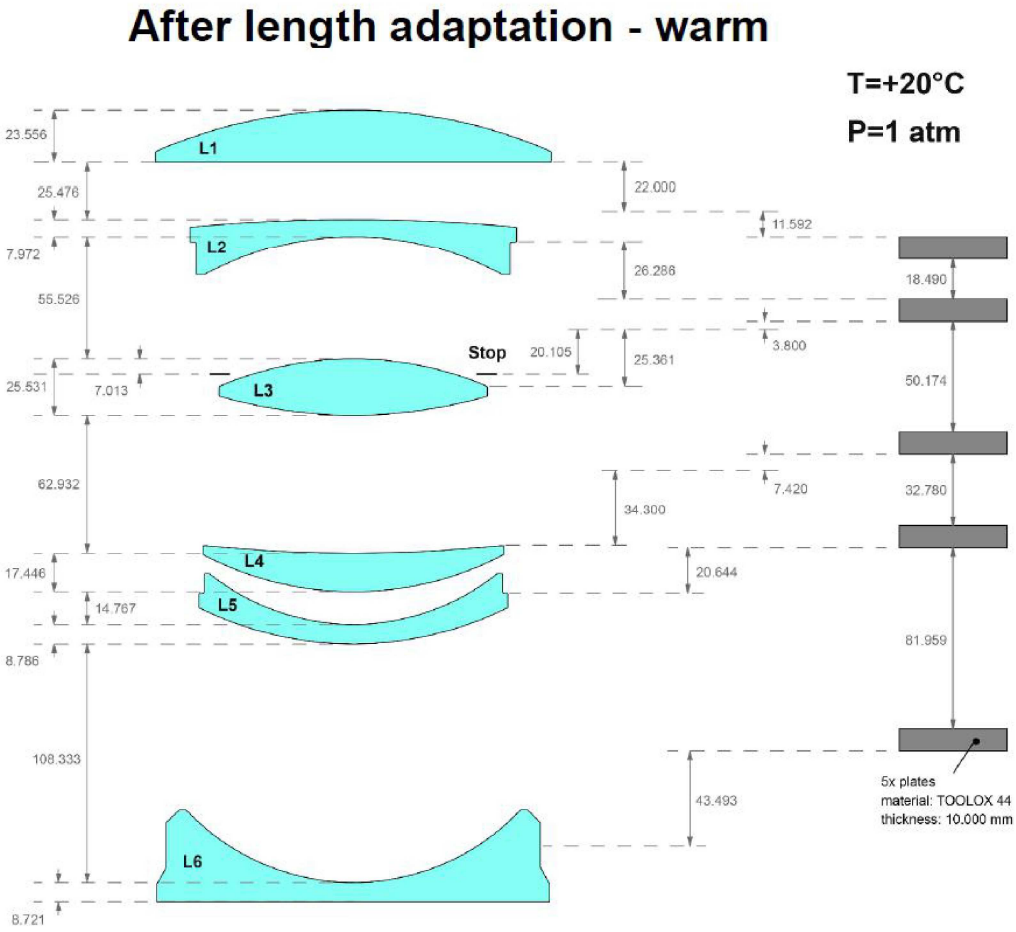

Figure 4.16: Prototype TOU Parameters at room temperature after optimization.

The only combination that results in a reasonable range of transmitted focal positions is L3-L4-L2-L1-L5-L6. The sequence requires only 4 rotations of the handling structure. If the rotation axis of the structure is placed approximately at 45 mm from the optical stop of L3 in the direction of L4, the focal shift is minimized and is equal to $\Delta Z \sim 113\ mm$. Such a range can be easily covered with a precision linear stage.
Figure 4.18 shows a schematic view of the alignment procedure. The tower must be rotated to align L3, insert L2, insert L5 and to test the optical quality after L6 is inserted. In fact, L6 is the only lens that will be mounted from the top but the focus must be measured after rotation of the whole TOU. For all the other lenses, the focal position can be measured without rotating the handling tool, facilitating the alignment procedure.
As is visible in the figure, in some configurations the focus is formed inside the structure. For this reason, the test camera support structure should allow us to insert it inside the TOU for measurement and to move it away when the tower needs to be rotated.

The size of the spot depends on the size of the beam used to illuminate the lenses. In fact, spherical aberration is particularly big for certain combinations of lenses and the lateral ray aberration depends on the aperture illuminated. Assuming the diameter of the beam to be 30 mm, the biggest spot dimension is of the order of 200 μm and happens for the combination

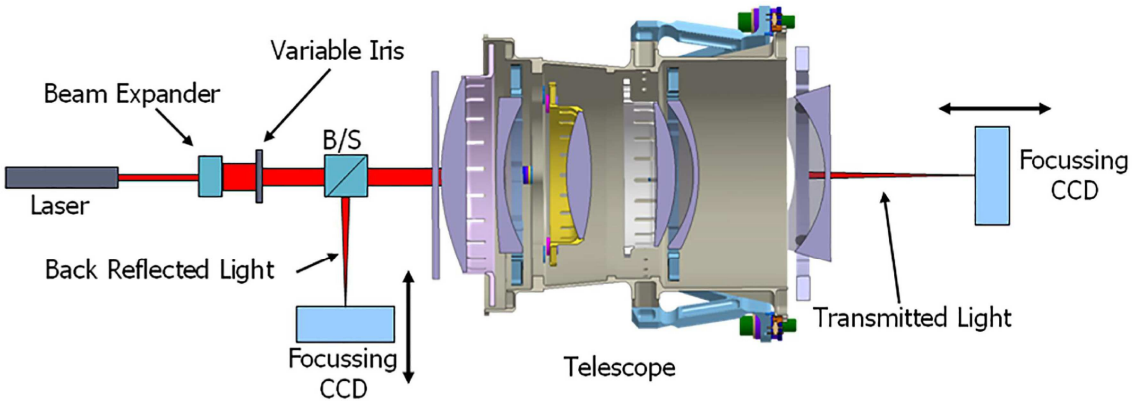

Figure 4.17: TOU alignment concept.

L2-L3-L4. The dimension can be covered by a common image sensor.

4.6.3 Sensitivity to de-focus of lenses

During integration, the position of the intermediate focal planes is used to position lenses at the correct distance along the optical axis. In order to understand the relation between lens de-focus and shift of the focal plane, we ran a sensitivity analysis for every combination of lenses. We considered movements of the lenses along the optical axis of 10, 50, 100 and 400 μm and measured the shift of the best focus position. The results are reported in figure 4.19. The relation is linear for all cases, but the coefficient of proportionality depends on the configuration considered. For example, to position lens L2 within a 100 μm de-focus error, it is necessary to estimate the best focal plane with an accuracy of 60 μm. To achieve the same precision with the lens L4, the accuracy required for the determination of the best focal plane is 18 μm.
To increase the sensitivity on the determination of the focal plane, it is possible to illuminate the lenses with a larger beam and to perform a Hartmann mask test. A preliminary investigation of the feasibility of this approach is discussed in the next section.

4.6.4 Alignment with Hartmann test

We simulated a Hartmann test by non-sequential ray-tracing with Zemax. The Hartmann mask used in the simulation exploits the full aperture of the lenses and is composed of 8 holes placed in a circle of 90 mm diameter. Each hole has a diameter of 4 mm. Holes are placed in a single ring to minimize the effect of spherical aberration. In this way, they reach focus at the same position of the caustic and are easier to identify in the intra and extra-focal images. The detector used is a PROSILICA GT3300 with a format of 3296x2472 px and pixel size of 5.5 μm.
The best focal position has been determined in the following way:

- we simulated 5 intra-focal and 5 extra-focal images of the spots with ray-tracing (figure 4.20, left). The only noise source is the one arising from the finite number of rays traced ($5 \cdot 10^6$ rays)

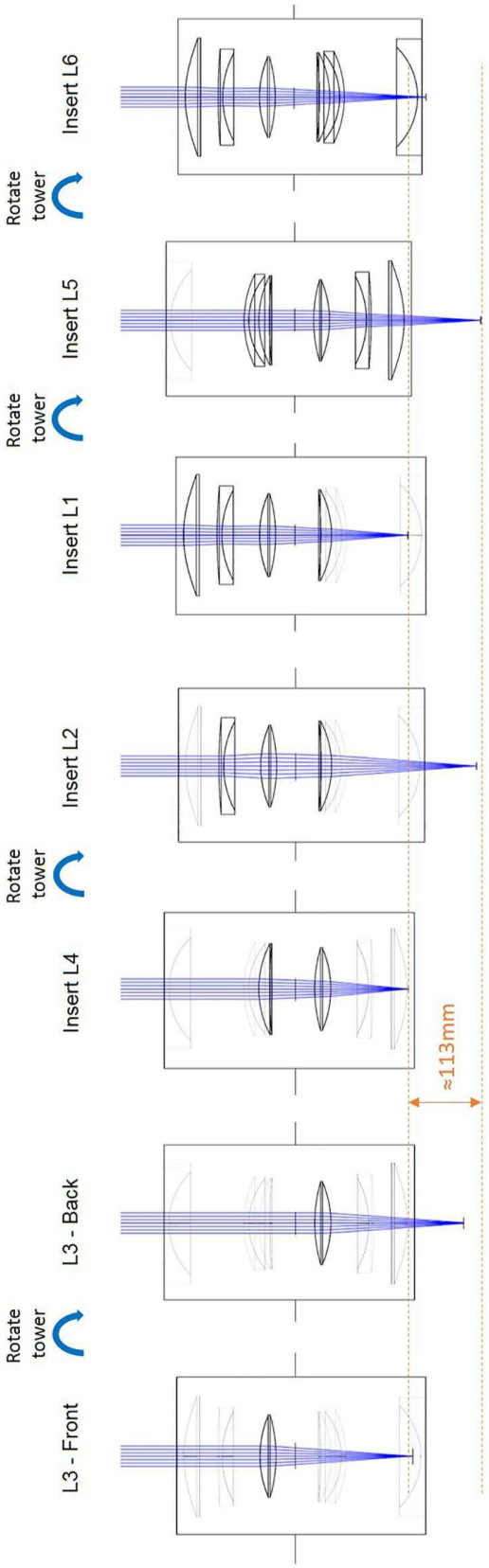

Figure 4.18: Alignment sequence for the TOU.

	Lens de-focus error [mm]				
	0	0.01	0.05	0.1	0.4
L3L4	0	-0.002	-0.009	-0.018	-0.072
L3L4L2	0	-0.006	-0.03	-0.061	-0.245
L3L4L2L1	0	-0.003	-0.013	-0.026	-0.103
L3L4L2L1L5	0	-0.002	-0.01	-0.021	-0.086
L3L4L2L1L5L6	0	-0.001	-0.005	-0.01	-0.04

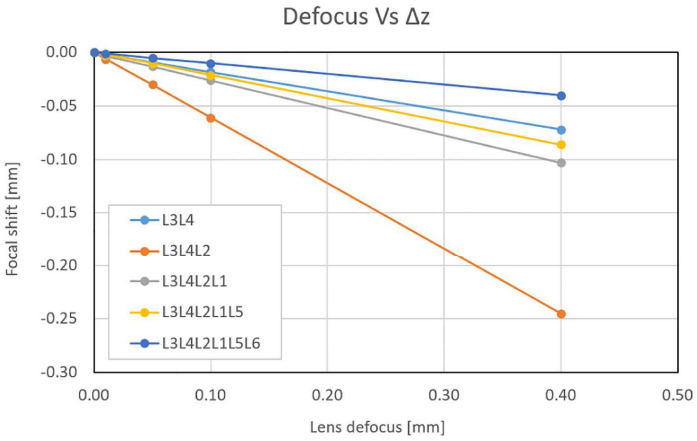

Figure 4.19: Sensitivity to lens de-focus for the alignment procedure.

- the position of the spot is determined by an automatic routine that detects the spots on the image and finds the position of their centroid.
- we used a least square method to find the best line connecting the intra and extra-focal spots (figure 4.20, right)
- The best focal position in the z-direction is identified minimizing the RMS of the points found intersecting the lines with z-slicing planes

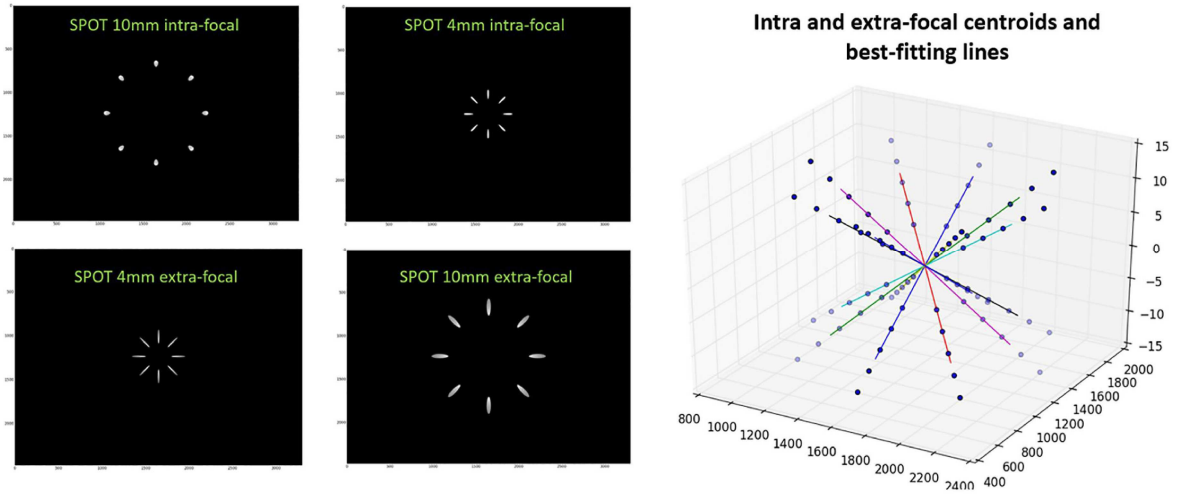

Figure 4.20: Left: synthetic intra-focal and extra-focal images from ray-tracing. Right: Best linear fits of the spot centroid for the determination of the focal position.

Taking as an example the configuration with L3 and L4 inserted, and considering a de-focus of L4 of $\Delta z = 50\ \mu m$, we get a shift of the focal plane of 5 μm, which is in agreement with the result from the sensitivity analysis. Some further tests on the synthetic spot images show that the procedure is very stable and the result does not change (sub-micron stability) if

only a part of the intra and extra-focal images or if a different intensity threshold is used to automatically identify the spots. The conclusion is that we can achieve a sufficient sensitivity on the determination of the focal plane position with the Hartmann test, but no error sources were considered except the statistical noise of the ray-tracing.
A second set of simulations was dedicated to test the procedure when the Hartmann mask is displaced with respect to the optical axis. We considered a decenter of the mask of 1 mm from the optical axis and produced a new set of intra-focal and extra-focal images. Adopting the same routine for the determination of the best focus we get an error of 17 μm, which is higher than the error we would like to achieve (less of 5 μm). Similar results are obtained for the other combinations of lenses.
We can conclude that the Hartmann test is a good method for the determination of the best focus position, provided that the Hartmann mask is accurately aligned to the optical axis of the system.

4.7 Conclusions

PLATO is an ensemble of small telescopes, that will search for exoplanets by looking simultaneously toward a direction of the sky with partially overlapping FoV. This concept, has been granted selection by ESA as a Medium sized mission, and is going to be soon adopted for a launch, currently foreseen in 2025.
PLATO promises to produce a catalog of accurate radii, masses and densities of exoplanets orbiting bright stars, opening the path towards a statistical study of the properties of earth-sized exoplanets.
The big number of telescopes composing PLATO requires a detailed assessment of the manufacturability of the Telescope Optical Units, and the validation of a fast and reliable AIV procedure. In order to demonstrate the feasibility of the proposed design, and to check the AIV procedure, a Prototype of one of the TOUs in under development. The specifications of every optical element of the Prototype have been optimized and adapted for the production by the industry. Simultaneously, the colleagues from University of Bern have designed and produced the mechanical structure and the mountings. All the pieces are now ready and will be sent to the Astronomical Observatory of Padova for the assembly, integration and test of the TOU. The test of the optical quality of the aligned system at working temperature ($T = -80°\mathrm{C}$) is foreseen by the end of September 2017.

Chapter 5

Conclusions

Developing optical designs for astronomical instrumentation is a challenging and stimulating activity. It involves first understanding the scientific requirements for the instrument, then assessing the limits or motivations behind similar current or past instrumentation and finally, shaping the new system step by step. In this Thesis, I described optical solutions for three new astronomical instruments that will hopefully enable new scientific discoveries in the forthcoming decades. The work is not limited just to the delivery of the best possible image quality, but rather it involves a careful evaluation of all the constraints coming from "real world" conditions. These constraints are the real reasons for which a given design can be successful and another cannot. Many examples have been encountered during the Thesis: limitations on volume, on mass, stray-light due to scattering, stability of the system to misalignment or thermal variations, resistance to high levels of radiation or thermal background, just to cite some of them.

This is why the design is usually a multi-step process. A first optical configuration is chosen and optimized based on a starting set of general requirements. In this phase, it is already possible to take into account the major constraints that are already known. Then, a preliminary set of analyses is carried out on the design and, most probably, some modifications are required. The change can involve some details or also a major revision of the optical configuration. This is what happened for JANUS in which, after a careful evaluation, it was estimated that the mass of the opto-mechanical structure was higher than that allowed by the spacecraft and the optical configuration had to be changed. The new configuration is slightly worse in terms of stray-light, but also has some advantages related to manufacturing and alignment of the optics.

Also SHARK-NIR underwent modifications. In fact, at the beginning, it was characterized by a bigger FoV, one coronagraphic pupil plane and an all-cryogenic design. Then the design evolved towards a smaller FoV, and a partially-cryogenic design hosting two coronagraphic pupil planes. The new design is better in terms of flexibility of observations, but the expected thermal background is higher and the bandwidth needed to be limited to $\lambda < 1.7\ \mu m$. Essentially, the evolution of the design requires a set of trade-offs that slowly approaches the final design of the instrument.

Another important point that came out several times during the evaluation of performance is the trade-off between the accuracy and time spent for the analyses. In general, to produce more accurate results, it is necessary to spend more time for the definition of the system properties and to check that all the inputs are correct. This can cause delays in the project,

so it is necessary to understand what is the most reasonable level of detail achievable based also on past experience. The results of the analyses presented in this Thesis are a perfect example of this aspect. They are usually based on simplifying assumptions. Nevertheless, they provide useful input for design optimization. Examples are the optimization of baffles in JANUS, the cut-off wavelength in SHARK-NIR or the design adaptation procedure for the PLATO prototype.

Finally, there is the creative side of optical design which is particularly relevant during the first phases, but it plays an important role during the optimization and fine-tuning of the design as well. In fact, all instruments start from some requirements and a white piece of paper (or a white screen) and the optical design of the instrument takes shape from the combination of physical laws, creativity and experience. While the first of these three ingredients is (probably) immutable (although not completely known or understood), the last two ingredients are somehow competing. Experience is a very powerful tool, since we can use it to solve problems based on the knowledge gained in the field. It takes time to acquire, but it saves a lot of time for future works. In a certain way, it is "easier" to exploit past experience rather than create new ones. On the other hand, creativity is necessary when dealing with new problems and scientific challenges. Most of the creative work realized for JANUS, SHARK and PLATO consisted in putting together knowledge and solutions coming from other instruments and adapting them to the fulfillment of the science requirements. Some solutions were successful, while others could not be applied, for example, due to constraints on volume, or because they did not achieve the desired performance. Then, of course, creativity is needed for fine-tuning of the details, like the choice of glasses for the ADC, the modification of the baffle design, or a smart folding of the system to exploit the available volume in the best possible way.

The work realized during these three years has played a crucial role for the optimization and the definition of the optical components that will build up JANUS, SHARK and PLATO. The importance of the solutions implemented on the optical design of the three instruments is quite evident, both because in principle they will deliver high quality images and enable new observations and because they can serve as a reference for future instrumentation.

Acronyms

ADC	Atmospheric Dispersion Corrector
ADI	Angular Differential Imaging
AGN	Active Galactic Nuclei
AIV	Assembly Integration and Verification
AO	Adaptive Optics
AR	Anti-Reflection
ASM	Adaptive Secondary Mirror
BS	Beam Splitter
BSDF	Bi-directional Scattering Distribution Function
CDP	Conceptual Design Phase
ELT	Extremely Large Telescope
FDR	Final Design Review
FP	Focal Plane
FPA	Focal Plane Array
FLAO	First Light Adaptive Optics
FM	Fold Mirror
FoV	Field of View
GSE	Ground Segment Equipment
HA	Hour Angle
IWA	Inner Working Angle
JUICE	JUpiter ICy moons Explorer
LBT	Large Binocular Telescope
LBTI	Large Binocular Telescope Interferometer
MTF	Modulation Transfer Function
NCPA	Non-Common Path Aberrations
NIR	Near InfraRed
OAP	Off-Axis Parabola
OWA	Outer Working Angle
PAC	Percent Area Coverage
PLATO	PLAnetary Transits and Oscillations
ppm	Part Per Million
PSD	Power Spectral Density
PST	Point Source Transmittance
RON	Read Out Noise
SDI	Spectral Differential Imaging
SFR	Star Forming Region

SHARK	System for coronagraphy with High order AO from R to K band
SNR	Signal to Noise Ratio
SR	Strehl Ratio
TOU	Telescope Optical Unit
TT	Tip Tilt
WFE	Wave-Front Error
WFS	Wave-Front Sensor
XAO	eXtreme Adaptive Optics
ZA	Zenith Angle

Bibliography

[1] M. Bass, D. Casimer, J. Enoch, V. Lakshminarayanan, G. Li, C. MacDonald, M. Virendra, and E. Van Stryland, *Handbook of Optics - Vol II.* McGraw-Hill Education; 3 edition, 2009.

[2] M. Bass, D. Casimer, J. Enoch, V. Lakshminarayanan, G. Li, C. MacDonald, M. Virendra, and E. Van Stryland, *Handbook of Optics - Vol I.* McGraw-Hill Education; 3 edition, 2009.

[3] E. C. Fest, *Stray light: analysis and control.* SPIE Press, Bellingham, 2013.

[4] W. T. Welford, *Aberrations of the Symmetrical Optical Systems.* Academic Press, London, 1974.

[5] A. B. Bhatia and E. Wolf, "On the circle polynomials of zernike and related orthogonal sets," *Proc. Cambridge Phil. Soc., 50, 40*, 1954.

[6] A. Maréchal, "Etude des effets combinés de la diffraction et des aberrations géométriques sur l'image d'un point lumineux," *Rev. Opt.*, vol. 2, pp. 257–277, 1947.

[7] T. S. Ross, "Limitations and applicability of the maréchal approximation," *Appl. Opt.*, vol. 48, pp. 1812–1818, Apr 2009.

[8] C. S. Williams and O. A. Becklund, *Introduction to the optical transfer function*, vol. 112. SPIE Press, 1989.

[9] W. A. Traub and B. R. Oppenheimer, "Direct imaging of exoplanets," in *University of Arizona Press*, pp. 111–156, 2011.

[10] A. Boutonnet, J. Schoenmaekers, and W. Martens, *JUICE - Consolidated Report on Mission Analysis.* 2015.

[11] J. team, *JANUS - Scientific Performance Report.* 2014.

[12] J. team, *JANUS - Instrument Requirements Specification.* 2014.

[13] K. Dohlen, M. Saisse, G. Claeysen, P. L. Lamy, and J.-L. Boit, "Optical designs for the Rosetta narrow-angle camera," *Optical Engineering*, vol. 35, Apr. 1996.

[14] D. Korsch, *Reflective optics.* Academic Press Limited, London, 1991.

[15] W. B. Wetherell, "The use of image quality criteria in designing a diffraction limited large space telescope," 1972.

[16] M. Hoek, E. Bennet, D. Branford, E. Cowie, M. Düren, K. Föhl, D. Glazier, R. Kaiser, A. Lehmann, S. Lu, J. Marton, R. Ostendorf, G. Schepers, C. Schwarz, B. Seitz, A. Teufel, and D. Watts, "Radiation hardness study on fused silica," in *Nuclear Instruments and Methods in Physics*, vol. 595, pp. 190–193, 2008.

[17] T. P. Lester, M. L. McCall, and J. B. Tatum, "Theory of planetary photometry," *Journal of the Royal Astronomical Society of Canada*, vol. 73, p. 233, 1979.

[18] M. J. Persky, "Review of black surfaces for space-borne infrared systems," *Review of Scientific Instruments*, vol. 70, pp. 2193–2217, May 1999.

[19] J. team, *JANUS - Instrument Design Report*. 2014.

[20] G. Marra, L. Colangeli, and e. a. Mazzotta Epifani, E., "The Optical Design of the High Resolution Imaging Channel for the SIMBIO-SYS experiment on the BepiColombo Mission to Mercury," *Memorie della Società Astronomica Italiana Supplementi*, vol. 12, p. 77, 2008.

[21] A. Fortier, T. Beck, W. Benz, C. Broeg, V. Cessa, D. Ehrenreich, and N. Thomas, "CHEOPS: a space telescope for ultra-high precision photometry of exoplanet transits," in *Space Telescopes and Instrumentation 2014: Optical, Infrared, and Millimeter Wave*, vol. 9143 of *SPIE Proc.*, p. 91432J, 2014.

[22] G. L. Peterson, "Analytic expression for in-field scattered light distribution," in *SPIE Proc.*, vol. 5178, pp. 184–193, 2004.

[23] J. Farinato, F. Pedichini, E. Pinna, F. Baciotti, C. Baffa, A. Baruffolo, M. Bergomi, P. Bruno, E. Cappellaro, L. Carbonaro, A. Carlotti, M. Centrone, L. Close, J. Codona, S. Desidera, M. Dima, S. Esposito, D. Fantinel, G. Farisato, A. Fontana, W. Gaessler, E. Giallongo, R. Gratton, D. Greggio, J. C. Guerra, O. Guyon, P. Hinz, F. Leone, F. Lisi, D. Magrin, L. Marafatto, M. Munari, I. Pagano, A. Puglisi, R. Ragazzoni, B. Salasnich, E. Sani, S. Scuderi, M. Stangalini, V. Testa, C. Verinaud, and V. Viotto, "SHARK (System for coronagraphy with High order Adaptive optics from R to K band): a proposal for the LBT 2nd generation instrumentation," in *Ground-based and Airborne Instrumentation for Astronomy V*, vol. 9147 of *SPIE Proceedings*, p. 91477J, Aug. 2014.

[24] F. Pedichini, M. Stangalini, A. Ambrosino, A. Puglisi, E. Pinna, V. Bailey, L. Carbonaro, M. Centrone, J. Christou, S. Esposito, J. Farinato, F. Fiore, E. Giallongo, J. M. Hill, P. M. Hinz, and L. Sabatini, "High Contrast Imaging in the Visible: First Experimental Results at the Large Binocular Telescope," *ArXiv e-prints*, Sept. 2016.

[25] R. Ragazzoni and J. Farinato, "Sensitivity of a pyramidic Wave Front sensor in closed loop Adaptive Optics," *Astronomy and Astrophysics*, vol. 350, pp. L23–L26, Oct. 1999.

[26] S. Esposito and A. Riccardi, "Pyramid Wavefront Sensor behavior in partial correction Adaptive Optic systems," *Astronomy and Astrophysics*, vol. 369, pp. L9–L12, Apr. 2001.

[27] A. Vigan, C. Gry, G. Salter, D. Mesa, D. Homeier, C. Moutou, and F. Allard, "High-contrast imaging of Sirius A with VLT/SPHERE: looking for giant planets down to one astronomical unit," *MNRAS*, vol. 454, pp. 129–143, Nov. 2015.

[28] A. Riccardi, M. Xompero, R. Briguglio, F. Quirós-Pacheco, L. Busoni, L. Fini, A. Puglisi, S. Esposito, C. Arcidiacono, E. Pinna, P. Ranfagni, P. Salinari, G. Brusa, R. Demers, R. Biasi, and D. Gallieni, "The adaptive secondary mirror for the Large Binocular Telescope: optical acceptance test and preliminary on-sky commissioning results," in *SPIE Proc.*, vol. 7736 of *SPIE Proc.*, p. 77362C, July 2010.

[29] G. Agapito, C. Arcidiacono, F. Quirós-Pacheco, and S. Esposito, "Adaptive optics at short wavelengths. Expected performance and sky coverage of the FLAO system going toward visible wavelengths," *Experimental Astronomy*, vol. 37, pp. 503–523, Nov. 2014.

[30] J.-L. Beuzit, A. Boccaletti, M. Feldt, K. Dohlen, D. Mouillet, P. Puget, F. Wildi, L. Abe, J. Antichi, A. Baruffolo, P. Baudoz, M. Carbillet, J. Charton, R. Claudi, S. Desidera, M. Downing, C. Fabron, P. Feautrier, E. Fedrigo, T. Fusco, J.-L. Gach, E. Giro, R. Gratton, T. Henning, N. Hubin, F. Joos, M. Kasper, A.-M. Lagrange, M. Langlois, R. Lenzen, C. Moutou, A. Pavlov, C. Petit, J. Pragt, P. Rabou, F. Rigal, S. Rochat, R. Roelfsema, G. Rousset, M. Saisse, H.-M. Schmid, E. Stadler, C. Thalmann, M. Turatto, S. Udry, F. Vakili, A. Vigan, and R. Waters, "Direct Detection of Giant Extrasolar Planets with SPHERE on the VLT," in *Pathways Towards Habitable Planets* (V. Coudé du Foresto, D. M. Gelino, and I. Ribas, eds.), vol. 430 of *Astronomical Society of the Pacific Conference Series*, p. 231, Oct. 2010.

[31] B. A. Macintosh, J. R. Graham, D. W. Palmer, R. Doyon, J. Dunn, D. T. Gavel, J. Larkin, B. Oppenheimer, L. Saddlemyer, A. Sivaramakrishnan, J. K. Wallace, B. Bauman, D. A. Erickson, C. Marois, L. A. Poyneer, and R. Soummer, "The Gemini Planet Imager: from science to design to construction," in *Adaptive Optics Systems*, vol. 7015 of *SPIE Proc.*, p. 701518, July 2008.

[32] L. M. Close, J. R. Males, D. A. Kopon, V. Gasho, K. B. Follette, P. Hinz, K. Morzinski, A. Uomoto, T. Hare, A. Riccardi, S. Esposito, A. Puglisi, E. Pinna, L. Busoni, C. Arcidiacono, M. Xompero, R. Briguglio, F. Quiros-Pacheco, and J. Argomedo, "First closed-loop visible AO test results for the advanced adaptive secondary AO system for the Magellan Telescope: MagAO's performance and status," in *Adaptive Optics Systems III*, vol. 8447 of *SPIE Proc.*, p. 84470X, July 2012.

[33] O. Guyon, F. Martinache, C. Clergeon, R. Russell, T. Groff, and V. Garrel, "Wavefront control with the Subaru Coronagraphic Extreme Adaptive Optics (SCExAO) system," in *Astronomical Adaptive Optics Systems and Applications IV*, vol. 8149 of *SPIE Proc.*, p. 814908, Oct. 2011.

[34] R. Dekany, R. Burruss, J. C. Shelton, B. Oppenheimer, G. Vasisht, S. Metchev, J. Roberts, J. Tesch, T. Truong, J. Milburn, D. Hale, C. Baranec, S. Hildebrandt, M. Wahl, C. Beichman, L. Hillenbrand, R. Patel, S. Hinkley, E. Cady, and I. Parry, "First exoplanet and disk results with the PALM-3000 adaptive optics system," in *Proceedings of the Third AO4ELT Conference* (S. Esposito and L. Fini, eds.), p. 52, Dec. 2013.

[35] N. Jovanovic, F. Martinache, O. Guyon, C. Clergeon, G. Singh, T. Kudo, V. Garrel, K. Newman, D. Doughty, J. Lozi, J. Males, Y. Minowa, Y. Hayano, N. Takato, J. Morino, J. Kuhn, E. Serabyn, B. Norris, P. Tuthill, G. Schworer, P. Stewart, L. Close, E. Huby,

G. Perrin, S. Lacour, L. Gauchet, S. Vievard, N. Murakami, F. Oshiyama, N. Baba, T. Matsuo, J. Nishikawa, M. Tamura, O. Lai, F. Marchis, G. Duchene, T. Kotani, and J. Woillez, "The Subaru Coronagraphic Extreme Adaptive Optics System: Enabling High-Contrast Imaging on Solar-System Scales," *Publications of the Astronomical Society of Pacific*, vol. 127, pp. 890–910, Sept. 2015.

[36] J. X. Prochaska, E. Gawiser, A. M. Wolfe, S. Castro, and S. G. Djorgovski, "The Age-Metallicity Relation of the Universe in Neutral Gas: The First 100 Damped Ly-alpha Systems," *ApJ letters*, vol. 595, pp. L9–L12, Sept. 2003.

[37] C. Vérinaud, M. Le Louarn, V. Korkiakoski, and M. Carbillet, "Adaptive optics for high-contrast imaging: pyramid sensor versus spatially filtered Shack-Hartmann sensor," *MNRAS*, vol. 357, pp. L26–L30, Feb. 2005.

[38] S. Esposito, A. Riccardi, L. Fini, E. Pinna, A. Puglisi, F. Quiros, M. Xompero, R. Briguglio, L. Busoni, P. Stefanini, C. Arcidiacono, G. Brusa, and D. Miller, "LBT AO on-sky results," in *Second International Conference on Adaptive Optics for Extremely Large Telescopes. Online at ¡A href="http://ao4elt2.lesia.obspm.fr"¿http://ao4elt2.lesia.obspm.fr¡/A¿, id.3*, p. 3, Sept. 2011.

[39] S. E. Dodson-Robinson, D. Veras, E. B. Ford, and C. A. Beichman, "The Formation Mechanism of Gas Giants on Wide Orbits," *ApJ*, vol. 707, pp. 79–88, Dec. 2009.

[40] P. Goldreich and R. Sari, "Eccentricity Evolution for Planets in Gaseous Disks," *ApJ*, vol. 585, pp. 1024–1037, Mar. 2003.

[41] K. L. Luhman, P. R. Allen, C. Espaillat, L. Hartmann, and N. Calvet, "The Disk Population of the Taurus Star-Forming Region," *The Astrophysical Journal Supplement*, vol. 186, pp. 111–174, Jan. 2010.

[42] S. Daemgen, M. Bonavita, R. Jayawardhana, D. Lafrenière, and M. Janson, "Sub-stellar Companions and Stellar Multiplicity in the Taurus Star-forming Region," *The Astrophysical Journal*, vol. 799, p. 155, Feb. 2015.

[43] A. L. Kraus and M. J. Ireland, "A Young Exoplanet Caught at Formation," in *American Astronomical Society Meeting Abstracts #219*, vol. 219 of *American Astronomical Society Meeting Abstracts*, p. 228.03, Jan. 2012.

[44] J. E. Schlieder, S. Lépine, and M. Simon, "Likely Members of the β Pictoris and AB Doradus Moving Groups in the North," *The Astronomical Journal*, vol. 144, p. 109, Oct. 2012.

[45] J. Gagné, D. Lafrenière, R. Doyon, L. Malo, and É. Artigau, "BANYAN. V. A Systematic All-sky Survey for New Very Late-type Low-mass Stars and Brown Dwarfs in Nearby Young Moving Groups," *ApJ*, vol. 798, p. 73, Jan. 2015.

[46] A. J. Skemer, P. M. Hinz, S. Esposito, A. Burrows, J. Leisenring, M. Skrutskie, S. Desidera, D. Mesa, C. Arcidiacono, F. Mannucci, T. J. Rodigas, L. Close, D. McCarthy, C. Kulesa, G. Agapito, D. Apai, J. Argomedo, V. Bailey, K. Boutsia, R. Briguglio,

G. Brusa, L. Busoni, R. Claudi, J. Eisner, L. Fini, K. B. Follette, P. Garnavich, R. Gratton, J. C. Guerra, J. M. Hill, W. F. Hoffmann, T. Jones, M. Krejny, J. Males, E. Masciadri, M. R. Meyer, D. L. Miller, K. Morzinski, M. Nelson, E. Pinna, A. Puglisi, S. P. Quanz, F. Quiros-Pacheco, A. Riccardi, P. Stefanini, V. Vaitheeswaran, J. C. Wilson, and M. Xompero, "First Light LBT AO Images of HR 8799 bcde at 1.6 and 3.3 μm: New Discrepancies between Young Planets and Old Brown Dwarfs," *ApJ*, vol. 753, p. 14, July 2012.

[47] B. R. Oppenheimer, C. Baranec, C. Beichman, D. Brenner, R. Burruss, E. Cady, J. R. Crepp, R. Dekany, R. Fergus, D. Hale, L. Hillenbrand, S. Hinkley, D. W. Hogg, D. King, E. R. Ligon, T. Lockhart, R. Nilsson, I. R. Parry, L. Pueyo, E. Rice, J. E. Roberts, L. C. Roberts, Jr., M. Shao, A. Sivaramakrishnan, R. Soummer, T. Truong, G. Vasisht, A. Veicht, F. Vescelus, J. K. Wallace, C. Zhai, and N. Zimmerman, "Reconnaissance of the HR 8799 Exosolar System. I. Near-infrared Spectroscopy," *The Astrophysical Journal*, vol. 768, p. 24, May 2013.

[48] A. Garufi, S. P. Quanz, H. Avenhaus, E. Buenzli, C. Dominik, F. Meru, M. R. Meyer, P. Pinilla, H. M. Schmid, and S. Wolf, "Small vs. large dust grains in transitional disks: do different cavity sizes indicate a planet?. SAO 206462 (HD 135344B) in polarized light with VLT/NACO," *Astronomy and Astrophysics*, vol. 560, p. A105, Dec. 2013.

[49] S. team, *Proposal for a Coronagraph using extreme AO for the LBT: SHARK*. 2014.

[50] M. Kuzuhara, M. Tamura, T. Kudo, M. Janson, R. Kandori, T. D. Brandt, C. Thalmann, D. Spiegel, B. Biller, J. Carson, Y. Hori, R. Suzuki, A. Burrows, T. Henning, E. L. Turner, M. W. McElwain, A. Moro-Martín, T. Suenaga, Y. H. Takahashi, J. Kwon, P. Lucas, L. Abe, W. Brandner, S. Egner, M. Feldt, H. Fujiwara, M. Goto, C. A. Grady, O. Guyon, J. Hashimoto, Y. Hayano, M. Hayashi, S. S. Hayashi, K. W. Hodapp, M. Ishii, M. Iye, G. R. Knapp, T. Matsuo, S. Mayama, S. Miyama, J.-I. Morino, J. Nishikawa, T. Nishimura, T. Kotani, N. Kusakabe, T.-S. Pyo, E. Serabyn, H. Suto, M. Takami, N. Takato, H. Terada, D. Tomono, M. Watanabe, J. P. Wisniewski, T. Yamada, H. Takami, and T. Usuda, "Direct Imaging of a Cold Jovian Exoplanet in Orbit around the Sun-like Star GJ 504," *The Astrophysical Journal*, vol. 774, p. 11, Sept. 2013.

[51] A. Carlotti, R. Vanderbei, and N. J. Kasdin, "Optimal pupil apodizations for arbitrary apertures," *ArXiv e-prints*, Aug. 2011.

[52] A. Ghedina and R. Ragazzoni, "Optimum configurations for two off-axis parabolae used to make an optical relay.," *Journal of Modern Optics*, vol. 44, pp. 1259–1267, July 1997.

[53] A. Carlotti, "Apodized phase mask coronagraphs for arbitrary apertures," *Astronomy and Astrophysics*, vol. 551, p. A10, Mar. 2013.

[54] C. G. Wynne, "Correction of atmospheric dispersion in the infrared," *MNRAS*, vol. 282, pp. 863–867, Oct. 1996.

[55] C. G. Wynne, "Correction of atmospheric dispersion in a converging beam," *The Observatory*, vol. 104, pp. 140–142, June 1984.

[56] M. N'Diaye, K. Dohlen, T. Fusco, and B. Paul, "Calibration of quasi-static aberrations in exoplanet direct-imaging instruments with a Zernike phase-mask sensor," *Astronomy and Astrophysics*, vol. 555, p. A94, July 2013.

[57] R. Racine, G. A. H. Walker, D. Nadeau, R. Doyon, and C. Marois, "Speckle Noise and the Detection of Faint Companions," *PASP*, vol. 111, pp. 587–594, May 1999.

[58] C. Marois, R. Doyon, R. Racine, and D. Nadeau, "Efficient Speckle Noise Attenuation in Faint Companion Imaging," *PASP*, vol. 112, pp. 91–96, Jan. 2000.

[59] C. Perrot, A. Boccaletti, E. Pantin, J.-C. Augereau, A.-M. Lagrange, R. Galicher, A.-L. Maire, J. Mazoyer, J. Milli, G. Rousset, R. Gratton, M. Bonnefoy, W. Brandner, E. Buenzli, M. Langlois, J. Lannier, D. Mesa, S. Peretti, G. Salter, E. Sissa, G. Chauvin, S. Desidera, M. Feldt, A. Vigan, E. Di Folco, A. Dutrey, J. Péricaud, P. Baudoz, M. Benisty, J. De Boer, A. Garufi, J. H. Girard, F. Menard, J. Olofsson, S. P. Quanz, D. Mouillet, V. Christiaens, S. Casassus, J.-L. Beuzit, P. Blanchard, M. Carle, T. Fusco, E. Giro, N. Hubin, D. Maurel, O. Moeller-Nilsson, A. Sevin, and L. Weber, "Discovery of concentric broken rings at sub-arcsec separations in the HD 141569A gas-rich, debris disk with VLT/SPHERE," *Astronomy and Astrophysics*, vol. 590, p. L7, May 2016.

[60] E. Oliva, S. Gennari, L. Vanzi, A. Caruso, and M. Ciofini, "Optical materials for near infrared Wollaston prisms," *Astronomy and Astrophysics*, vol. 123, May 1997.

[61] S. F. Sánchez, U. Thiele, J. Aceituno, D. Cristobal, J. Perea, and J. Alves, "The Night Sky at the Calar Alto Observatory II: The Sky at the Near-infrared," *PASP*, vol. 120, pp. 1244–1254, Nov. 2008.

[62] F. Patat, "Impact of optical and near-IR Sky brightness on Site Evaluation," *ESO internal report*, 2006.

[63] M. G. Dittman, "Contamination scatter functions for stray-light analysis," in *Optical System Contamination: Effects, measurements and control VII*, vol. 4774 of *SPIE Proc.*, 2002.

[64] E. L. Church, "Fractal surface finish," *Appl. Opt.*, vol. 27, pp. 1518–1526, Apr 1988.

[65] K. Dohlen, F. P. Wildi, P. Puget, D. Mouillet, and J.-L. Beuzit, "SPHERE: Confronting in-lab performance with system analysis predictions," in *Second International Conference on Adaptive Optics for Extremely Large Telescopes. Online at ¡A href="http://ao4elt2.lesia.obspm.fr"¿http://ao4elt2.lesia.obspm.fr¡/A¿, id.75*, p. 75, Sept. 2011.

[66] S. team, *SHARK-NIR Simulation Tool*. 2016.

[67] H. Rauer, C. Catala, C. Aerts, T. Appourchaux, W. Benz, A. Brandeker, J. Christensen-Dalsgaard, M. Deleuil, L. Gizon, M.-J. Goupil, M. Güdel, E. Janot-Pacheco, M. Mas-Hesse, I. Pagano, G. Piotto, D. Pollacco, Ċ. Santos, A. Smith, J.-C. Suárez, R. Szabó, S. Udry, V. Adibekyan, Y. Alibert, J.-M. Almenara, P. Amaro-Seoane, M. A.-v. Eiff, M. Asplund, E. Antonello, S. Barnes, F. Baudin, K. Belkacem, M. Bergemann, G. Bihain, A. C. Birch, X. Bonfils, I. Boisse, A. S. Bonomo, F. Borsa, I. M. Brandão, E. Brocato, S. Brun, M. Burleigh, R. Burston, J. Cabrera, S. Cassisi, W. Chaplin, S. Charpinet,

C. Chiappini, R. P. Church, S. Csizmadia, M. Cunha, M. Damasso, M. B. Davies, H. J. Deeg, R. F. Díaz, S. Dreizler, C. Dreyer, P. Eggenberger, D. Ehrenreich, P. Eigmüller, A. Erikson, R. Farmer, S. Feltzing, F. de Oliveira Fialho, P. Figueira, T. Forveille, M. Fridlund, R. A. García, P. Giommi, G. Giuffrida, M. Godolt, J. Gomes da Silva, T. Granzer, J. L. Grenfell, A. Grotsch-Noels, E. Günther, C. A. Haswell, A. P. Hatzes, G. Hébrard, S. Hekker, R. Helled, K. Heng, J. M. Jenkins, A. Johansen, M. L. Khodachenko, K. G. Kislyakova, W. Kley, U. Kolb, N. Krivova, F. Kupka, H. Lammer, A. F. Lanza, Y. Lebreton, D. Magrin, P. Marcos-Arenal, P. M. Marrese, J. P. Marques, J. Martins, S. Mathis, S. Mathur, S. Messina, A. Miglio, J. Montalban, M. Montalto, M. J. P. F. G. Monteiro, H. Moradi, E. Moravveji, C. Mordasini, T. Morel, A. Mortier, V. Nascimbeni, R. P. Nelson, M. B. Nielsen, L. Noack, A. J. Norton, A. Ofir, M. Oshagh, R.-M. Ouazzani, P. Pápics, V. C. Parro, P. Petit, B. Plez, E. Poretti, A. Quirrenbach, R. Ragazzoni, G. Raimondo, M. Rainer, D. R. Reese, R. Redmer, S. Reffert, B. Rojas-Ayala, I. W. Roxburgh, S. Salmon, A. Santerne, J. Schneider, J. Schou, S. Schuh, H. Schunker, A. Silva-Valio, R. Silvotti, I. Skillen, I. Snellen, F. Sohl, S. G. Sousa, A. Sozzetti, D. Stello, K. G. Strassmeier, M. Švanda, G. M. Szabó, A. Tkachenko, D. Valencia, V. Van Grootel, S. D. Vauclair, P. Ventura, F. W. Wagner, N. A. Walton, J. Weingrill, S. C. Werner, P. J. Wheatley, and K. Zwintz, "The PLATO 2.0 mission," *Experimental Astronomy*, vol. 38, pp. 249–330, Nov. 2014.